

AD-A130 913

TRANSIENT RESPONSE OF SUPERCONDUCTING MICROBRIDGES TO
SUPERCritical CURRENTS(U) HARVARD UNIV CAMBRIDGE MA DIV
OF APPLIED SCIENCES D J FRANK JUN 83 TR-20

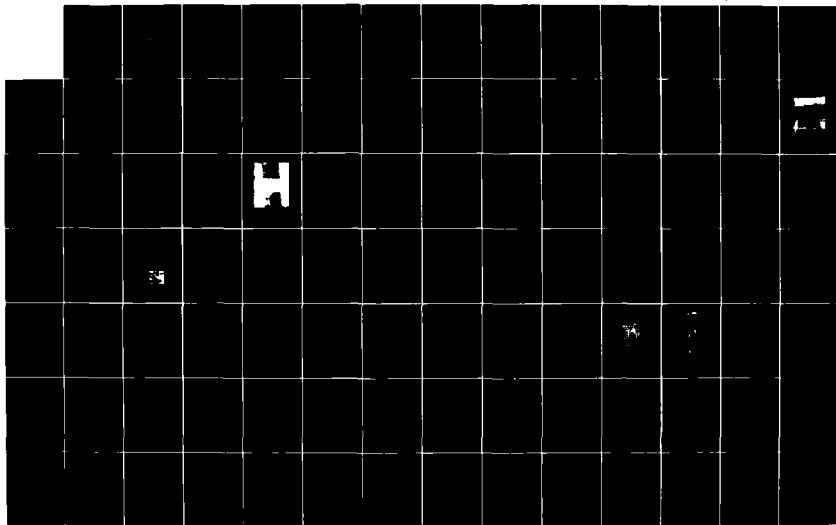
1/2

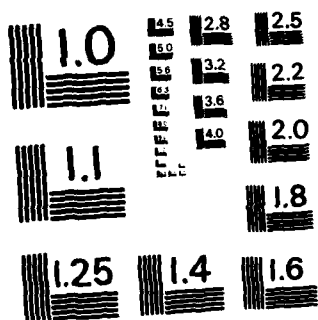
UNCLASSIFIED

N00014-77-C-0085

F/G 20/3

NL





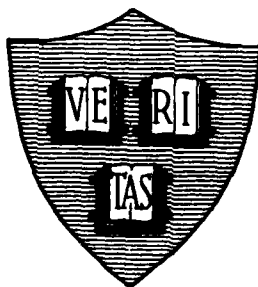
MICROCOPY RESOLUTION TEST CHART
NATIONAL BUREAU OF STANDARDS-1963-A

AD A 130913

(12)

Office of Naval Research
Contract N00014-77-C-0085 NR-310-116
Contract N00014-75-C-0048 NR-372-012
National Science Foundation Grant DMR79-04155

TRANSIENT RESPONSE OF SUPERCONDUCTING
MICROBRIDGES TO SUPERCRITICAL CURRENTS



By

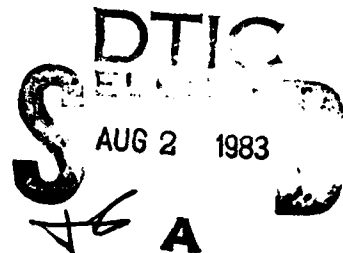
David J. Frank

JUNE 1983

Technical Report No. 20

This document has been approved for public release
and sale; its distribution is unlimited. Reproduction in
whole or in part is permitted by the U. S. Government.

Division of Applied Sciences
Harvard University Cambridge, Massachusetts



DTIC FILE COPY

88 08 01 015

Unclassified

SECURITY CLASSIFICATION OF THIS PAGE (When Data Entered)

REPORT DOCUMENTATION PAGE		READ INSTRUCTIONS BEFORE COMPLETING FORM
1. REPORT NUMBER Technical Report No. 20	2. GOVT ACCESSION NO. AD A130913	3. RECIPIENT'S CATALOG NUMBER
4. TITLE (and Subtitle) TRANSIENT RESPONSE OF SUPERCONDUCTING MICROBRIDGES TO SUPERCRITICAL CURRENTS		5. TYPE OF REPORT & PERIOD COVERED Interim Report
7. AUTHOR(s) David J. Frank		6. PERFORMING ORG. REPORT NUMBER
9. PERFORMING ORGANIZATION NAME AND ADDRESS Division of Applied Sciences Harvard University Cambridge, Mass. 02138		8. CONTRACT OR GRANT NUMBER(s) N00014-77-C-0085 N00014-75-C-0648 NSF DMR79-04155
11. CONTROLLING OFFICE NAME AND ADDRESS		10. PROGRAM ELEMENT, PROJECT, TASK AREA & WORK UNIT NUMBERS
14. MONITORING AGENCY NAME & ADDRESS (if different from Controlling Office)		12. REPORT DATE June 1983
		13. NUMBER OF PAGES 164
		15. SECURITY CLASS. (of this report) Unclassified
		15a. DECLASSIFICATION, DOWNGRADING SCHEDULE
16. DISTRIBUTION STATEMENT (of this Report) Reproduction in whole or in part is permitted for any purpose of the United States Government. Approved for public release; distribution unlimited.		
17. DISTRIBUTION STATEMENT (of the abstract entered in Block 20, if different from Report)		
18. SUPPLEMENTARY NOTES		
19. KEY WORDS (Continue on reverse side if necessary and identify by block number) Time-resolved measurements voltage waveforms phase slip center nonequilibrium superconductivity theory		
20. ABSTRACT (Continue on reverse side if necessary and identify by block number) We have made time-resolved measurements of the voltage waveforms on one-dimensional superconducting strips caused by current pulses in excess of their critical currents. We report the first known observations of the kinetic inductance spike the non-zero minimum voltage, and the time-domain development of phase-slip centers. These measurements were made on indium microbridges and represent an important extension of the work of Pals and Wolter (1979) to a higher critical temperature material. We have also measured the delay time between the application of the current pulse and the development of the first phase slip center in		

DD FORM 1473
1 JAN 73

EDITION OF 1 NOV 65 IS OBSOLETE
S/N 3102-014-6601

Unclassified

SECURITY CLASSIFICATION OF THIS PAGE (When Data Entered)

Unclassified

SECURITY CLASSIFICATION OF THIS PAGE (When Data Entered)

20. continued

these bridges and have used it in conjunction with the SST theory (Schmidt, Schön and Tinkham 1980) to estimate a τ_E of 140 picoseconds for indium. In addition, we have made a few measurements on dirty aluminum strips which also show the time-domain development of phase slip centers.

We have compared the data with the nonequilibrium superconductivity theory of SST wherever possible. To do this, we have developed a computer program that numerically solves the SST equations exactly in the one-dimensional, uniform strip approximation. From these numerical solutions we have found that, for the most part, the theory is in good agreement with the data. We have also used this exact solution to test the validity of several simpler approximations.

These experiments have been carried out using conventional electronics in the laboratory at Harvard and using a superconducting sampler circuit and pulse generator in a collaboration with IBM. This is the first known use of this superconducting circuitry for a nonequilibrium superconductivity experiment. In both types of experiments, the microbridges were fabricated using a small photolithographic facility that we helped to develop at Harvard.

Unclassified

SECURITY CLASSIFICATION OF THIS PAGE (When Data Entered)

Office of Naval Research

Contract N00014-77-C-0085 NR-319-116
Contract N00014-75-C-0648 NR-372-012
National Science Foundation Grant DMR79-04155

TRANSIENT RESPONSE OF SUPERCONDUCTING MICROBRIDGES
TO SUPERCRITICAL CURRENTS

By

David J. Frank

Technical Report No. 20

Reproduction in whole or in part is permitted for any
purpose of the United States Government. Approved
for public release; distribution unlimited.

June 1983

The research reported in this document was made possible through support extended the Division of Applied Sciences, Harvard University, by the Office of Naval Research, under Contract N00014-77-C-0085, Contract N00014-75-C-0648 and by the National Science Foundation under Grant DMR79-04155.

Division of Applied Sciences
Harvard University • Cambridge, Massachusetts

TABLE OF CONTENTS

	page
LIST OF FIGURES	iv
LIST OF TABLES	viii
CHAPTER I: INTRODUCTION	1
CHAPTER II: EXPERIMENTAL TECHNIQUES--HARVARD EXPERIMENTS	9
2.1 Introduction	9
2.2 Sample Fabrication Techniques	10
2.2.1 Sample Size Considerations	10
2.2.2 Photolithography	11
2.2.3 Contact Printing	14
2.2.4 Projection Photolithography	17
2.2.5 Fabrication Facilities	20
2.3 Early Harvard Experiments	26
2.4 Recent Harvard Experiments	34
CHAPTER III: EXPERIMENTAL TECHNIQUES--IBM EXPERIMENTS	42
3.1 Introduction	42
3.2 Josephson Junctions	43
3.3 The Superconducting Circuitry	47
3.4 Fabrication Details	53
3.5 Data Taking	57
CHAPTER IV: THEORY	61
4.1 Introduction	61
4.2 Tinkham's Phenomenological Approach	67

LIST OF FIGURES

	page
Figure 1-1 Block diagram illustrating the basic form of our experiments.	2
Figure 1-2 An example of the results of this type of experiment.	6
Figure 2-1 Illustration of the basic processes involved in photolithography.	12
Figure 2-2 (a) Contact printing mask and (b) resulting microbridges.	16
Figure 2-3 Schematic illustration of the technique of projection lithography.	18
Figure 2-4 Indium microbridge made by projection photolithography.	21
Figure 2-5 Physical layout of the Harvard "clean" room.	23
Figure 2-6 Diagram of the projection attachment for our microscope.	25
Figure 2-7 Electrical setup used in the Harvard experiments. (a) shows a block diagram of the entire setup. (b) shows the effective electrical environment of the microbridge and (c) is an equivalent circuit.	27
Figure 2-8 Schematic diagram of the TTL pulse generator used in the early Harvard experiments.	29
Figure 2-9 Cut-away view of the setup used to connect the samples to the coaxial cables.	31
Figure 2-10 Examples of voltage waveforms taken on dirty aluminum.	33
Figure 2-11 Scheme used to make contact to the samples in the later Harvard samples.	37
Figure 2-12 Block schematic diagram of (a) the feedback-stabilized I/I_c circuit and (b) the synchronously detected chopped-feedback-stabilized circuit used to improve sensitivity for low resistance samples. Both of these use the tunnel diode pulse generator.	39
Figure 2-13 Voltage versus time waveforms for an indium microbridge taken using the circuit shown in Figure 2-12.	41

4.3 Simple Improvements	77
4.4 Numerical Solution of SST Equations	82
CHAPTER V: DATA ANALYSIS AND INTERPRETATION	94
5.1 Introduction	94
5.2 Indium Microbridges	94
5.2.1 Kinetic Inductance Spike and Nonzero Minimum Voltage	96
5.2.2 Delay Time	104
5.2.3 The Development of Phase-slip Centers	110
5.3 Aluminum Microbridges	116
CHAPTER VI: POSSIBLE FUTURE EXPERIMENTS	121
6.1 Introduction	121
6.2 Destruction of Superconductivity by a Pulsed Magnetic Field	121
6.3 Destruction of Superconductivity by a Burst of RF Current	124
CHAPTER VII: SUMMARY AND CONCLUSION	127
APPENDIX A: TUNNEL DIODE-BASED PULSE GENERATOR	130
APPENDIX B: NUMERICAL SOLUTION OF SST EQUATIONS	141
B.1 The Equations	141
B.2 Program Listing	145
REFERENCES	150
ACKNOWLEDGEMENTS	152

Figure 3-1 Josephson junction logic gates and threshold curves.	31
Figure 3-2 (a) Schematic diagram of the IBM superconducting circuitry and (b) An illustration of the operation of the Faris sampler.	48
Figure 3-3 Block diagram of the entire IBM experimental setup.	51
Figure 3-4 Picture of about 2/3 of one of the Josephson chips such as we used in our experiments. Our portion is in the upper right-hand corner.	55
Figure 3-5 Micrograph of our portion of the chip with the various parts of the circuit labeled.	56
Figure 3-6 Voltage versus time waveforms taken on sample BJ35-4-2 using the IBM superconducting circuitry.	59
Figure 4-1(a) Delay time as a function of I_D/I_C for dirty aluminum for the five theoretical models considered.	63
Figure 4-1(b) Delay time as a function of I_D/I_C for indium for the five theoretical models considered.	64
Figure 4-2 An example of the solution of the simplest form of the TDT GL model for $(1-T/T_C)=0.01$, $I_D/I_C=1.8$ and $t_{rise}/\tau_E=0.15$. (a) shows the gap and voltage development and (b) shows the corresponding δT development.	71
Figure 4-3 An illustration of the various regime boundaries in the simplest TDT GL model.	74
Figure 4-4 A comparison of the time evolution of the gap and the voltage for the five theoretical models considered.	79
Figure 4-5 Examples of the four generalized densities of states used in the SST equations.	85
Figure 4-6(a) Plot of the nonequilibrium quasiparticle distribution function as a function of time and energy.	86
Figure 4-6(b) Plot of the total quasiparticle density as a function of time and energy.	88
Figure 4-7(a) Plot showing the evolution of Δ , J_{sne} , V and the pair-breaking potential for indium as determined from our exact numerical solution of the SST equations.	89
Figure 4-7(b) Plot showing the time dependence of Δ , J_{sne} , V and the pair-breaking potential for dirty aluminum as calculated by our exact numerical solution of the SST equations.	90

Figure 4-8	Semi-log plots of the important densities of states as functions of energy for various values of the pair-breaking potential.	91
Figure 4-9	A set of waveforms simulating one of our IBM experiments, calculated using our exact numerical solution of the SST equations.	93
Figure 5-1	The voltage waveform data taken on sample BJ35-4-1 using the IBM circuitry.	97
Figure 5-2	The voltage waveform data taken on sample BK90-3-1 using the IBM circuitry.	98
Figure 5-3	Comparison of experimental and theoretical waveforms for IBM sample BJ35-4-1 for three different temperatures.	100
Figure 5-4	Measured inductive spike height as a function of temperature for two of the IBM samples. The solid and dashed lines are the theoretical predictions for the two samples.	102
Figure 5-5	Measured minimum voltage as a function of temperature for two of the IBM samples. The solid and dashed lines are the theoretical predictions for the two samples.	103
Figure 5-6	Illustration of our delay time definition for comparison of theory and experiment.	105
Figure 5-7	Measured delay time versus $(1-T/T_c)$ for the IBM samples. The solid line for each sample is a fit to the theory.	107
Figure 5-8	Plot of the delay time versus $(I_p/I_c - 1)$ for four different temperatures.	109
Figure 5-9	(a) An I-V curve showing phase slip centers, and (b) the time-domain development of these same phase slip centers.	111
Figure 5-10	The measured delay time as a function of I_p/I_c for each of the four PSC's seen in the waveforms in Figure 5-9(b).	113
Figure 5-11	The measured delay time for each PSC in Figure 5-10 plotted against I_p/I_c , where I_c is the effective critical current of each PSC. The solid line is the theoretical prediction for the first PSC.	114

Figure 5-12 Plot of the delay time versus (I_p/I_c-1) for four different temperatures for one of our dirty aluminum bridges, with a theoretical fit given for each temperature.	117
Figure 5-13 Set of voltage waveforms for a dirty aluminum bridge demonstrating the time-domain development of PSC's.	119
Figure 6-1 Possible experimental configuration for observing the time-domain destruction of superconductivity by a pulsed magnetic field.	122
Figure 6-2 (a) An applied 7GHz current burst and (b) the resulting voltage and (c) gap variation with time.	126
Figure A-1 (a) Block schematic diagram of the tunnel diode pulse generator. (b) Timing diagram showing one full cycle.	131
Figure A-2 I-V curve for the TD266A tunnel diode used in our pulse generator.	133
Figure A-3 Calibration diagram for G, the I-V curve correction control, as a function of the attenuation of the current output to the sample.	140

LIST OF TABLES

Table 3-1 Layers used in the IBM lead alloy technology.	54
Table 5-1 Measured properties of selected indium samples.	95

CHAPTER I

INTRODUCTION

In the 71 years since superconductivity was discovered, its equilibrium properties have come to be well understood and research has gradually moved on to the study of its nonequilibrium properties. Because superconductivity occurs at low temperatures, it has relatively long relaxation times which lead to a wide variety of nonequilibrium properties that are fairly easily observed. Many kinds of experiments have been done to probe nonequilibrium superconductivity. For example, Clarke (1972) used double tunnel junctions, Skocpol, Beasley and Tinkham (1974) and Dolan and Jackel (1977) studied phase slip centers and Peters and Meissner (1973) explored the high frequency impedance of long thin strips. Smith, Skocpol and Tinkham (1980) among others tested laser illuminated tunnel junctions, and Chi, et al. (1981) observed the transient response of superconducting films subjected to picosecond laser pulses. Dynamic experiments, such as this last one, are interesting in that they probe beyond the steady state properties.

The dynamic experiment reported in this work involves observing the response of a superconducting strip to a current pulse. A block diagram of the experiment is shown in Figure 1-1. It consists of three basic parts: a current-pulse generator, a superconducting strip, or microbridge as it is often called, and a high-speed voltage measuring

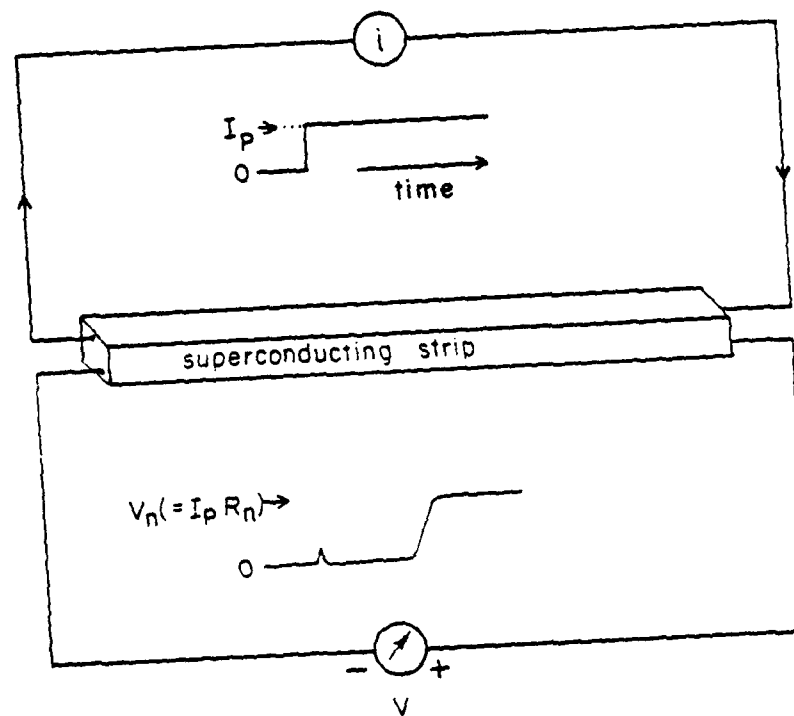


Figure 1-1 Block diagram illustrating the basic form of our experiments.

device. As indicated in the figure, we are concerned only with the rising edge of the pulse in this experiment. The superconductor starts out in the equilibrium state, with no current flowing through it. Suddenly, in as short a time as possible, the current through the strip is increased from zero to I_p . If the height of this current step is less than the critical current of the microbridge, the strip will remain superconducting, and therefore after an initial transient, such as is indicated in the figure, there will be no observable voltage. If, however, the height of the current step exceeds the critical current, then, after some period of time, the strip must reach the voltage level which it would show at that current level in its DC I-V curve. The primary goal of this experiment is to observe in the time domain how this superconducting-to-normal transition occurs.

In order to simplify the physics involved, the strip which is used needs to be effectively one-dimensional. This is required so that it will be possible to compare the predictions of the various theories of nonequilibrium superconductivity for this particular problem with the actual results of the experiments. Ginzburg-Landau theory shows that the strip can be treated as essentially one-dimensional when both its thickness and its width are less than or at most equal to $\xi_{GL}(T)$, the temperature-dependent superconducting coherence length (typically of order 1-2 μm). The fabrication techniques that were developed to accomplish this are included in Chapter 2.

In Figure 1-1, the pulse generator and voltage detector are shown as being simply connected to the sample by wires. In reality, of course, these must be either very short, or else they must be

transmission lines, so that high frequency signals will not be lost. Furthermore, the strip must be located in a cryogenic environment. This means that either the pulse generator and/or detector must also be in the cryogenic environment with the microbridge or that transmission lines must be used to bring the signal in and/or out of the cryostat. In the work reported here, two rather different approaches were used. In experiments at Harvard the pulse generator and detector were located outside the cryostat and a pair of four foot long 50Ω coaxial transmission lines were used in the cryostat to get the signal in and out. The details of these experiments are reported in Chapter 2. A separate series of experiments was done in a collaboration with IBM. In these the pulse generator and detector were located in the liquid helium along with the strip. They were both on the same $1/4$ " square silicon substrate. The microbridge was then added to the chip by projection photolithography. The details of this experiment are explained in Chapter 3.

The first measurements of the time required to drive a superconductor normal by application of current in excess of the critical current were made in the early 1960's (Gittleman and Bozowski 1964, Hagedorn 1964). At that time people were interested in the switching speed of such films because of their potential use as computer elements called cryotrons. Gittleman and Bozowski published fairly extensive data about tin and indium strips. Unfortunately their strips were somewhat too wide to be clearly one-dimensional and they only considered temperatures well below T_c ; hence direct comparison of their data with our one-dimensional theoretical predictions is rather

questionable. As a result, we have found it necessary to repeat their experiments (greatly aided by improvements in technology).

A variety of other time-domain measurements have also been done. Schmidlin, et al. (1960) worked on wider strips and were able to explain their results in terms of the growth of large thermal hot spots. In more recent experiments, Chi, et al. (1981) have directed picosecond laser pulses onto tunnel junctions and observed the resulting time-dependent quasi-particle population by studying the changes in the tunnel junction I-V curve. In an experiment that does not depend significantly on nonequilibrium, Faris and Pedersen (1981) used their superconducting sampling circuit to observe the switching time of a two-junction SQUID. This is the same sampling circuit that was used in our collaborative effort with IBM.

The present work was most directly motivated by the recent experiment of Pals and Wolter (1979). They observed a delay time between the rising edge of a current pulse through their superconducting aluminum strips and the onset of voltage along the strip. Their example of this is shown in Figure 1-2(a). They found that this delay time depended on the ratio of the height of their current pulse, I_p , to the critical current of the strip, I_c , as shown in Figure 1-2(b). Note that the delay time diverges as $I_p/I_c \rightarrow 1.0$ and decreases to rather small values as I_p/I_c increases. These qualitative features are the same as those seen in our experiments on different materials, as will be shown in Chapter 5.

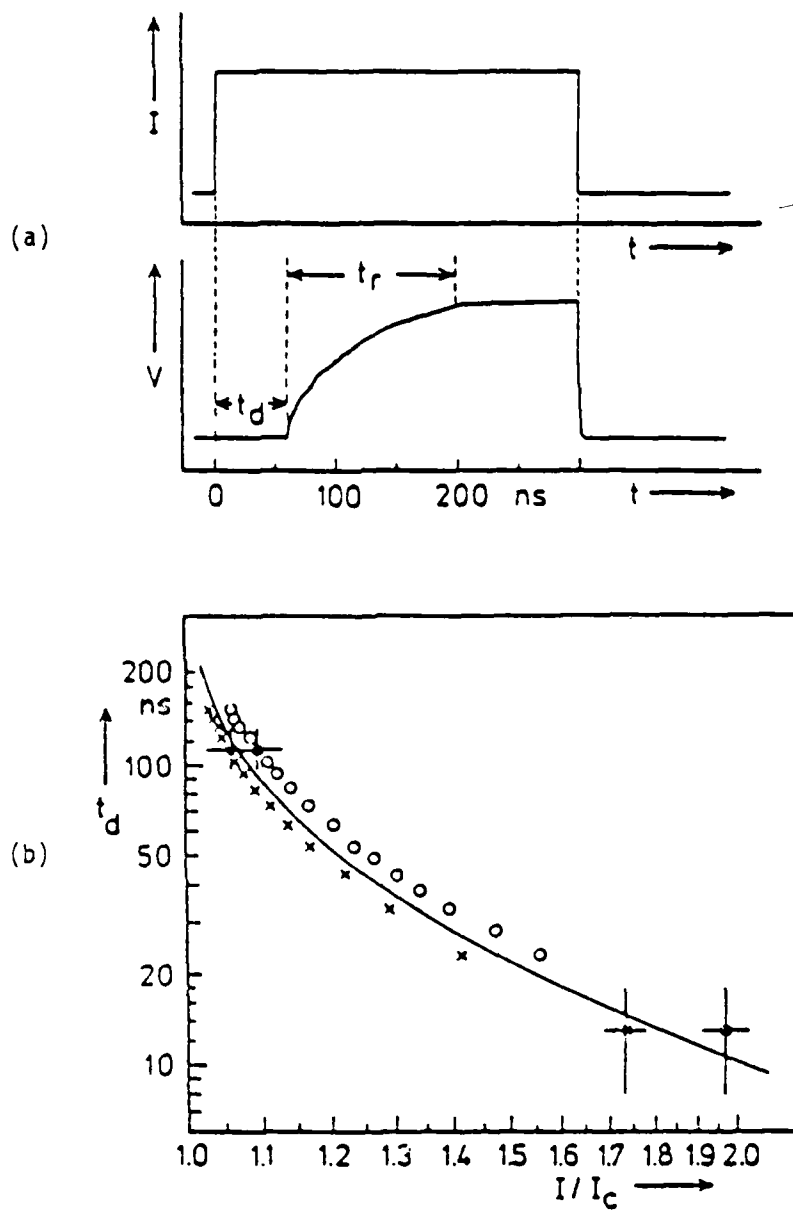


Figure 1-2 An example of the results of this type of experiment. (a) The current pulse and resulting waveform as a function of time. (b) The measured delay time versus I/I_c . (Taken from Pals and Wolter 1979.)

There are a variety of time constants that might be invoked to explain these results. Pals and Wolter initially believed that the Ginsburg-Landau time, τ_{GL} , set the over-all time scale for t_d . τ_{GL} is the time scale which governs changes in the superconducting energy gap, Δ , when Δ is extremely close to zero. Unfortunately the magnitude of the τ that they needed to explain their effect was much larger than the usually accepted value of τ_{GL} . Using a phenomenological approach developed from his study of weak links, Tinkham (1981) showed that τ_{Δ} should be the correct time scale to explain this effect. The time scale τ_{Δ} governs the rate of changes in the magnitude of Δ due to disequilibrium in the quasi-particle population, when Δ is not extremely small. Since $\tau_{\Delta} = 2.41 \tau_E (1 - T/T_C)^{-0.5}$, where τ_E is the inelastic scattering time of electrons at the Fermi surface at T_C , it should be possible to observe a temperature dependence in this delay time. Later experiments by Wolter, et al. (1981) and our own experiments have shown the existence of such a temperature dependence, though somewhat modified by other effects. In addition, our experiments manifest several other effects predicted by the detailed theory of Schmid and Schön (Schmid, et al. 1980) which we have applied to this problem. Our application of this theory was aided by the work of Geier and Schön (1982) on this same subject. Octavio, et al. (1981) and Oppenheim, et al. (1982) have carried out theoretical analyses of this experiment from the point of view of the Kramers and Watts-Tobin equations, with a special emphasis on the effects of finite length strips. Our own theoretical analyses and computations are discussed in Chapter 4.

The superconductors we have used in our experiments, "dirty" aluminum and indium, were chosen because of their anticipated delay times. Since the delay time depends on τ_E , and τ_E is known to decrease with increasing T_C of the material, and since the bandwidth of our equipment at Harvard was initially limited to 200 MHz, we chose the lowest T_C material we could conveniently test, which was "dirty" aluminum. Clean aluminum has a τ_E of ~ 12 nsec (Chi and Clarke 1979), but its T_C is about 1.2 K which was too cold for us to measure. However, when oxygen impurities are added to make it "dirty", its T_C can become as high as 2.0 K. We tested strips with T_C 's in the range 1.5-1.8 K. When the much higher speed IBM Josephson junction circuits became a possibility, we chose to use indium because its delay time was compatible with the time resolution of the circuits. The results of these experiments are reported in Chapter 5.

Chapter 6 contains some suggestions for further experiments in the area of transient nonequilibrium superconductivity, and the seventh chapter is a summary of the results and conclusions of this work. In addition there are several appendices containing some of the more laborious details of this work.

CHAPTER II

EXPERIMENTAL TECHNIQUES--HARVARD EXPERIMENTS

2.1 Introduction

Although conceptually only one type of experiment has been done in the course of this work, the measurements were made using two rather different techniques. For this reason, the techniques used with the superconducting circuitry in collaboration with IBM will be described separately in the next chapter. This chapter will deal only with the experimental details of the work done at Harvard using, for the most part, conventional room-temperature electronics.

The first step in doing this experiment was to fabricate appropriate samples. The clean room that was set up and the photolithographic techniques that were developed for this purpose are described in Section 2.

The experimental techniques that were used gradually evolved in the course of the research. Section 3 describes the earlier experiments, which were mostly on "dirty" aluminum and were limited by a simple homemade pulse generator with a 4-5 nsec rise-time. Eventually a much more sophisticated pulse generator was built and more experiments were performed. The details of this more recent experimental setup are discussed in Section 4.

2.2 Sample Fabrication Techniques

2.2.1 Sample Size Considerations

In order to be useful for comparisons with theory, the superconducting strips used must be effectively one-dimensional. This condition is satisfied only if d and $w \leq \xi_{GL}(T)$, where d is the thickness of the strip and w is its width. According to theory,

$$\xi_{GL} \cong \frac{0.856 \xi_0}{\sqrt{1.33 + \xi_0/\lambda} \sqrt{1-t}} \quad (T \cong T_c) \quad (2-1)$$

where ξ_0 is the BCS coherence length, λ is the electron mean free path and $t=T/T_c$. For "dirty" aluminum of the sort we want to use, λ is $\sim 40\text{\AA}$ and $\xi_0 = 1.6\mu\text{m}$ which gives $\xi_{GL}(1-t=.01) = .68\mu\text{m}$. For our indium, which is relatively clean, λ is $\sim 2500\text{\AA}$ and $\xi_0 = .364\mu\text{m}^*$ which gives $\xi_{GL}(1-t=.01) = 1.87\mu\text{m}$. Since the thickness is controlled by the amount of metal that is evaporated, it can easily be kept within these criteria. The width, however, will be determined by photolithography. Using the facilities we have acquired, we can make strips with uniform widths in the 1-2 μm range. Such widths should give satisfactory results for indium as long as the temperature is within a few percent of T_c , which is usually the regime of greatest interest.

* This value is suggested by Beasley and Orlando (Donnelly 1982); their source is unknown. Other literature values range from .20 μm (Guyon, et al. 1967) to .44 μm (Lindelof and Hansen 1977).

Unfortunately, strips with widths on the order of $.6\mu\text{m}$, as needed for aluminum, can only be made with techniques that are unavailable to us. As a result, we have had to settle for a less stringent criterion for the aluminum strips, namely that $w \leq \lambda_{\perp}$. According to the work of Skocpol (1976) this should result in current density variations of less than $\sim 15\%$ across the width of the strip. For our "dirty" aluminum we expect $\lambda_{\perp} \approx 2\lambda_{\text{eff}}^2/d$, where $\lambda_{\text{eff}}(1-t=.01)=6\mu\text{m}$. Thus, we can clearly make "dirty" aluminum microbridges with uniform current densities, but their one-dimensionality with regard to gap variation will always be in doubt. As a result, we place more emphasis on our measurements on indium.

The photolithographic techniques used to achieve these sizes are discussed in the next subsection.

2.2.2 Photolithography

Photolithography is a very useful tool for microfabrication which has been developed by the semiconductor industry for making integrated circuits. In general terms the procedure is as follows. The first step is to put a photosensitive layer (called "photoresist" or simply "resist") onto the substrate one plans to use. This is exposed to light in a desired pattern as shown in Figure 2-1(a). It is then developed, resulting in the removal of part of the layer (Figure 2-1(b)). The exposed part is removed if it is a positive resist (as in the Figure), and the unexposed part if it is a negative resist. The remaining layer is usually used in one of two ways. One can etch away the material that is no longer covered by photoresist, as in 2-1(c). Then, after the

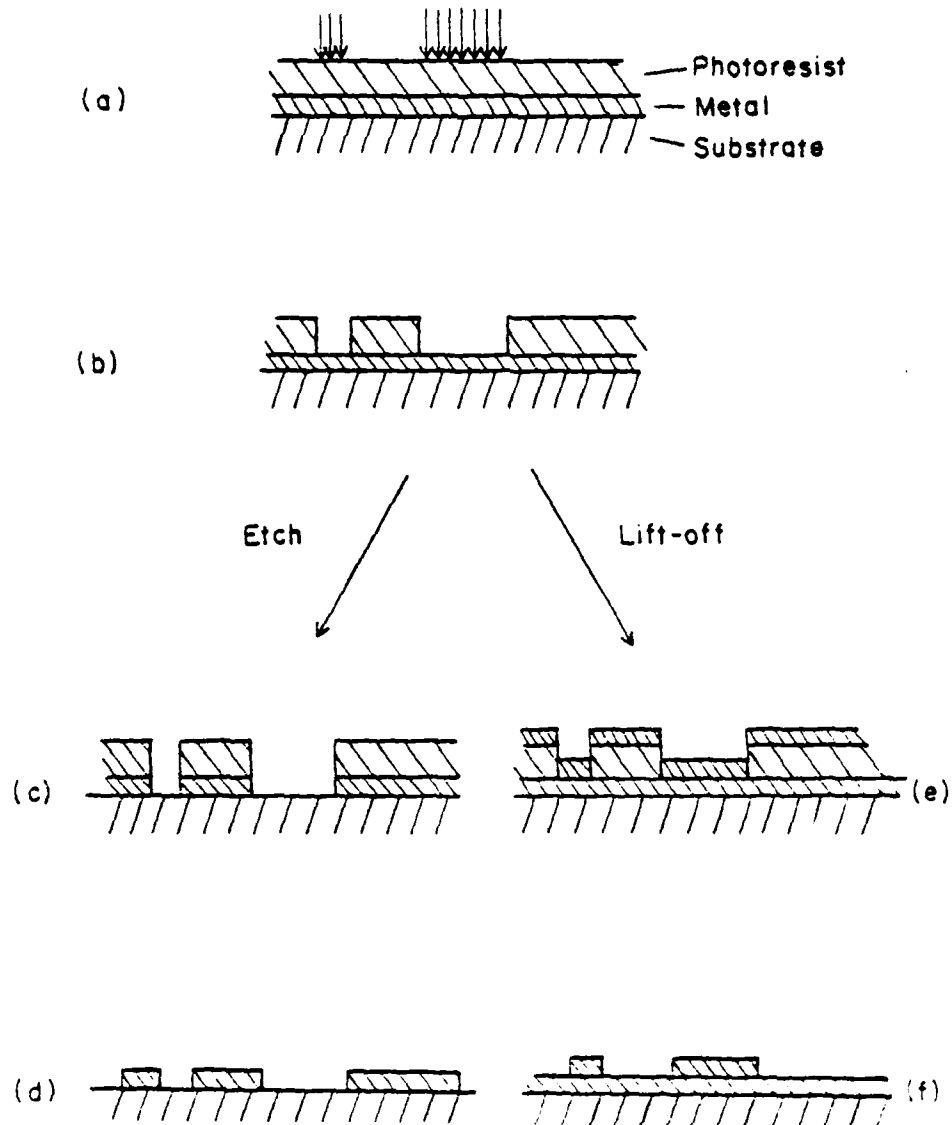


Figure 2-1 Illustration of the basic processes involved in photolithography. (a) The photoresist is exposed to a pattern resulting in (b) after it is developed. In (c) the metal beneath the photoresist has been etched away, leaving (d) as the final result. Using lift-off processing, (e) shows a metal film evaporated on top of (b). (f) is the final result after the photoresist and unwanted metal are removed.

unexposed photoresist is removed, the etched pattern remains (2-1(d)). Alternatively, one can deposit a layer of material on top of the patterned photoresist (2-1(e)) and then, when the unexposed photoresist is removed, it lifts away the material that was deposited on top of it (2-1(f)).

Some of the details of the specific processes we have used are described below. First, we cut the desired size of substrate from an ordinary 1mm thick glass microscope slide. We usually used 1" x 1" or 1" x 1/4" substrates. Then the substrates were cleaned by soaking them in acetone to remove grease, which would prevent metal from sticking to the substrate later, during the evaporation. Sometimes trichloroethylene was also used if the substrates needed to be particularly clean. We used Shipley AZ1350J positive photoresist for most of our fabrication.* The substrate was placed on a vacuum chuck in a photoresist spinner. Several drops of photoresist were applied while the substrate was stationary. Then vacuum was applied to the chuck to hold the substrate down while it was spun at 3-6K RPM for ~35 seconds. This produced a uniform photosensitive film about 1.5 μ m thick. Next, the substrate was baked at ~80°C for 20-30 minutes to harden the resist. It was then ready for exposure to a pattern.

* Shipley photoresist is made by Shipley Company, Inc. in Newton, Massachusetts. The AZ resists consist of polymerized Novalak resins with naphthoquinone diazides serving as sensitizers. When exposed to ultraviolet light, the diazides photochemically transfer energy to the polymer, changing it and making it soluble in the developer. Since the developer is only able to dissolve exposed resist, only the areas that were illuminated are removed. (Giang and Gregor 1970)

We used lift-off to make all of the samples tested. One subtlety in the use of lift-off is that if the banks on the photoresist are not completely vertical, the evaporated metal will also stick to them, forming a bridge between the top of the photoresist and the substrate. Then, when lift-off is attempted, it will be unsuccessful or will leave jagged edges. To avoid this, one needs vertical, or, better yet, undercut banks. Initially we used the two layer photoresist technique of Dunkleberger (1978) to obtain an undercut. Later the simpler chlorobenzene technique of Canavello, *et al.* (1977) became known and we have used it since then. In this technique the baked photoresist is soaked in chlorobenzene for ~8 minutes before exposure. This seems to toughen its surface and results in an undercut bank.

A variety of methods were tried to create the necessary pattern size in the photoresist, two of which produced useful results. In the first method, the pattern is made solely by contact printing. The second method uses contact printing only for the large pads through which electrical contact is made to the outside world, and uses a projection technique to create the narrow strips. These two methods are described in more detail below.

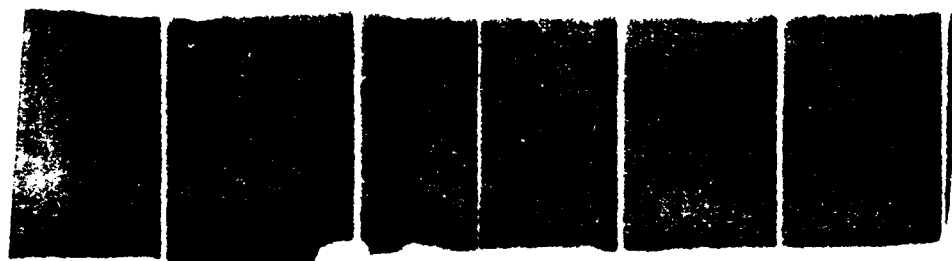
2.2.3 Contact Printing

Contact printing involves placing a high contrast mask in direct contact with the layer of photoresist. Ultraviolet light is then shone through the transparent portions of the mask to expose the photoresist. Hence, the features of the mask must be exactly the same size as the

desired final features of the developed photoresist layer. The mask that we used was invented by Prof. Skocpol; a picture of it is shown in Figure 2-2(a). It consists of a strip of metal 250 μ m wide, across the width of which various slits have been made using a diamond knife. The widths of the slits vary from ~ 1 to $\sim 6\mu$ m, depending on the exact angle and pressure of the diamond knife. Since these parameters could not be well controlled, a large number of slits were made so that, statistically, at least a few would turn out well.

This mask was pressed against a layer of photoresist on a clean glass substrate and ultraviolet light was shone through it to expose the photoresist. Next, the photoresist was developed in diluted developer (3 or 5 parts water, 1 part developer). At this point in the process the photoresist was gone from the areas where we wanted the metal film to be, as in Figure 2-1(b). The substrate with its photoresist pattern was then placed in a vacuum evaporator and "dirty" aluminum was thermally evaporated onto it from an electrically heated boat. The aluminum was made dirty by evaporating from an alumina-coated boat at $\sim 10\text{\AA}/\text{sec}$ at an oxygen pressure of 55 μ torr. The sample was then soaked in acetone to dissolve the unexposed photoresist and to lift off the unwanted metal.

An example of the result of this process is shown in Figure 2-2(b). Naturally, since the mask had many slits, the substrate ended up with many microbridges on it. The next step was to use a microscope to inspect each strip on a given substrate. The best one was chosen, and a diamond knife was used to carefully break all of the other bridges. Notice that in 2-2(b) all but one of the bridges have been cut.



(a)

200 μ m

(b)

Figure 2-2 (a) Contact printing mask and (b) resulting microbridges. All but one of the bridges has been cut using a diamond knife.

2.2.4 Projection Photolithography

Projection photolithography involves patterning the photoresist by means of a projected image of a high contrast mask. In our work, the image is a demagnification of a larger mask. In this way we can make 1-2 μ m wide strips with uniform widths from larger strips, whose dimensions are easier to control. We accomplish this demagnification by projecting the mask down through a metallurgical microscope onto the substrate. This technique was first used by Palmer and Decker (1973). A diagram of this arrangement is shown in Figure 2-3.

The photoresist-coated substrate is first brought into focus as viewed through the eyepieces. The mask is then positioned such that it is in another of the focal planes of the substrate, available through the illuminator or one of the other ports of the microscope. When the light of the illuminator is directed through the positioned mask, both the substrate and the image of the mask appear in focus to the viewer. While the mask and substrate are being lined up, a red filter is used to block the ultraviolet and prevent exposure of the photoresist. When everything is in focus and the substrate has been rotated and/or translated so that the mask pattern appears in the desired location, the red filter is removed and the photoresist is exposed for a fixed amount of time. More information will be given about our specific setup in the next subsection.

The exact time of exposure of the photoresist is quite important. Underexposure by ~10% can result in incomplete removal of the

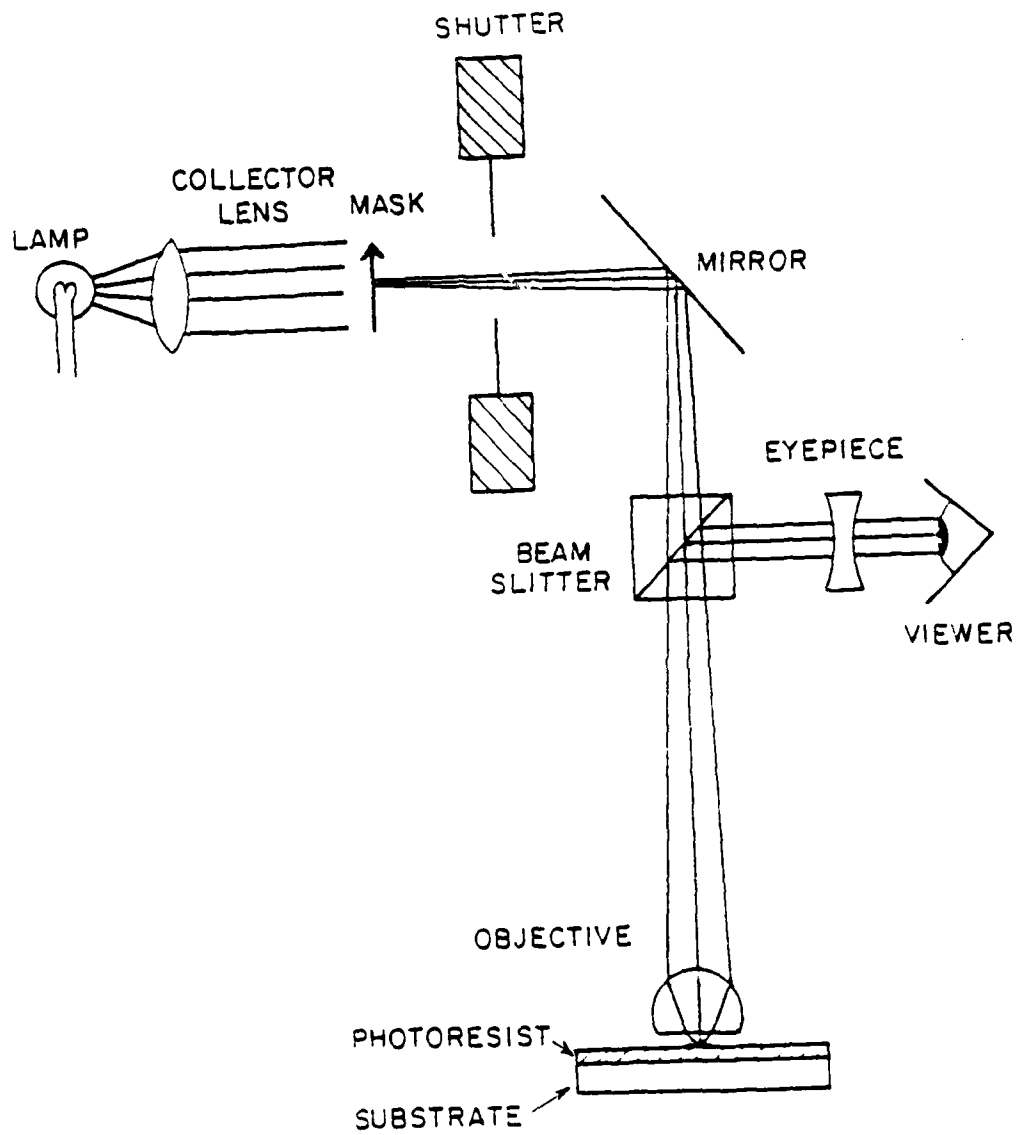


Figure 2-3 Schematic illustration of the technique of projection lithography.

photoresist during development. Overexposure by ~20% can result in observably wider lines. Since the exact time required depends on substrate reflectivity, photoresist thickness, temperature, illuminator setting, developer concentration, and duration of the developing, best results are obtained by running a set of test exposures first on an identical, but spare, substrate, subject to the same conditions as will be used on the real thing. After the test substrate is developed and inspected, the exposure time that gave the best test result can be used to make the desired sample.

All of our indium samples have been made by projection photolithography used in conjunction with contact printing. The contact printing was used to define the larger areas where contact to the coaxial cables would be made. After the contact print exposure, the photoresist was developed so that the pattern could be viewed in the microscope. Then projection was used to define the microbridge in the appropriate place. The sample was again developed to remove the newly exposed photoresist. (This second developing of the same photoresist does not change the first pattern since all of its exposed photoresist was removed the first time.)

Next, the substrate and its composite-patterned photoresist layer were attached to a cold stage in a vacuum evaporator. They were cooled by liquid nitrogen to 77 K before the indium was evaporated from a molybdenum boat at $10\text{--}20\text{\AA}/\text{sec}$ with the pressure in the 10^{-7} range. Fortunately, the cooling did not cause any problem with the photoresist, since evaporation onto room temperature substrates was found to result in such lumpy films that the microbridges were discontinuous. An

example of an indium bridge fabricated by this procedure is shown in Figure 2-4.

2.2.5 Fabrication Facilities

To do the photolithography we have described, we purchased and set up a variety of equipment with the help of the entire superconductivity group at Harvard. We were also aided by visits to Massachusetts Institute of Technology's Lincoln Laboratories and by a course on microfabrication.

Contact printing requires a dust-free environment because dust prevents good optical contact between the mask and the photoresist. (If they are separated by more than a few wavelengths of light, diffraction fringes cause improper line widths.) Two laminar flow hoods were obtained and a clean room was set up in order to achieve the necessary reduction in airborne dust. The two flow hoods have 99.99+% efficient HEPA (High Efficiency Particulate Air) filters and, if properly maintained, meet or exceed the requirements of Class 100 (Federal Standard 209A). According to specifications, the particle count does not exceed 100 particles 0.3 μ m or larger per cubic foot. Laminar flow means that there is a uniform (laminar) flow of air through the entire work space. This is important because it prevents dust from entering the air flow by way of turbulence.

One of the hoods is a horizontal laminar flow hood (air flows out of the back toward the user) in which the contact printing and (after

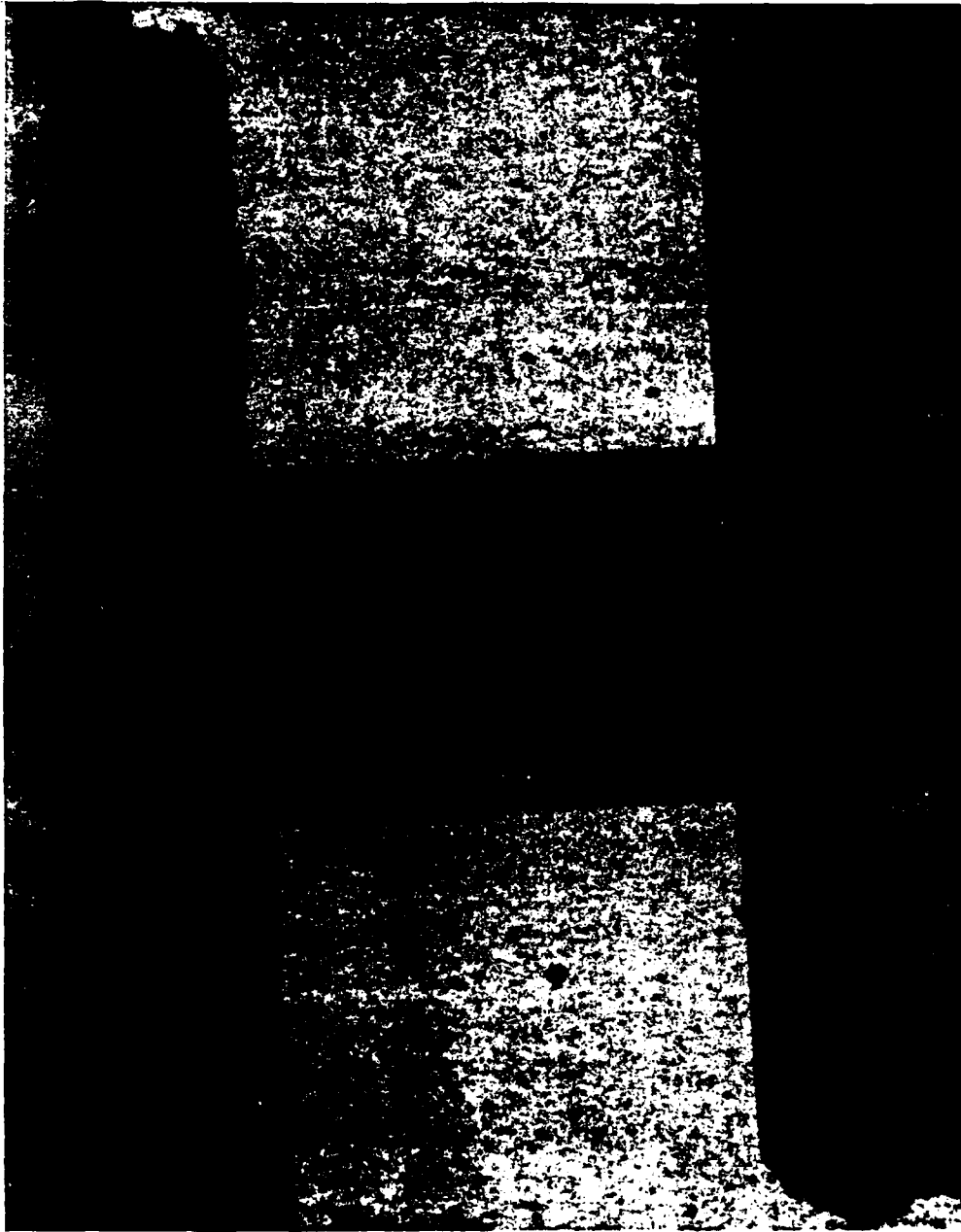


Figure 2-4 Indium microbridge made by projection photolithography. The mask used to make this 50 μ m long bridge was made by IBM.

the microscope was bought) the projection photolithography are done. The other hood is a vertical laminar flow hood. The working surface is perforated stainless steel and the air flows down out of the top, through the working surface, and is partly recirculated, partly exhausted out of the building. The photoresist spinner was mounted in the center of the vertical flow hood and a small hotplate oven was placed in one corner. The various chemicals that were needed were also placed in it. Thus configured, all photoresist processing except exposure is done in the vertical hood. Exposure of the resist is done in the horizontal hood, which is positioned next to the vertical hood. This can be seen in Figure 2-5, which shows the present layout of the room.

As indicated in the Figure, these hoods were placed in the same room as the vacuum evaporator. The room was converted to a medium quality clean room by upgrading the filter on the air-conditioner to one that was 60% efficient and by running the flow hoods whenever using photoresist. Since both the fume hood and the vertical laminar flow hood exhaust air out of the room, filters were used on the large vent in the door where most of the air is drawn into the room. The mechanical pump for the evaporator was removed to the next room, as it seemed to be a source of considerable filth. Ports were made through the wall so that gas cylinders and liquid nitrogen need not be brought into the room.

Since photoresist is exposed by blue and ultra-violet light, the fluorescent bulbs and all other lights in the room were covered with yellow plastic sleeves. Furthermore, the lower halves of the windows

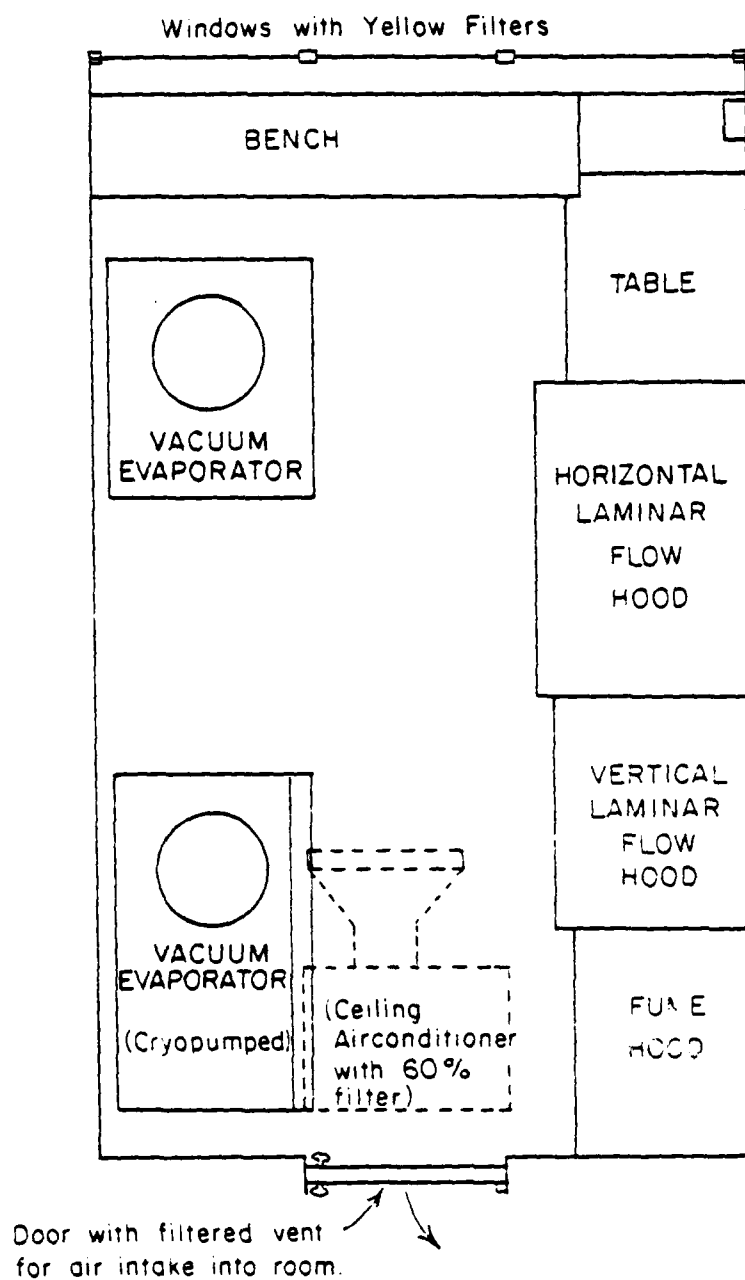


Figure 2-5 Physical layout of the Harvard "clean" room. The mechanical pumps for the evaporators and all necessary gas cylinders are located in the next room to the left on this diagram.

were filtered with yellow plastic sheeting and the upper halves were covered with aluminum foil to block out the light altogether. To keep grease off of samples and hence enhance reliability, everyone wears disposable plastic gloves when they work in the hoods. Smoking and entry by unauthorized personnel were prohibited by a large sign on the door of the room.

Initially, an old Reichert MeF2 microscope was used for the projection photolithography. When money became available, we purchased a Zeiss Universal metallurgical microscope and placed it in the horizontal flow hood as previously mentioned. The microscope has four objectives (8X, 16X, 40X, 80X) that can be used for both reflection and transmission illumination. It also has a camera for use in documenting results.

The important feature of the microscope for use in projection is a six-position, three-port beam splitter. We attached the camera to one of the ports and built a projection attachment for one of the other ports. Figure 2-6 shows a diagram of this attachment. It was designed so that the mask could be moved back and forth along the z axis by a single knob, and has several smaller adjustments for the tilt of the mask. These adjustments make it possible to position the mask exactly in the image plane of the objective, as was described in the previous section. The mask is mounted in an easily changed holder on an X-Y stage so it can be properly positioned in the field of view. There is a slot where the necessary red filter can easily be slipped in and out.

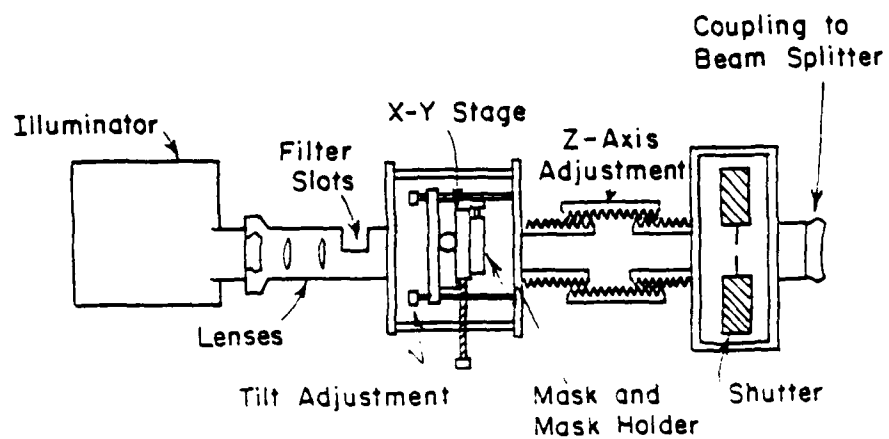


Figure 2-6 Diagram of the projection attachment for our microscope. The illuminator is the same one that is used with the microscope for ordinary illumination. The z-axis adjustment uses left-handed screw threads on the left and right-handed threads on the right.

The same lamp is used as for the rest of the microscope; it is simply removed from its usual place and attached to this projection apparatus. Two lenses are included to transform the light source into that which is most appropriate for the optics. The attachment is made almost entirely of aluminum to reduce the weight and it is anodized black to reduce reflections.

Very reproducible exposures are provided for by use of a Vincent Associates electromechanical shutter driven by a crystal controlled timer. The shutter is spring mounted to reduce vibrations. We designed the timer specifically for this projection attachment. Using it, the exposure time can be set to four digit accuracy in each of three ranges: 9.999, 99.99 and 999.9 seconds. It also provides a small amount of audio feedback to the user while it is running.

2.3 Early Harvard Experiments

Our initial experiments at Harvard depended mostly on equipment that already existed in the laboratory. Figure 2-7(a) shows a block diagram of the electrical arrangement of these experiments. The pairs of wires shown are 50 Ω coaxial transmission lines; all inputs and outputs are matched to this impedance. The microbridge is connected across the transmission line and, hence, is effectively located in the circuit shown in 2-7(b), where the 50 Ω resistors represent the source and termination impedances. This circuit is exactly equivalent to 2-7(c) in which the 25 Ω source resistance is the load line seen by the microbridge. It results from the two 50 Ω resistors in parallel. This

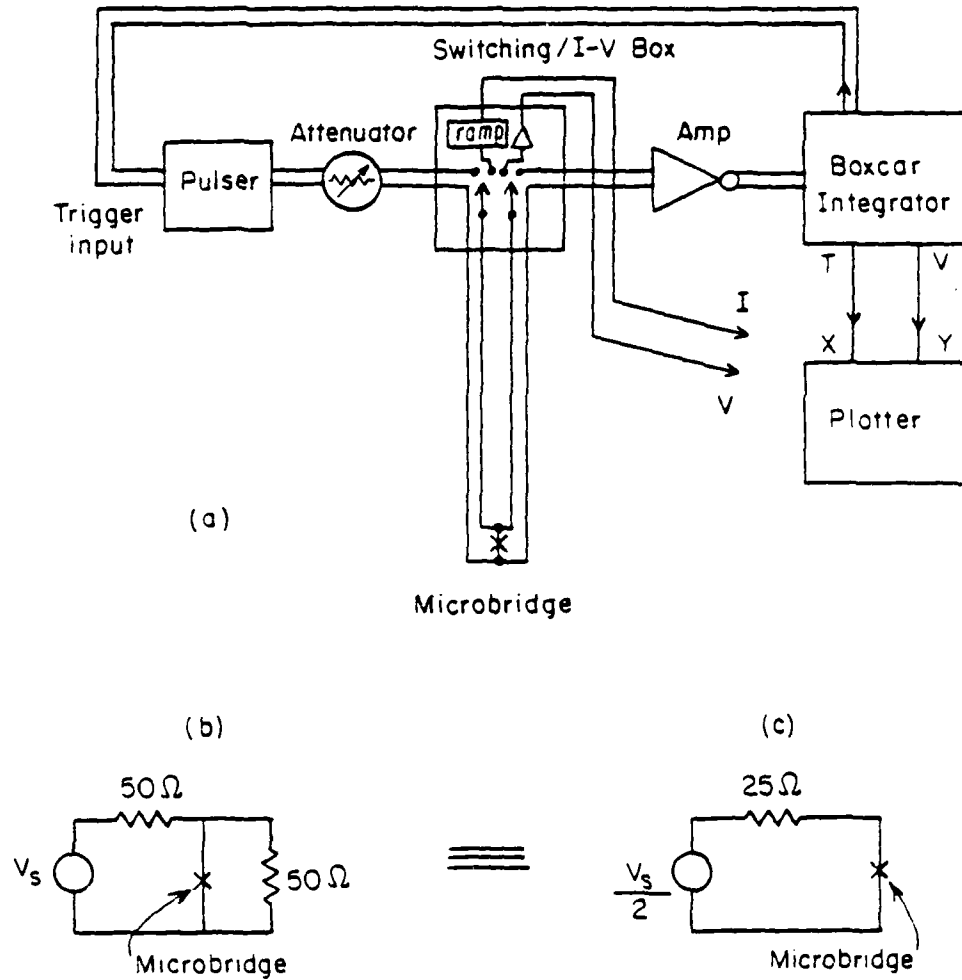


Figure 2-7 Electrical setup used in the Harvard experiments. (a) shows a block diagram of the entire setup. (b) shows the effective electrical environment of the microbridge and (c) is an equivalent circuit.

load line means that the strip is not truly current biased as in the simple description of the experiment. For low resistance strips, where $R_{N \text{ sample}} \ll 25\Omega$, the difference between this setup and true current biasing should be negligible. The behavior of high resistance samples may, however, be modified. In either case our theoretical calculations take into account the load line.

One of the limiting factors in our early experiments was the pulse generator that was used. Since there was not a suitable one in the lab, a simple one was built. A partial schematic diagram of it is shown in Figure 2-8. It uses ordinary TTL (transistor-transistor logic) integrated circuits powered by a 5V supply offset from ground. This was done so that it could put out variable-height negative-going pulses that would take advantage of the fall time of the open collector output, which is shorter than its rise time. The resistors on the output of the TTL driver were chosen so that the source impedance would be 50Ω during the pulses. The pulse generator was made to be externally triggered by the boxcar integrator, which was used to detect the signal, in order to eliminate the need for a pretrigger for the boxcar. The trigger input is completely AC coupled in order to prevent ground loops.

The output of the pulse generator goes directly into a W and G Instruments RT-1 continuously variable attenuator that covers the range -10dB to -70dB. Later measurements with a sampling scope indicated that its bandwidth was about 4GHz. The combination of the relatively coarse attenuator and the more finely adjustable height from the pulser allowed us to obtain any pulse height we wanted.

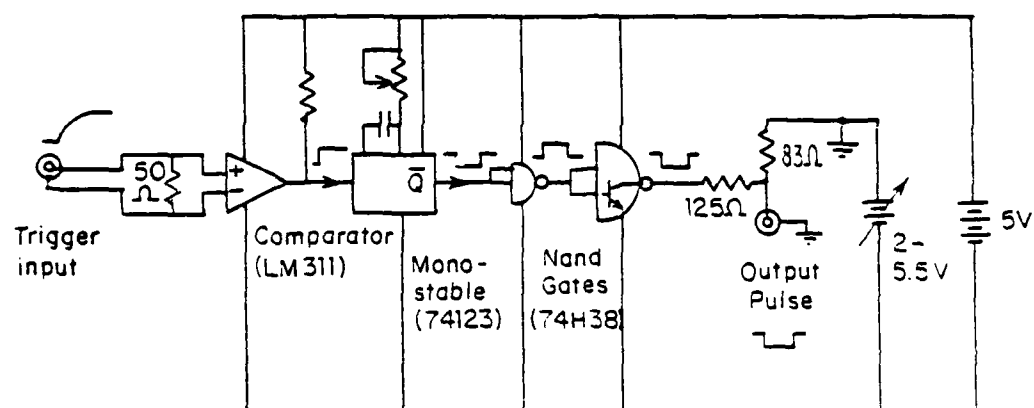


Figure 2-8 Schematic diagram of the TTL pulse generator used in the early Harvard experiments. The input is floating to prevent a ground loop.

Next the pulse goes through a switching box before entering the cryostat. The switching/I-V box allowed us to switch from voltage-time measurements to an I-V mode. In the latter mode we could observe the I-V curve either on an oscilloscope or on a plotter, and thus determine the critical current and normal state resistance of the strip. The box contains the variable-speed current ramp and the instrumentation amplifier that are used to make the I-V curves.

The pulse then goes into the cryostat. A very simple cryostat was used, consisting mostly of two 50 Ω semi-rigid stainless steel coaxial cables that extended nearly to the bottom of the liquid helium dewar. All experiments were done with the samples directly immersed in the liquid helium.

The sample was attached to the cables as illustrated in Figure 2-9. The outer conductors of the cables are attached to the large copper block which forms the local ground. One of the microbridge contact pads is pressed against an indium coated protrusion from this copper block to form the ground contact. The other contact pad is pressed against a small indium-coated copper block that is soldered to both of the cable center pins. The pressure is applied by screws between the copper flat beneath the substrate and the large copper block. Indium is used on the contacts because when it is smashed under the pressure it forms good electrical connections.

A germanium resistance thermometer is attached to the copper flat to monitor the temperature independently of the helium pressure. A heater resistor and a carbon resistor thermometer are also located near

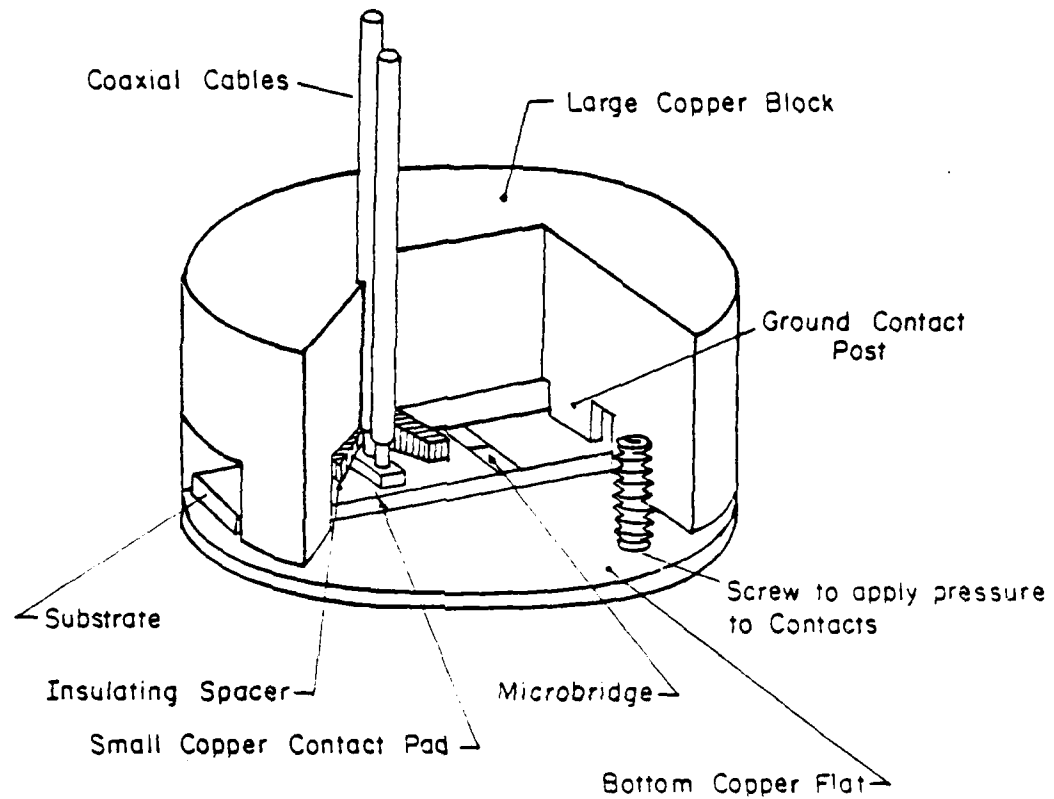


Figure 2-9 Cut-away view of the setup used to connect the samples to the coaxial cables. The large copper block is connected to the shields of the cables and forms the local ground. The copper flat on the bottom is used to press the sample against the small copper contact pad and the ground contact post.

the sample and are used in conjunction with a feedback system to control the bath temperature when operating below the lambda point of liquid helium. This is a standard temperature controller system consisting of an AC bridge and lock-in amplifier to measure the resistance of the thermometer resistor and a simple proportional/integrating feedback circuit to drive the heater resistor. It was found to provide stabilization to at least $\pm 0.5\text{mK}$ for our experiments on dirty aluminum. For the measurements on indium, the temperature was controlled by regulating the pressure above the bath.

After the voltage signal comes out of the cryostat and goes through the switching box, it is amplified by a Hewlett Packard 461A wideband amplifier. This amplifier has a bandwidth of 1kHz-150MHz and gains of 20dB and 40dB. Its equivalent input noise is 40 μV and it has a rise-time of $\sim 2\text{ns}$.

This amplified signal was fed into a PAR 160 Boxcar Integrator. This instrument had a rise-time of about 20ns and hence was the limiting factor in these experiments. The boxcar was hooked directly to a plotter and would slowly scan through time, averaging the signal at each time and recording the voltage waveform. An example of its output for a "dirty" aluminum microbridge is shown in Figure 2-10(a). This family of waveforms was taken at fixed $T=1.516\text{K}$ by varying the height of the current pulse, I_p . Note that the delay time varies from 300ns for $I_p/I_c=1.013$ to times too short to resolve at larger ratios. The analysis of this data is given in Chapter 5.

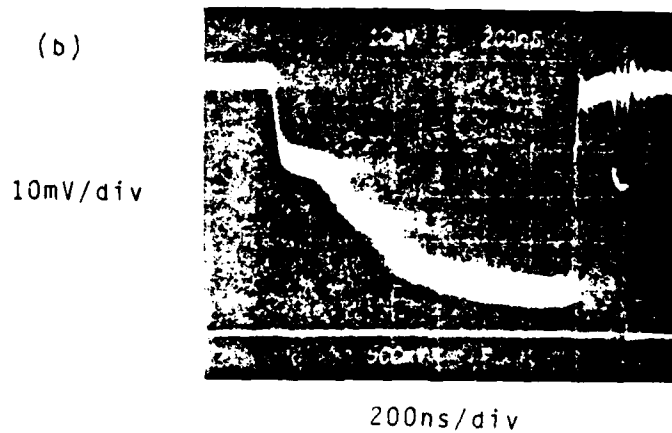
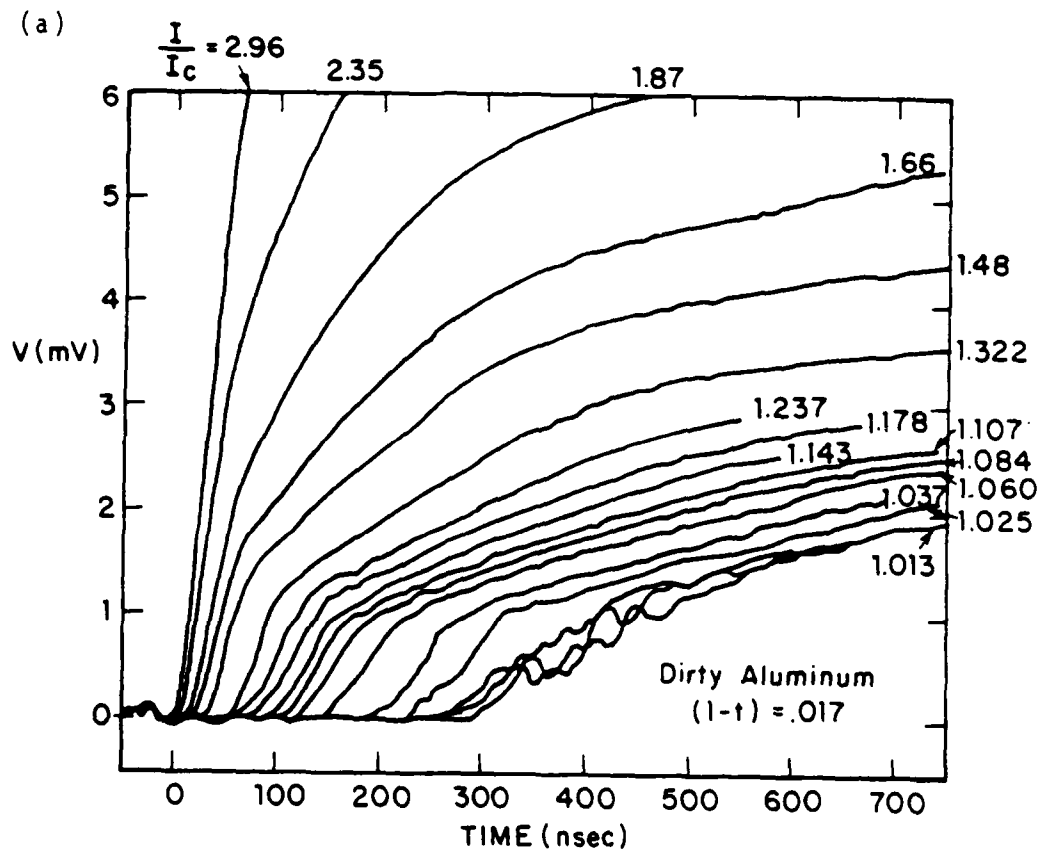


Figure 2-10 Examples of voltage waveforms taken on dirty aluminum. (a) shows waveforms taken at fixed temperature and a range of values of I/I_c using the Boxcar Integrator. (b) shows an example of a trace taken directly on the oscilloscope.

Some of our high resistance aluminum samples had a signal-to-noise ratio high enough that we could observe the voltage coming out of the amplifier directly on a Tektronix 7704A oscilloscope using a 7A24 plugin. Since this combination has a 2ns rise-time, we used this method to make some of the delay time measurements directly on the oscilloscope screen. A photograph of a typical trace is shown in Figure 2-10(b). (The current pulse is negative and, hence, the uninverted voltage transition is also negative.)

In our initial experiments we did not have access to a sampling plug-in for our oscilloscope. Later we were able to borrow one from another research group. This unit, a Tektronix 7S12 Time-Domain Reflectometer with an S-6 sampling head (30ps rise-time) and an S-53 trigger recognizer head, enabled us to make much higher frequency measurements and to easily plot the results via some outputs on the front of the unit. Now that we had this very wide bandwidth voltage measuring device, the minimum delay time that we could observe was limited by our pulse generator and by the wide-band amplifier.

2.4 Recent Harvard Experiments

In our more recent experiments at Harvard we have greatly increased our time resolution by making improvements in the limiting aspects of our previous experiments. We have built a new pulse generating system using a tunnel diode for the source of the pulse. We have improved the cryostat by use of better coaxial cables and by mounting most of the circuitry directly on top of the cryostat to shorten the lines. We have

also obtained a much wider bandwidth amplifier.

The pulse generator system is based on the switching of a tunnel diode across its negative resistance region. The system is described only briefly here; a more complete description is given in Appendix A. The tunnel diode approach was chosen because it is the fastest known way of creating voltage steps with available semiconductor technology. The diode we used is in principle capable of making a 450mV jump in about 22ps. Commercial pulse generators are available that use this principle, but unfortunately we could not use them because they had unacceptable baselines.

The pulser we have made has an adjustable baseline, so that, in particular, we can set the baseline to be zero. Alternately, we can vary the baseline as a way of effectively varying the pulse height. The 10%-to-90% rise-time of our pulses is about 275ps. This is longer than we had hoped for, but still represents a substantial improvement over the old equipment. It self-adjusts the bias current on the tunnel diode to compensate for any drift. During the pulses it measures the height of the source voltage. Between pulses it measures the amount of source voltage needed to exceed the sample's critical current. Using these voltages, which are proportional to I_p and I_c , respectively, as inputs for an analog divider, it creates an output voltage equal to $-I_p/I_c$, i.e., -1.0V when $I_p/I_c=1.0$. This is not an accurate determination of the true I_p/I_c , due to threshold errors in detecting when the critical current has been exceeded. It can, however, be used to monitor the current ratio stability or for feedback to stabilize the current ratio.

Several improvements were made to the crystat. The old one had used .085" diameter stainless steel coaxial cable. The new version used .141" diameter copper-sheathed stainless steel coaxial cable, which has much better frequency response. Another improvement was that both the pulse generator and the wideband amplifier were mounted on top of the crystat. Less than three inches of semi-rigid copper coaxial cable were required to make the connections between the electronics and the cryostat cables. Furthermore, SMA connectors (rated to 18GHz) were used on all of the high frequency connections.

A new sample geometry and a new configuration for connecting to it were also used. These are shown in Figure 2-11. The sample was mounted in the vertical plane and the pad areas were made into 50 Ω striplines to minimize reflections in the transmission lines. Contact was made to the sample by pressing the indium coated center pins of the coaxial cable directly against the sample. The pressure was applied through a fairly thick insulating material so as not to change the electrical characteristics of the connections.

The new wide-band amplifier that we used was a B and H Electronics DC-3002AL. Its bandwidth is DC to 3.15GHz and it will put out 4dBm (1.5mW, 270mVrms) into 50 Ω . Its gain is about 22dB, it has a noise figure of 3.5dB below 1GHz and its rated rise-time is 140ps. Using this we can take much better advantage of the bandwidth of our sampling unit. The only drawback to this amplifier has been that its input impedance is only about 35 Ω , which results in the reflection of a significant portion of the signal back to the sample. We have reduced this effect by adding a 15 Ω resistor in series with the input. This decreases the

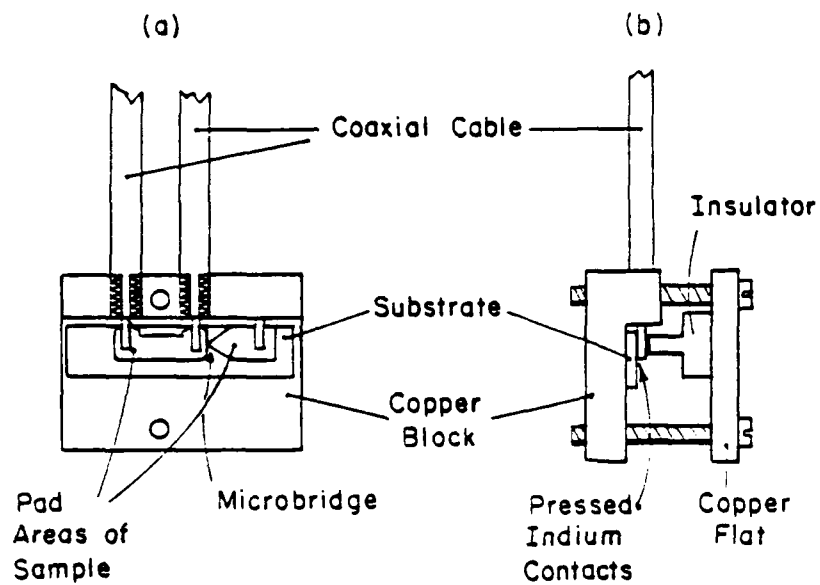


Figure 2-11 Scheme used to make contact to the samples in the later Harvard samples. The center conductors of the coaxial cables are tinned with indium and pressed directly against the sample's pad areas.

reflections, but degrades some of the high frequency characteristics of the amplifier.

The indium strips that we have tested have had normal state resistances of $\sim 1\Omega$ at T_c . The differential resistance per phase slip center was only $\sim 0.1\Omega$, however, which means that when I_c is $\sim 100\mu A$, the voltage associated with each phase slip center is only $\sim 10\mu V$. Even after the $\sim 10X$ wide-band amplifier, this signal is too small to be resolved with our Tektronix sampling unit. We therefore used a synchronous technique to observe the signal.

To explain this method, it is easiest to consider first the simpler circuit shown in Figure 2-12(a). In it a simple feedback loop serves to stabilize the I/I_c at which one is making a measurement. The circuit consists of two op amps. The first one forms the difference $V' = 2V_{ref} - (-I_p'/I_c) = 2V_{ref} + I_p'/I_c$, where $I_p' = I_{step} + I_{baseline}$. The second one integrates the difference signal V' , increasing or decreasing the baseline, until $V' = 0$. It then continues to adjust itself so that $V' = 0$, even if I_c (for example) changes. Thus, it forces $I_p'/I_c = -2V_{ref}$ (V_{ref} is negative).

The synchronous method uses the above principle, except that it has two feedback paths stabilized to different reference voltages, and switches back and forth between the two (Figure 2-12(b)). This has the effect of switching the pulse height back and forth between two different values of I_p'/I_c . As shown in the Figure, a PAR 124A lock-in amplifier is used on the output of the sampler to synchronously detect the voltage changes caused by these I_p'/I_c changes. In practice, one of

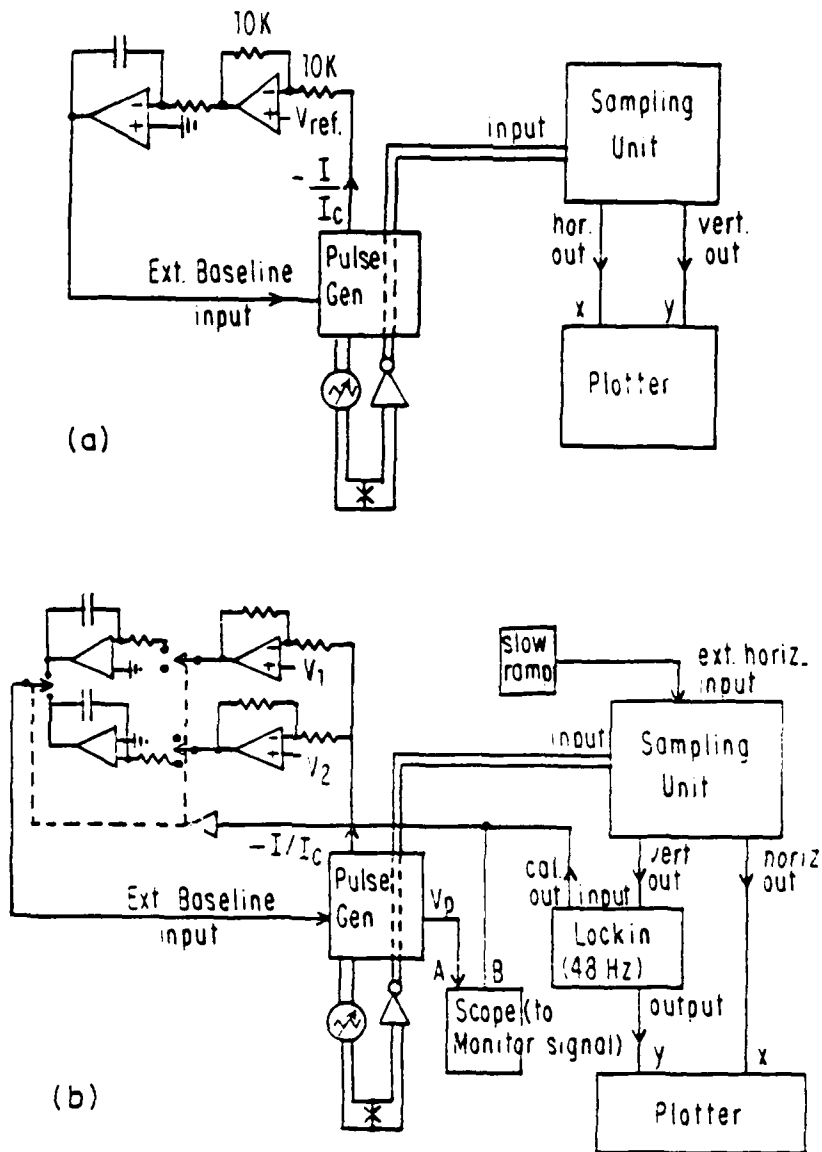


Figure 2-12 Block schematic diagram of (a) the feedback-stabilized I/I_c circuit and (b) the synchronously detected chopped-feedback-stabilized circuit used to improve sensitivity for low resistance samples. Both of these use the tunnel diode pulse generator.

the two is set such that $I_p'/I_c < 1.$, in which case the strip remains superconducting, and the synchronously detected voltage is precisely the signal voltage we wanted to measure. Figure 2-13 shows some waveforms that were taken in this way. Notice the excellent voltage sensitivity for a bandwidth in excess of 1GHz. The ringing is believed to be due to the amplifier mismatch and appears in this synchronously taken data because of slight shifts in when the pulse is triggered that occur when the baseline is shifted. The interpretation of the data in this Figure and the rest of data will be discussed in Chapter 5.

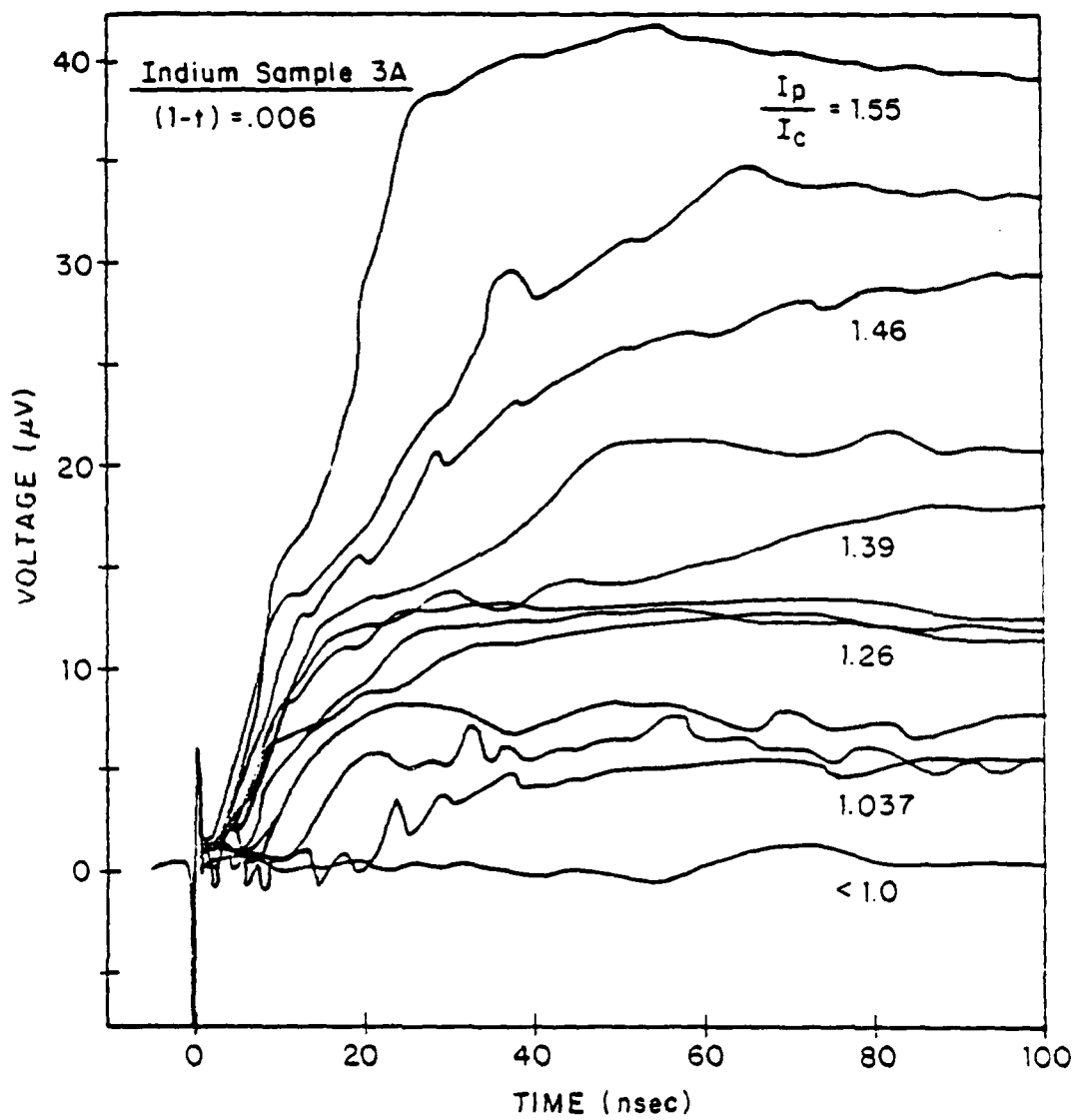


Figure 2-13 Voltage versus time waveforms for an indium microbridge taken using the circuit shown in Figure 2-11.

CHAPTER III

EXPERIMENTAL TECHNIQUES--IBM EXPERIMENTS

3.1 Introduction

In addition to taking data with the conventional electronics discussed in the previous chapter, we have also taken data using superconducting circuitry in a collaboration with A. Davidson and S. Faris at the IBM Watson Research Center. In this chapter we discuss the details of these collaborative experiments.

The experiments were done on a superconducting integrated circuit made by IBM in a project designed to use their Josephson junction technology in some fundamental scientific experiments. Our particular experiment was only a small part of each chip, consisting of two Josephson junction pulse generators, two sets of two pads between which we fabricated the microbridges, and a Josephson junction sampling circuit invented by Faris (Faris and Pedersen 1981).

There are several significant advantages of this entire approach over our more conventional experiments at Harvard. The interferometers of which the circuit is constructed are intrinsically very fast. The sampling circuit is thought to have a time resolution of better than 10ps and the rise-time of the pulse generator should be less than ~100ps. As a result, we were able to make measurements on a superconductor with shorter time constants than aluminum. We chose to use indium and, for the most part, obtained very good results. Two

other very important advantages of these circuits were the excellent sensitivity of the sampler and the common ground plane of the entire circuit which greatly reduced ringing problems. Due to these characteristics, we were able to make the first accurate waveform measurements of the entire initial transient in these supercritical current pulse experiments.

In the next section, we will briefly discuss the characteristics of Josephson devices to provide a background for our description, in Section 3.3, of the superconducting circuitry that we used for this experiment. In Section 3.4 we will briefly mention the fabrication details of this work, and in the last section we will discuss the remaining experimental details.

3.2 Josephson Junctions

A Josephson junction is formed when two superconductors are separated by a thin insulating barrier through which electrons can tunnel. Josephson showed, in 1962, that the Cooper pairs of a superconductor can tunnel through such a barrier coherently (Josephson 1962). As a result, a supercurrent can flow through the barrier without any voltage drop. Furthermore, it can be shown that for a simple point junction this supercurrent obeys the Josephson relation, $I = I_0 \sin(\varphi = \varphi_1 - \varphi_2)$, where the critical current, I_0 , is the maximum supercurrent that can be passed through the junction and φ_1 and φ_2 are the phases of the superconducting order parameter on the two sides of the junction.

When the current through such a Josephson junction is forced to exceed I_0 , the junction switches from the zero voltage state to a state in which there is net average voltage across the junction, the phase, φ , continuously advances, and the quasiparticles carry the extra current. For junctions such as those usually used in logic, the voltage switched to is $\sim 2\Delta/e$. This case is illustrated in the I-V curve in 3-1(b), where R_L is the load line on which the junction has been biased. To get back to the zero voltage state in such a junction, the current must be decreased to near zero.

When Josephson junctions are extended to one or two dimensions, their critical current depends on the magnetic flux through the junction. For a symmetric extended junction, the critical current takes the form of a Fraunhofer diffraction pattern, that is, $I_0(\Phi) = I_0(0) \sin(\pi\Phi/\Phi_0) / (\pi\Phi/\Phi_0)$, where Φ_0 is the superconducting flux quantum, $hc/2e = 2.07 \times 10^{-7} \text{ gauss-cm}^2 = 2.07 \text{ mApH}$. An example of such a junction and its I_0 versus Φ curve is shown in Figure 3-1(a).

Unfortunately, such junctions do not make good high speed switching devices because any junction large enough to be reasonably sensitive to magnetic fields also has a relatively large capacitance. As a result, they will not switch very fast. Much of the capacitance can be removed, however, by simply taking out the middle of the junction and leaving a pair of much smaller junctions, one at each end. This is simply the conventional two-junction SQUID.

The schematic diagram of such a SQUID used as a logic gate with a control line is shown in Figure 3-1(b). For this device, the flux is

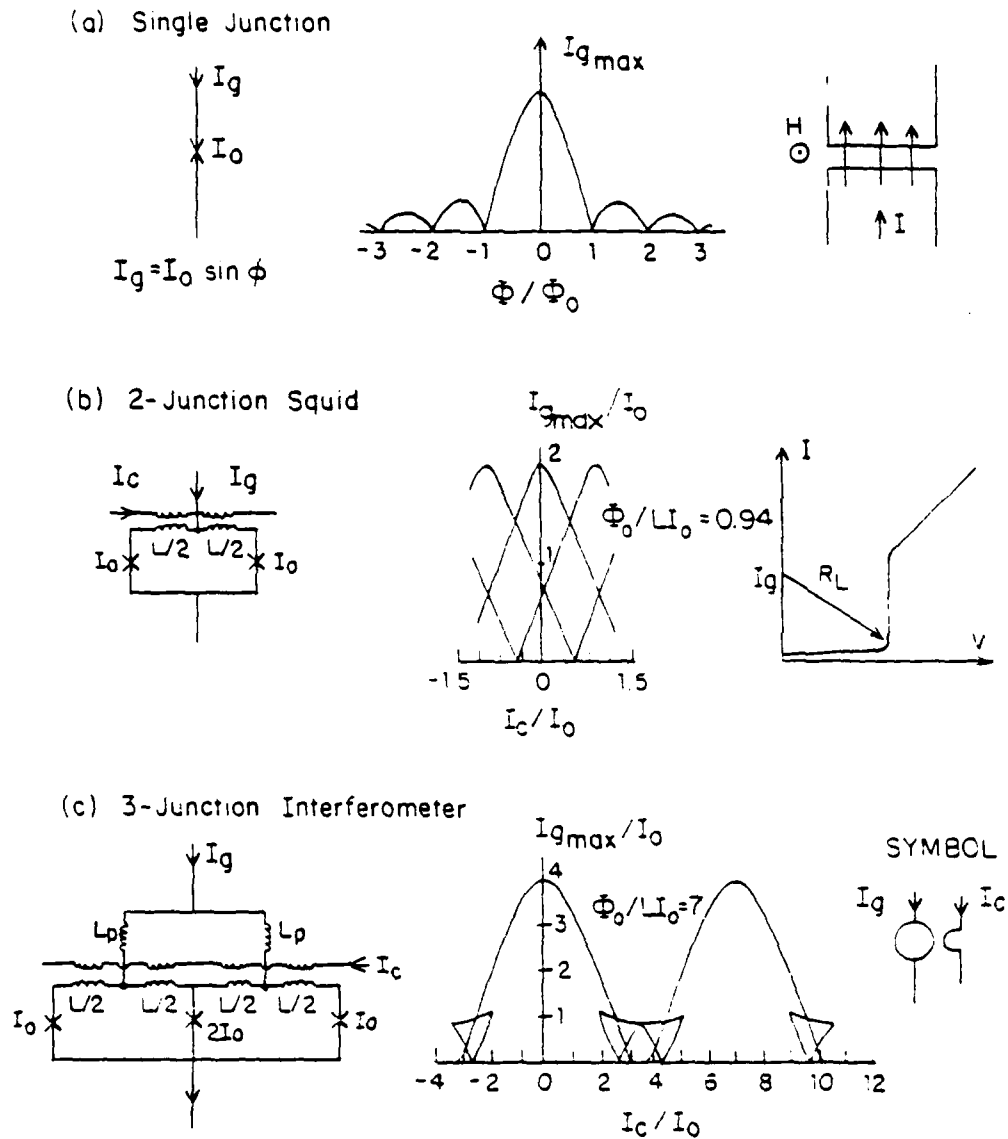


Figure 3-1 Josephson junction logic gates and threshold curves. (a) shows a single junction and its dependence on magnetic field. (b) shows a 2-junction SQUID with a control line and its dependence on control current, and (c) shows the same for a 3-junction interferometer. Taken from Matisoo (1973), Faris and Davidson (1979) and Jillie (1980).

directly proportional to I_c' , the control current, and $I_0(I) = I_{gmax}(I_c')$ is the maximum bias current that can be applied to the gate before it switches into the voltage state. This I_{gmax} , as a function of I_c , is shown in Figure 3-1(b). The different lobes correspond to different integer numbers of flux quanta in the loop. (Quantization of the flux in the loop is a result of the single-valuedness of the superconducting wavefunction.) In operation, such a device would be biased at a fixed gate current I_g on a load line R_L , as shown in its I-V curve in Figure 3-1(b). Assuming that it was brought up to this I_g level with $I_c = 0$, the junction would be in the zero voltage state. It can then be switched to the voltage state by applying a control current such that $I_{gmax}(I_c') < I_g$. Since these devices are usually hysteretic, it would very quickly switch to the voltage state upon the application of such an I_c , and would remain there until I_g was decreased to near zero. Note that for a given $I_g < I_{gmax}(0)$, there are several ranges of currents that can be passed through the control without causing switching. The control currents at the edges of these regions are called the thresholds. Hence, the $I_{gmax}(I_c)$ versus I_c curve is often thought of as the threshold curve, since, for any given I_g , it shows the control currents at the boundaries between switching and non-switching.

Unfortunately, such two-junction SQUIDS do not usually make good logic elements because of their small operating range. (I_g must be quite close to I_{gmax} and the control current cannot be very large, since if it reaches the next lobe, the gate may not switch reliably.) This problem can be solved by using a three-junction interferometer, which has a much larger operating range, but has the same I-V curve and mode

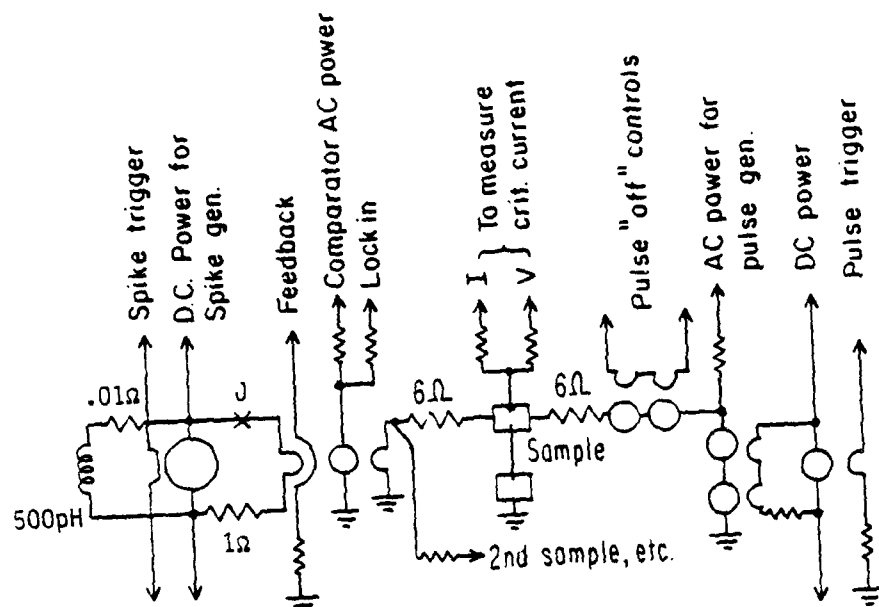
of operation as the simpler SQUID. An example is shown in Figure 3-1(c). Note that the lobes of the I_{gmax} versus I_c curves are much better separated, thus allowing a much wider range of control currents and I_g 's for proper, reliable operation.

Because of these advantages, these last devices are the type used in the circuitry for our experiments.

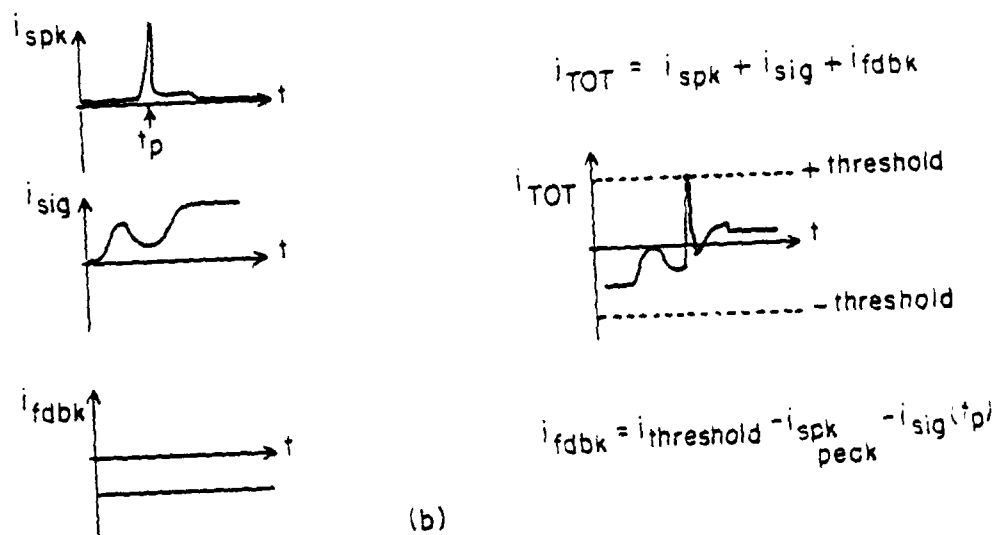
3.3 The Superconducting Circuitry

A schematic diagram of the sampler and pulse generator circuits is shown in Figure 3-2(a), where each of the small circles represents a three junction interferometer like the one in Figure 3-1(c). From left to right, the circuit consists of a spike generator, a comparator, the sample, a pulse generator and a trigger circuit for the pulse generator. Each chip actually contained two samples and two pulse generator and trigger circuits, one for each sample, attached to the same comparator, but for clarity, only one sample, etc., is shown in the figure.

The spike generator works as follows. When a trigger pulse occurs on its control line, the interferometer switches very quickly to its voltage state. As it does so, its bias current is diverted to its output loop (to the right of the interferometer), where the current rapidly increases until it reaches the I_0 of Josephson junction J. When this happens, J switches to its voltage state and most of the current is switched back out of the output loop and into the quasiparticle current of the interferometer. Thus, a very short spike of current has occurred in the output loop. The whole circuit is made self-resetting by the



(a)



(b)

Figure 3-2 (a) Schematic diagram of the IBM superconducting circuitry and (b) An illustration of the operation of the Faris sampler.

inductor and resistor to the left of the interferometer. During an $\frac{L}{V}$ time of $\sim 200\text{ps}$ they take up most of the current through the interferometer, so that it switches back to its zero voltage state. After the currents have readjusted, the spike generator is ready for another trigger pulse.

The sampling scheme invented by Faris consists of both the spike generator and the comparator with its three control lines. Figure 3-2(b) illustrates how it works. The currents through the three control lines of the comparator are shown as a function of time in the left half of the figure. The current through the output loop of the spike generator is i_{spk} , i_{sig} is the current from the sample ($=V_{\text{sample}}/6\Omega$) and i_{fdbk} is a feedback current (constant on this time scale) provided by the external circuitry. The comparator in essence sums up all of these currents and only switches to its voltage state when the sum exceeds one of its thresholds. Provided that the overall variation in i_{sig} is less than the height of i_{spk} , this switching can be arranged to occur only during the spike. Since the junctions are hysteretic, the comparator remains switched until its bias current is decreased to zero and it resets. Thus, the effect of the circuit is to make a test at the time of the trigger pulse, t_p , to determine whether or not $i_{\text{spk}} + i_{\text{sig}} + i_{\text{fdbk}}$ exceeds the threshold of the comparator, and to hold the result of that test until its bias current is removed.

Using this simple yes/no circuit, i_{sig} at time t_p is determined by adjusting i_{fdbk} so that the total current sensed by the comparator at the peak of i_{spk} is exactly equal to its threshold. An accurate determination of this i_{fdbk} requires averaging over many repetitions of

the same waveform, since thermal noise on the signal will cause the comparator to switch during some of the cycles, and not during the others. We define i_{fdbk} as that current which causes the comparator to switch during 50% of the cycles. Clearly, the more cycles over which the averaging is done, the better i_{fdbk} can be determined. Since $i_{fdbk}(t_p) = -i_{sig}(t_p) + (i_{threshold} - i_{spk})$, the signal current is simply the negative of the feedback current, plus a DC offset that can easily be removed.

Figure 3-3 shows a block diagram of the entire electronic setup. In particular, it shows the feedback circuitry used to operate the sampler. The comparator is powered by a pulse generator, with a 50% duty cycle triggered at ~10kHz. This pulse generator also serves as the reference for a lock-in amplifier. The lock-in synchronously detects the voltage output from the comparator and puts out a signal proportional to its average value. The negative input to the lock-in is taken from the reference, and is adjusted so that when the comparator is switching exactly 50% of the time, the output of the lock-in will be zero. This lock-in output is then connected through a current sensing resistor to the feedback input of the comparator. (The phase of the lock-in is set so that the feedback is negative.) Thus, the comparator and lock-in form a feedback stabilized loop which adjusts itself so that the average RMS input to the lock-in at the repetition frequency is very close to zero, and hence, the comparator is switching during almost exactly 50% of the cycles. Since the voltage detected on the current sensing resistor in the output of the lock-in is proportional to the signal current, it goes to the voltage axis on the plotter. The time,

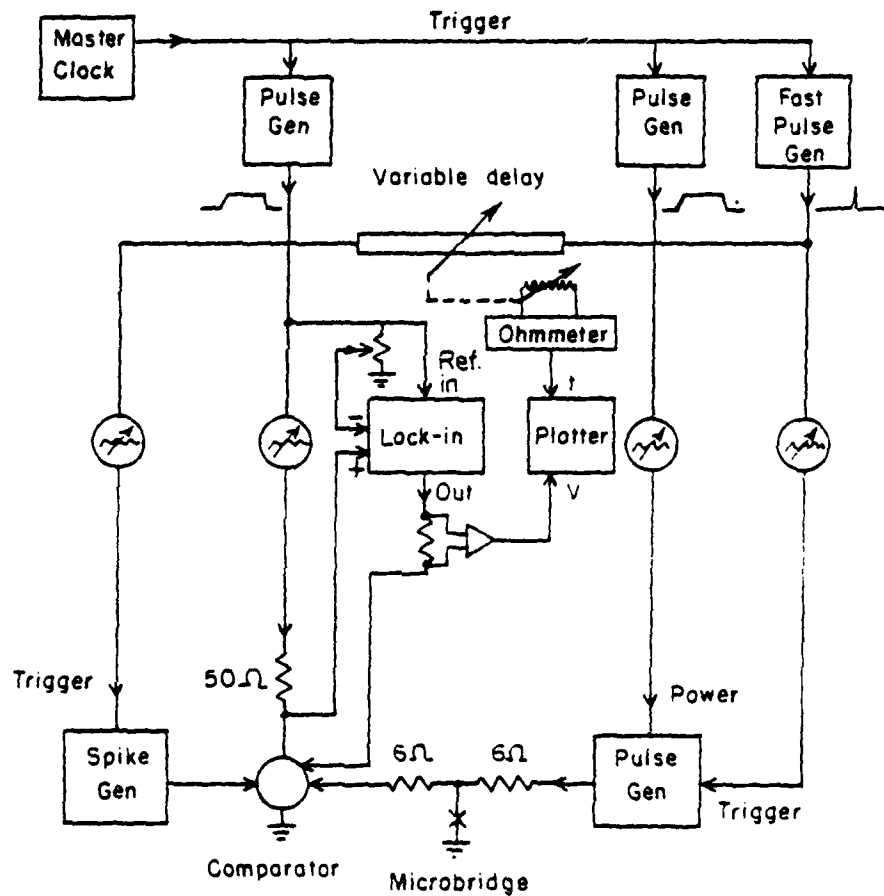


Figure 3-3 Block diagram of the entire IBM experimental setup. The variable resistors in the circles are variable attenuators. The master clock was usually run at $\sim 10\text{kHz}$.

t_p , at which the voltage is being sampled, is determined by a variable length delay line. The length of the line and, hence, the delay are measured electronically by means of a 10-turn potentiometer mechanically attached to the delay line. The resistance of this potentiometer gives the time axis of our plots. Since the variable delay line is also visually calibrated in picoseconds, it is easy to determine the calibration of these time axes.

To do our experiment, we also need to apply a current step to the microbridge. This is provided by the pulse generator circuitry on the right side of Figure 3-2(a). The pulse generator consists of two 3-junction interferometers in series, so that the total voltage put out is about $4\Delta/e$ when the gates switch out of the zero voltage state. This voltage is applied to the sample through a 6Ω resistor, so that the current pulse should have a magnitude of $(4\Delta/e)/6\Omega$. In practice, its magnitude was usually $\sim 750\mu A$, which is a little low, probably because we were not biasing the pulse generator as high as was possible. Note that since these two gates latch into the voltage state, the bias current must be turned off at the end of each cycle to reset them. (There were also a pair of interferometers that could have been used to make this pulse generator into a spike generator or to turn off the output pulse some time after it began, but they were never used.)

Since we require the two interferometers in the pulse generator to switch at essentially the same time, they must have a very short rise-time trigger. This is provided by another interferometer, the furthest one on the right in Figure 3-2(a). The external trigger pulse is applied to this interferometer, and its output in turn is applied to

the two interferometers of the pulse generator. Since this "trigger buffer" is designed to be self-resetting, it is DC powered. Even though it is thus buffered, a very fast external pulse generator (rise-time less than 1ns) is still necessary to minimize time jitter.

For a more complete description of the operation of the sampler circuit, see Faris' original publication (Faris 1980) and for more details about this technology in general, see the March 1980 issue of the IBM Journal of Research and Development, which is entirely devoted to the Josephson computer technology.

3.4 Fabrication Details

As mentioned before, all of the superconducting circuitry was designed and fabricated by IBM. It uses the lead alloy technology that IBM has developed for the Josephson computer project. The circuitry has 5-7 μ m linewidths and 15 distinct layers, most of which are patterned. Table 3-1, which summarizes the different layers and their purposes, is taken from Greiner, et al. (1980), an excellent summary of all the fabrication techniques used in making the chip.

Briefly, (omitting the insulators) first there is a Nb ground plane for the whole circuit. Then there is a Pb-In-Au base electrode layer that forms one side of the tunnel junctions. It is oxidized in the places where junctions are desired and then a Pb-Bi counter-electrode layer is put down to form the other side of the tunnel junctions. Finally, there is a layer of Pb-In-Au that forms the control lines for the gates and interconnections between the various parts of the circuit.

Table 3-1. Layers used in the IBM lead alloy technology.

Layer	Material	Thickness (nm)	Function
M ₁	Nb	300	Ground plane
I ₁	Nb ₂ O ₅	25-35	Ground-plane insulation
I ₂	SiO ₂	145-2 ¹ 5	Ground-plane insulation
R	AuIn ₂	30-43	Terminating, loading, and damping resistors
I ₃	SiO ₂	200	Logic interferometer isolation and resistor insulation
C ₁	Pb-In-Au*	300	Ground-plane contacts and logic interferometer inductance
M ₂	Pb-In-Au*	200	Base electrodes, interconnections, and resistor contacts
I ₄	SiO ₂	275	Junction definition and insulation
I ₅	SiO ₂	275	Memory interferometer inductance and insulation
I ₆	PbO-In ₂ O ₃	6.5	Tunneling barriers
M ₃	Pb-Br*	400	Counter electrodes
I ₇	SiO ₂	100	Counter-electrode protection layer
I ₈	SiO ₂	500	Controls and interconnection insulation
M ₄	Pb-In-Au*	800	Controls, interconnection, and contacts to R, C, and M ₁ layers
I ₉	SiO ₂	2000	Protective layer

*12 wt% In and 4 wt% Au
 *29 wt% Br

Figure 3-4 shows a picture of approximately two thirds of a chip of the type that we used. Our particular piece of this chip is in the upper right hand corner. An enlarged picture of our part alone is shown in Figure 3-5, where the different parts of the circuit are as labelled. Note that our entire circuit occupies less than 1mm^2 .

The microbridges in this figure (not present in Figure 3-4, which shows only the Pb alloy pads) were fabricated at Harvard using the projection photolithography techniques described in the previous chapter. The chip was designed so that such fabrication could be done. Large Pb pads ($50\mu\text{m} \times 125\mu\text{m}$) were provided for the contacts to the indium films, and a $250\mu\text{m} \times 250\mu\text{m}$ hole was left in the SiO passivation layer over the pads so that the contacts could be made. The indium pads used to make contact to these Pb pads were $50\text{-}65\mu\text{m}$ wide and overlapped the Pb by $\sim 30\mu\text{m}$. These large contact areas were used in order to minimize possible contact difficulties between the Pb and the indium. This seems to have been successful, since we have never seen anything in any of the I-V curves that appeared to be due to poor or tunneling contacts.

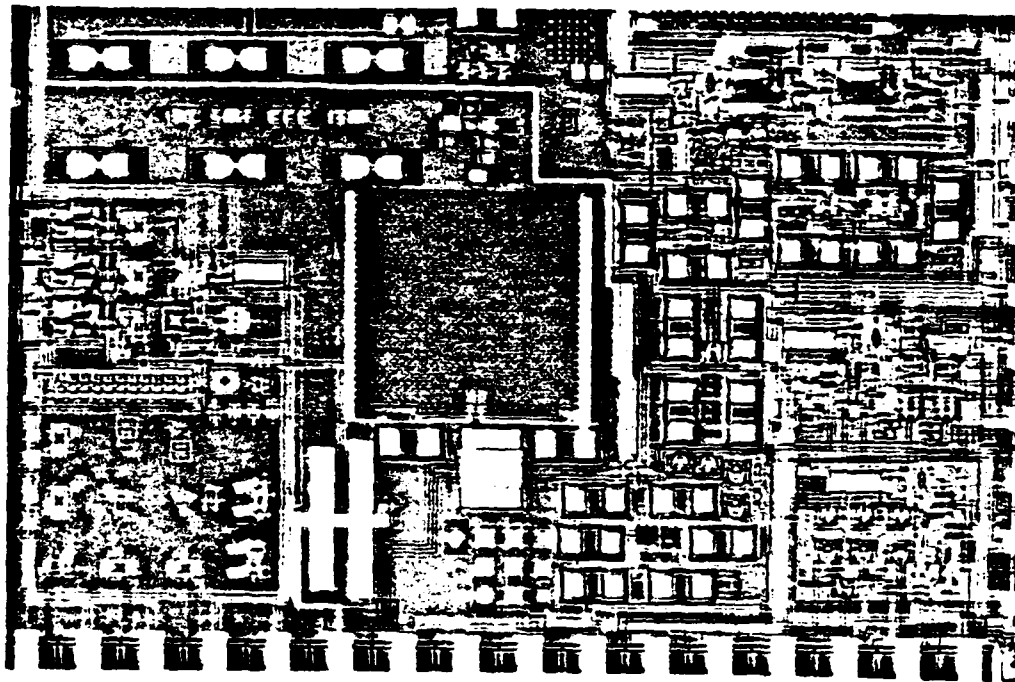


Figure 3-4 Picture of about 2/3 of one of the Josephson chips such as we used in our experiments. Our portion is in the upper right-hand corner. There are no microbridges between the lead pads in this picture.

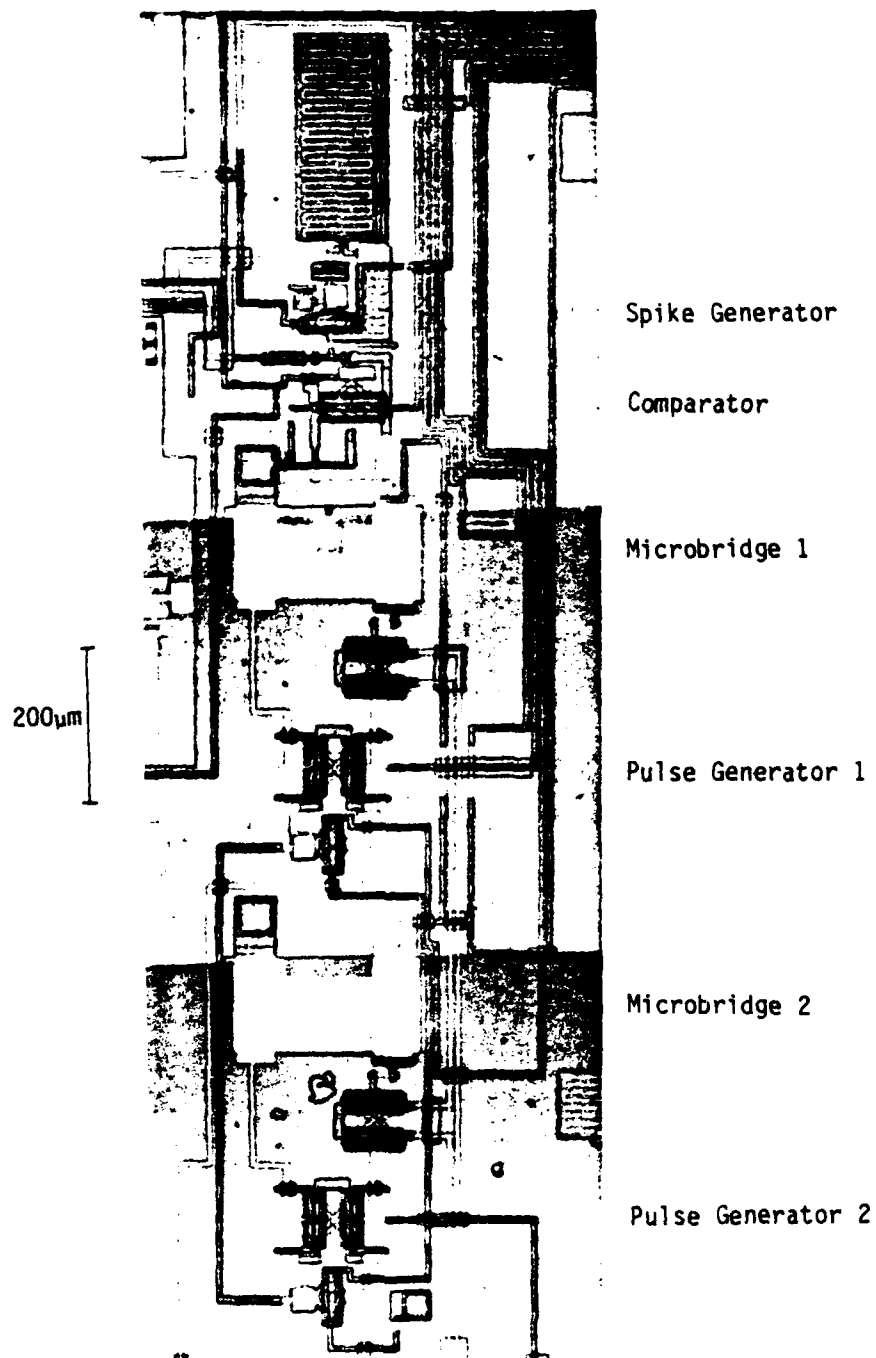


Figure 3-5 Micrograph of our portion of the chip with the various parts of the circuit labeled.

Since the chip was small (only $\sim 1/4" \times 1/4"$) and delicate, it could not be handled directly while fabricating the indium microbridges. This difficulty was overcome by first glueing it to a $1" \times 1"$ piece of a glass microscope slide with Duco cement thinned in acetone. We then did all of the processing: spinning on the photoresist, baking, soaking in chlorobenzene, exposing, developing, evaporating the indium and lifting off the unwanted metal. The final step was to remove the chip from the glass by dissolving the cement in acetone. The microbridge and its pads were fabricated simultaneously with the same evaporation and lift-off. Most of the bridges were $\sim 110\mu\text{m}$ long, although we did test two shorter ones (they are the ones shown in Figure 3-5). The widths varied from $1\text{-}2\mu\text{m}$ and the thickness from $2000\text{-}3000\text{\AA}$. Other characteristics of these microbridges are discussed in Section 5.2.

3.5 Data Taking

All of our measurements were made with the chip immersed directly in liquid helium. The temperature of the liquid helium was controlled by regulating the pressure above it using a Lakeshore Cryogenics pressure regulator. A cryostat with a specially designed chip holder was used to mount the chip. The holder had small etched copper-bronze fingers for making connections to all 64 of the contact pads on the chip. The appropriate fingers for our experiment were then attached to the outside world by means of fourteen 50Ω coaxial cables. (The rest of the 64 chip pads went to other experiments on the chip.) An additional cable was hooked to a resistor heater in indirect contact with the chip. This was used to temporarily heat the chip above its T_c in order to

remove trapped flux whenever such flux would cause the circuitry to malfunction.

The first step in testing any given sample was to carefully evaluate all of the interferometers in the circuit to make sure that they were working properly. Several of our early experiments were frustrated by malfunctioning parts of the circuit. Based on our evaluations of the interferometers, we approximately set the four variable attenuators indicated in Figure 3-3 and the DC power levels for the spike generator and the pulse generator trigger which are indicated in Figure 3-2. We would then fine-tune all of these controls in order to obtain optimum operation of the circuit. The final step was to make the desired voltage waveform measurements.

In taking the waveforms, we would begin at a temperature slightly above T_C and obtain the normal state waveform. Next we would decrease the temperature until it was very slightly below T_C , and then proceed to take a whole series of waveforms at regularly spaced decreasing values of the temperature, until the delay time was too long to observe with the variable length delay lines that we were using. Figure 3-6 shows an example of such a set of data for one of our samples. Note that very close to T_C the delay time is quite short because the critical current of the strip is much less than the fixed pulse height, I_p ($\sim 750\mu A$ in this case). As the temperature is decreased, however, an initial peak (due to the kinetic inductance) becomes evident, after which there is a longer delay time until the voltage begins rising toward the normal state. At still lower temperatures, the critical current of the strip approaches I_p , and the delay time becomes too long to be seen on this

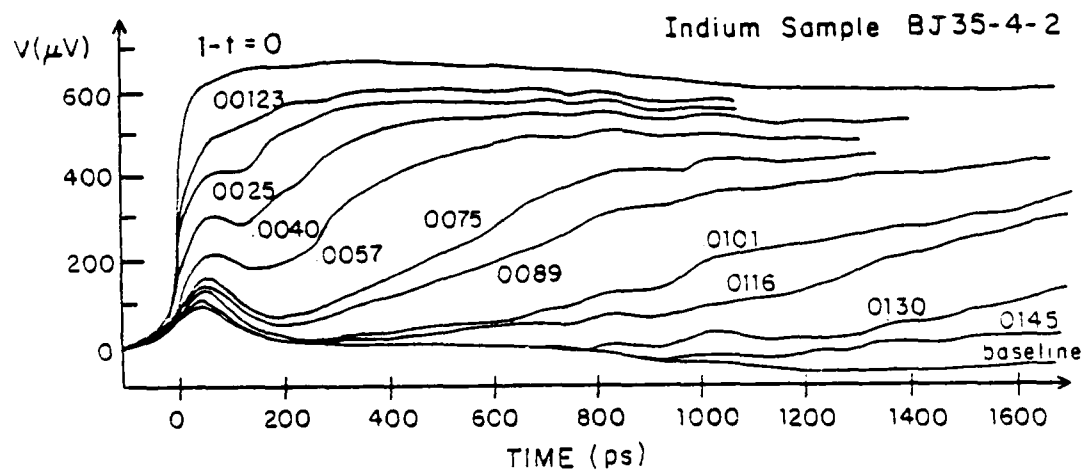


Figure 3-6 Voltage versus time waveforms taken on sample BJ35-4-2 using the IBM superconducting circuitry. These curves are taken with fixed current pulse height by varying the temperature and, hence, the critical current. The curves are parameterized by $(1-t)$, where this t is the reduced temperature, T/T_c .

time scale.

These features will be explained from a theoretical point of view in the next chapter and analyzed quantitatively in the fifth chapter.

CHAPTER IV

THEORY

4.1 Introduction

As reviewed in the first chapter, there have been a variety of contributions to the theoretical understanding of the present experiment. Pals and Wolter (1979) initially used a simple TDGL approach. Tinkham (1979, 1981) showed that a more explicit nonequilibrium approach was more appropriate and yielded the correct time scale. His work was augmented by our own work and that of others (Geier and Schön 1981, Octavio, et al. 1981 and Oppenheim, et al. 1982) using more detailed approximations. We have also added to these theoretical treatments by developing an exact numerical solution to the SST equations (Schmid, Schön and Tinkham 1980), as applied to this experiment.

In this chapter we will begin by discussing, in Section 2, the simple phenomenological theory of Tinkham in order to gain some physical insight into the phenomena that occur in our microbridges. Then, in the third section, we will discuss some of the relatively simple improvements that can be made to his model, including the work of Geier and Schön. Finally, in the last section, we will discuss the results of our numerical solutions of the SST equations.

All of these theoretical approaches involve the assumption that the microbridges can be treated as infinitely long, one-dimensional,

uniform, homogeneous strips, such that the magnitude of the order parameter depends only on time, and not on position along the strip. Although this assumption is clearly an idealization, it is necessary in order to make the theories tractable. Furthermore, it should not be an unreasonable approximation for the weakest part of the strip. The effects of a spatially varying order parameter have been dealt with to some extent by Octavio, et al. and Oppenheim, et al. using the equations of Kramers and Watts-Tobin. We have chosen not to use this approach, however, since it is not accurate for rapid changes in the order parameter, such as can occur during the rising edge of the current pulse in some of our experiments.

An overview of the predictions of the various theories that will be discussed is provided by Figures 4-1(a) and 4-1(b), which show the predicted delay time as a function of I_p/I_c , for dirty aluminum and indium, respectively. For all of these different theoretical curves, the temperature is fixed at 1% below T_c , and the rest of the parameters are chosen to simulate experimentally realistic situations. The current pulse is modelled as rising linearly from zero to I_p in the rise-time t_{rise} , after which it remains constant. The delay time for these plots is defined as beginning at the leading edge of the ramp and ending when $V/V_n=0.5$. (A slightly different definition will be used in Chapter 5 for comparisons with the data, where the current waveforms are not simulated exactly. For these theoretical calculations, however, the current waveforms are exactly the same for all of the curves, and, hence, it seems best to make the comparisons using the relatively simple definition we have suggested above.)

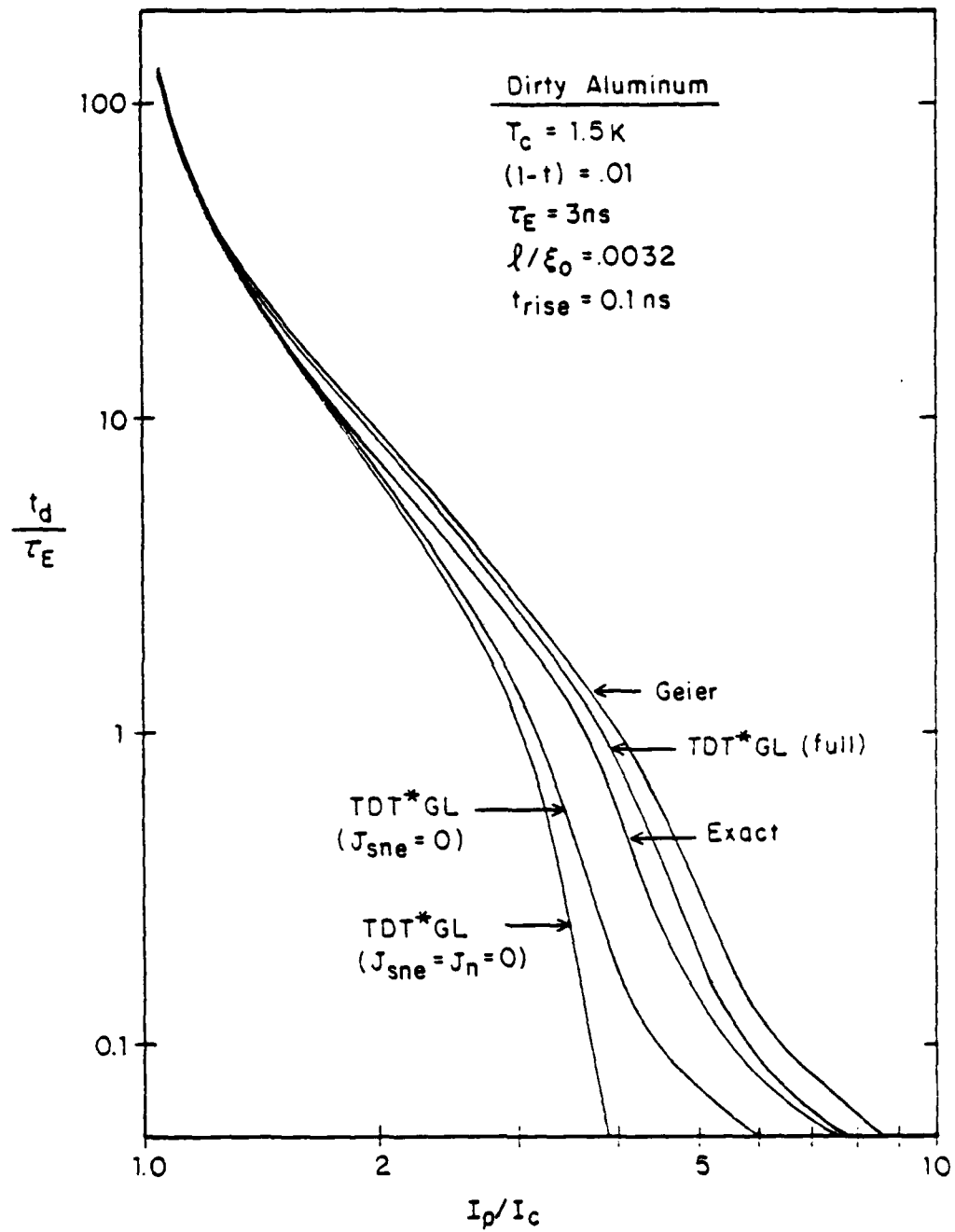


Figure 4-1(a) Delay time as a function of I_p/I_c for dirty aluminum for the five theoretical models considered.

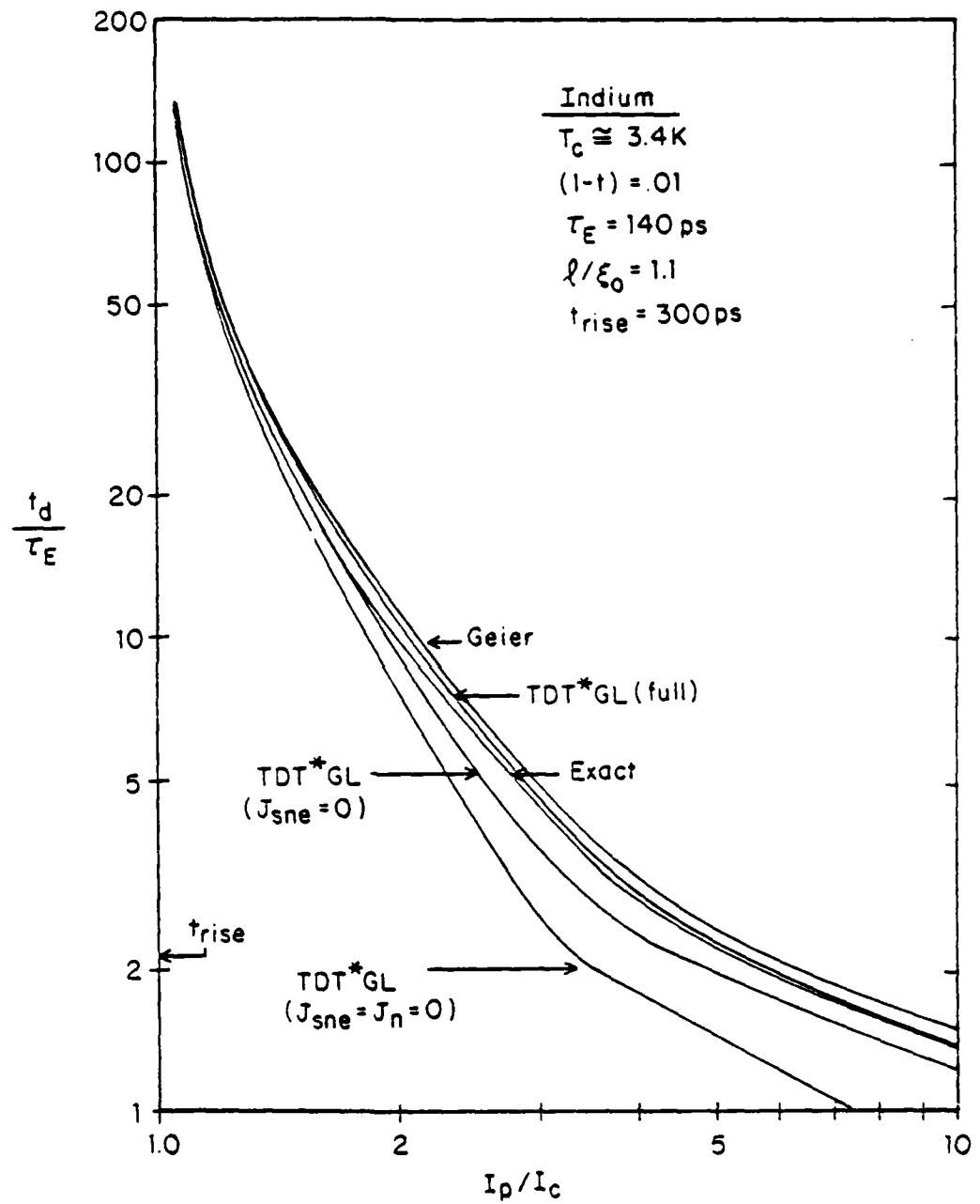


Figure 4-1(b) Delay time as a function of I_p/I_c for indium for the five theoretical models considered.

The parameters for (a), the dirty aluminum, are essentially the same as those of one of the microbridges we tested. The only change is that a shorter rise-time has been used in the calculations than in the experiments. The five curves show the predicted delay time for five different levels of approximation. The curve labeled "exact" represents our numerical solutions of the SST equations. The other four curves are in essence approximations of the SST equations. Hence, the "exact" curve is the one to which they should be compared. Note that they all predict qualitatively the same features: a delay time that diverges as $I_p/I_c \rightarrow 1.0$ and monotonically decreases as I_p/I_c increases. Furthermore, these qualitative features are in good agreement with both our data (see Chapter 5) and that of Pals and Wolter (see Figure 1-2).

Since Tinkham's phenomenological approach to the SST equations is based on putting a time-dependent effective temperature, T^* , into the Ginzburg-Landau equations, its curves are labeled "TDT*GL." The simplest version of Tinkham's theory involves only superfluid current flow; there is no normal current ($J_n=0$) and no nonequilibrium supercurrent ($J_{sne}=0$). As shown in the figure, this simplest approximation falls quite short of the exact delay time for high current ratios. We have been able to substantially improve this approximation by adding one or both of the current terms to the theory. As can be seen, the "TDT*GL(full)" curve, which includes both of the current terms, comes the closest of any of the approximate theories to following the exact solution.

Geier's theoretical work is based directly on the dynamic nonequilibrium superconductivity theory of Schmid and Schön (1975), which is also the origin of the SST equations. His approximations also represent a significant improvement over the simplest TDT*GL. His final equations, however, are only slightly different from those of the full TDT*GL model, and turn out to be slightly less accurate.

The tails of all of these curves, where the delay time begins to decrease more slowly with increasing I_p/I_c , are due to the combined effect of the 100ps rise-time we have used and the 35ps current relaxation time at this temperature. Both of these effects tend to define a shortest time scale within which the order parameter can be driven to zero, even for rather large currents.

The effects of the non-zero rise-time of the pulse are much larger in the curves for indium (Figure 4-1(b)). In these, the rise-time is much longer, relative to τ_E , than in the dirty aluminum curves. As a result, the curves never do reach the regime of rapid decrease with increasing I_p/I_c . Instead, the delay time remains of order t_{rise} , even for relatively large current ratios. Note that in other respects, the qualitative features of the curves and the relationships among them are the same as for aluminum.

In the following section we provide a more detailed discussion of these various models, their relative merits, and some of their predictions.

4.2 Tinkham's Phenomenological Approach

Shortly after Pals and Wolter published their first experiments, Tinkham used a phenomenological approach to nonequilibrium superconductivity to obtain a delay time between the application of a current pulse and the development of the normal state. This delay time was consistent with the results of Pals and Wolter and also consistent with the usual values of the time constants. First we will describe this approach and then discuss its results to provide physical insight into the processes involved in our experiment.

The first step in this approach is to take advantage of the relative magnitudes of the various time constants that determine the time-domain response of a superconductor. In the temperature range of Pals and Wolter's experiment, the current relaxation time, $\tau_J = 2\hbar T / (\pi \Delta_0^2) = 7 \pi (3) \hbar / (4\pi^3 T (1 - \tau))$,* and the Ginzburg-Landau time, $\tau_{GL} = \pi \hbar / (8T(1 - \tau)) = 5.79 \tau_J$, are both very much shorter than τ_E , the inelastic electron-phonon scattering time at the fermi energy at T_C , which determines the relaxation rate of the quasiparticles. One can, therefore, consider a "slow motion" regime consisting of those processes and changes that occur on the time scale of τ_E . In this regime, all processes that occur on the τ_J or τ_{GL} time scales are treated as instantaneous, and relaxation of the nonequilibrium quasiparticle distribution is the primary dynamic process.

* we are using units in which $k_B = 1$, i.e., T has units of energy.

The second step is to make the rather sweeping approximation that the state of the nonequilibrium quasiparticle distribution can be adequately described by a single parameter, $T^* = T + \delta T^*$. This parameter plays the role of an effective temperature, but it does not necessarily correspond to any physically observable temperature. This characterization will not always be valid, but for many purposes, it turns out to be a good approximation. The G-L equation and associated current equation then take the form

$$0 = (\alpha^* + \beta \frac{\Delta^2}{T^2} + \xi^2(0)Q^2)\Delta \quad (4-1a)$$

$$J = \frac{3\sqrt{3}}{2} \left(\frac{\Delta}{\Delta_0}\right)^2 \xi(T)Q \quad (4-1b)$$

where $\alpha^* = (T^*/T_c - 1) = T/T_c - 1 + \delta T^*/T_c = \alpha + \delta \alpha^*$ is the normalized effective temperature, $\beta = 7\pi^2/(8\pi^2) = 0.106$, Δ is the energy gap or order parameter, $\xi(T) = \xi(0)(1 - T/T_c)^{-1/2}$ is the G-L coherence length, Q is the superfluid momentum, and $J = I/I_c$ is the normalized current. In determining these equations, we have assumed, as mentioned before, a one-dimensional uniform strip with no spatial gradients.

In these conventions, which will be used throughout, the equilibrium gap, Δ_0 , is given by $\Delta_0^2/T_c^2 = -\alpha/\beta$. Changing to the usual reduced variables, $\psi = \Delta/\Delta_0$ and $q = \xi(T)Q$, simplifies Eq. (4-1) to the form

$$1 - \psi^2 - q^2 = -\delta \alpha^* / \alpha \quad (4-2a)$$

$$J = \frac{3\sqrt{3}}{2} \psi^2 q \quad (4-2b)$$

The next step is to determine $\delta\alpha^*$ in terms of the nonequilibrium quasiparticle distribution. This is accomplished by defining T^* such that the equilibrium gap at T^* , $\Delta_0(T^*)$, is equal to the actual instantaneous value of the gap in the presence of the nonequilibrium quasiparticle population. This definition is evaluated by means of the self-consistent gap equation in the absence of all spatial gradients:

$$\frac{2}{V} = \sum_k \frac{1-2f_k}{E_k(\Delta)} = \sum_k \frac{1-2f_k}{\sqrt{\Delta^2 + \epsilon_k^2}} \quad (4-3)$$

where f_k is the instantaneous quasiparticle population. The nonequilibrium part of this population is $\delta f_k = f_k - f_0(E_k(\Delta)/T)$, where f_0 is the usual fermi function. Solving for T^* , and, hence, for $\delta\alpha^*$, one can show that the following relations are approximately true near T_c and for small δf :

$$\delta\alpha^* = \frac{1}{N(0)} \sum_k \frac{\delta f_k}{E_k} = \int_{-\infty}^{\infty} \frac{\delta f}{E} d \quad (4-4)$$

where $N(0)$ is the density of states at the fermi energy.

The final step is to determine the nonequilibrium quasiparticle distribution, δf_k , in this slow motion regime. In general, the δf_k 's are given by a Boltzman equation, where the source of the nonequilibrium is the gap variation. In the relaxation approximation, the solution to such an equation is

$$\delta f_k = \int_{-\infty}^t \left(- \frac{\partial f_0(t')}{\partial t'} \right) e^{(t'-t)/\tau_E} dt' \quad (4-5)$$

where $\frac{\partial f_0}{\partial t}(t') = \frac{-1}{4T} \frac{\Delta'}{E_k} \Delta'$ and a ' means that the variable is a function of t' rather than of t . Combining these results with Eq. (4-4) gives

$$\dot{\alpha}^* \approx \frac{1}{4T} \int \int \frac{\Delta'}{EE'} \dot{\Delta}' e^{(t'-t)/\tau_E} dt' d\epsilon \quad (4-6)$$

$$\approx \frac{\pi}{4T} \int_{-\infty}^t \dot{\Delta}' e^{(t'-t)/\tau_E} dt' \quad (4-7)$$

where the second equation is the result of a fairly accurate approximate evaluation of the energy integral for $\Delta \approx \Delta'$.

Now that the effective nonequilibrium temperature has been found in terms of Δ , (4-2) can be written in closed form as

$$1 - \psi^2 - q^2 = \frac{2\tau_\Delta}{\tau_E} \int_{-\infty}^t \dot{\psi}' e^{(t'-t)/\tau_E} dt' \quad (4-8a)$$

$$J = \frac{3\sqrt{3}}{2} \psi^2 q \quad (4-8b)$$

where τ_Δ is the (longitudinal) gap relaxation time, which is given by $2\tau_\Delta/\tau_E = \pi/(4\sqrt{8(1-\epsilon)}) = 2.41(1-\epsilon)^{-1/2}$. These two equations represent the simplest form of the TDT*GL theory (*i.e.*, with $J_n = J_{sne} = 0$), the results of which were shown in Figure 4-1.

When we apply this model to our experiment, we take $J=0$ for $t < 0$, $J = J_p t/t_{\text{rise}}$ for $0 < t < t_{\text{rise}}$ and $J = J_p$ for $t > t_{\text{rise}}$, where $J_p = I_p/I_c$ is the height of the pulse relative to the critical current. Using this definition of J , we can numerically solve these equations for the gap and the voltage (which is proportional to \dot{q}) as a function of time. (It may, in principle, be possible to solve these equations analytically, but it does not appear that it would be worth the effort or that it would provide any additional insight.) An example of the solution of these equations is shown in Figure 4-2(a), where the voltage has been normalized to its normal state value, which is given by $\dot{q}_n = (1/\tau_J)(2/3\sqrt{3})J_p$. Notice that there are three distinct time regimes

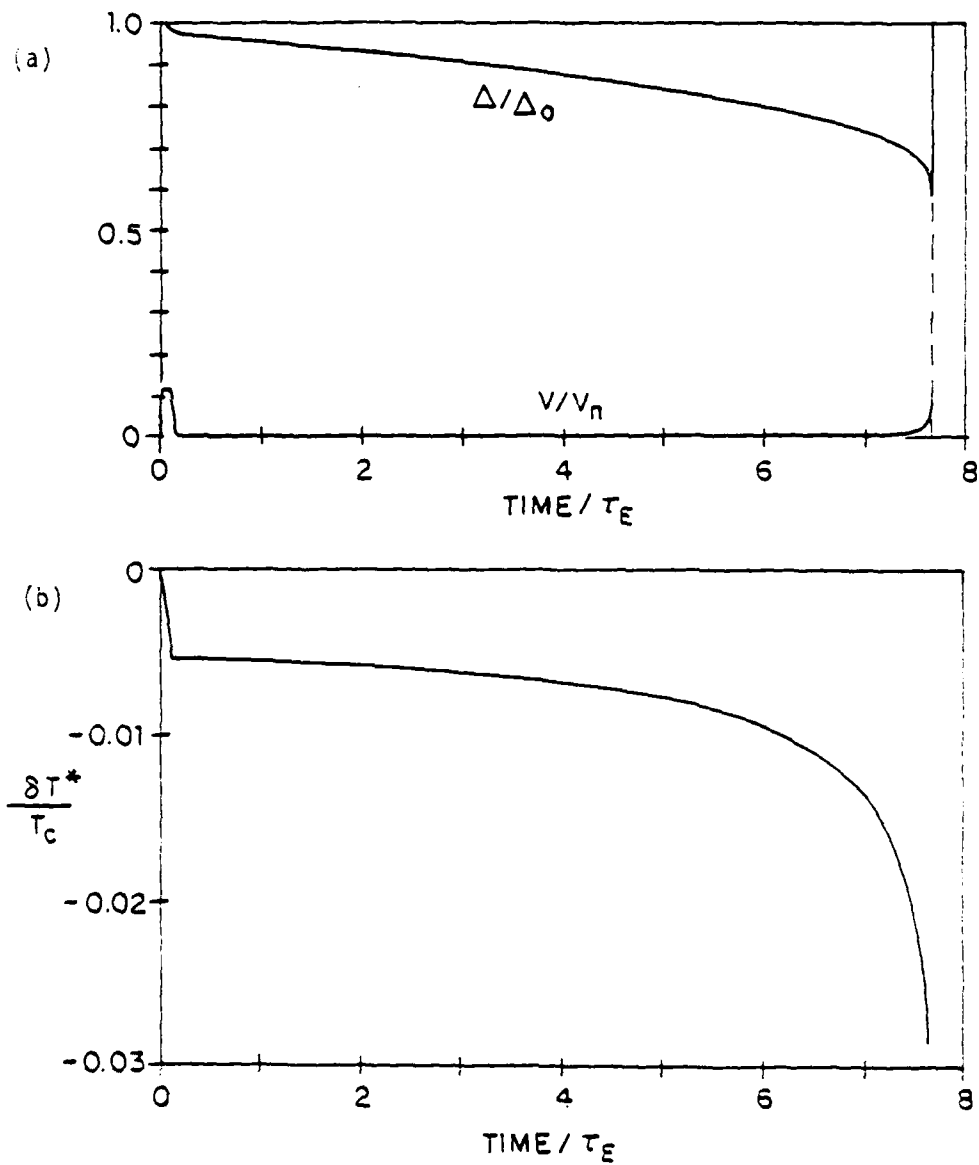


Figure 4-2 An example of the solution of the simplest form of the TDT*GL model for $(1-T/T_c)=0.01$, $I_0/I_c=1.8$ and $t_{\text{rise}}/\tau_E=0.15$. (a) shows the gap and voltage development and (b) shows the corresponding δT^* development.

in these solutions. For $t \ll \tau_E$, the gap and voltage vary rapidly, to accommodate the current step. These processes all relax away by the time $t \approx \tau_E$, provided that $\tau_{\text{rise}} \ll \tau_E$. There then follows a much longer delay time during which the gap and voltage vary relatively slowly. Finally, at the end of the delay time, the gap rapidly decreases to zero and the voltage diverges, indicating that the superconductivity has been entirely destroyed. Insight into these three regimes can be gained by analyzing them in light of the equations.

In the first regime, where $t \ll \tau_E$, Eq. (4-8a) can be well approximated by

$$1 - \psi^2 - \frac{4}{27} J^2(t)/\psi^4 = \frac{2\tau_\Delta}{\tau_E} (\psi - \psi(-\infty)) \quad (4-9)$$

where $\psi(-\infty) = 1.0$, since there were no DC bias currents, and where we have substituted for q from Eq. (4-8b). Thus, on this time scale, as $J(t)$ increases, $\psi(t)$ decreases in compensation. Phenomenologically this compensation takes two forms. On the left hand side of (4-9), the decreasing ψ^2 is the usual G-L adjustment for currents, and on the right hand side the decreasing ψ corresponds to a negative δT^* , in effect a cooling of the superconductor that enables it to carry a larger current. This nonequilibrium effective temperature decrease is shown in Figure 4-2(b) for the same case as in 4-2(a). As can be seen, the δT^* and the gap decrease rapidly during the rising edge of the current pulse, so that by the time the current reaches J_p , the effective temperature and the gap are low enough that J_p can be carried. Since this new, decreased value of ψ is the upper value of ψ during the next, τ_E dominated, regime, it will be called ψ_{max} . Algebraically,

the value of ψ_{\max} is given by

$$\frac{4}{27} J_p^2 = \psi_{\max}^4 (a + 1 + \psi_{\max})(1 - \psi_{\max}) \quad (4-10)$$

where $a = 2 \tau_{\Delta} / \tau_E$.

An example of a ψ_{\max} versus J_p curve is included in Figure 4-3 for $(1 - \epsilon) = 0.01$. Notice that there is a max value of J_p , beyond which there does not exist a real solution for ψ_{\max} . This means that for this model, when J_p exceeds this maximum value, which we have called J_{c1} , there is no second regime. The gap simply decreases very rapidly all the way to zero in a time that depends mostly on the rise-time and magnitude of the current step. Figure 4-1 shows that this effect is qualitatively seen in the numerical calculations for this model. Approximately solving (4-10) for J_{c1} gives

$$J_{c1} \cong 1.15 (1 - \epsilon)^{-1/4} \quad (4-11)$$

which is approximately 3.5 at $(1 - \epsilon) = 0.01$.

The initial voltage spike in this regime can be understood by using a very simple model. Since $V \propto \dot{q}$ and $q \propto J / \psi^2$, we clearly have $V \propto \dot{q} \propto \dot{J} / \psi^2$, ignoring, for the moment, $\dot{\psi}$. Note that since $V \propto \dot{J} / \psi^2$, and $V = \dot{I}L$ for an inductor, $1/\psi^2$ plays the role of an inductance. This is known as the kinetic inductance of the superfluid, L_K . (This concept can be generalized to include gap variation by letting $V = \dot{J}L_K + J\dot{L}_K$, where \dot{L}_K includes the $\dot{\psi}$ terms.) As can be seen from the figure, the voltage response of this theory is indeed that of a linearly ramped current applied to an inductor. Henceforth, we shall call this response a "kinetic-inductance spike."

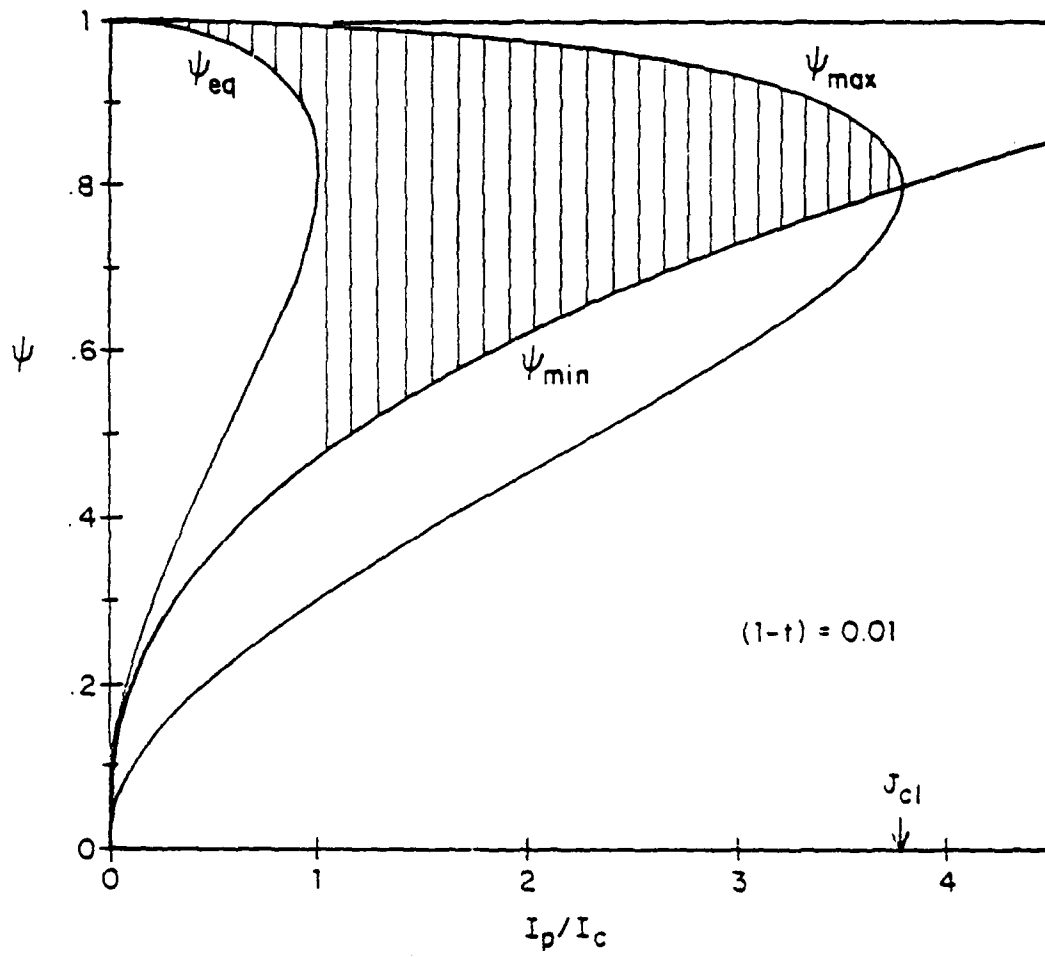


Figure 4-3 An illustration of the various regime boundaries in the simplest TDT GL model.

In the second regime, where $\tau_E \leq t < t_d$, the current is constant and there are no fast changes. Hence, (4-8b) can be substituted into (4-8a) and then that can be solved for $\dot{\psi}$. The result is

$$\dot{\psi} = \frac{1}{2\tau_\Delta} \frac{1 - \psi^2 - \frac{4}{27} J_p^2 / \psi^4}{1 + (1/a)(2\psi - \frac{16}{27} J_p^2 / \psi^5)} \quad (4-12)$$

This equation determines the time dependence of the gap throughout the second regime. The gap begins at ψ_{\max} in this regime and decreases, since the numerator is negative. If $J_p \leq 1$, there is an equilibrium solution of the G-L equation such that

$$1 - \psi_{\text{eq}}^2 - \frac{4}{27} J_p^2 / \psi_{\text{eq}}^4 = 0 \quad (4-13)$$

in which case the gap relaxes to that equilibrium value and remains there, since the numerator of (4-12) is then zero.

If J_p is slightly larger than 1., then the numerator of (4-12) can never actually reach zero, but it does become quite small as ψ passes by $\sqrt{2/3}$, the value at which it comes closest to carrying the entire current as supercurrent. As a result, $\dot{\psi}$ can become arbitrarily small as J_p approaches unity from above. This causes the divergence in the delay time as $J_p \rightarrow 1$. Making an approximate solution for the delay time in this divergence region, one can show that

$$t_d \approx \pi\sqrt{2} \tau_\Delta \left(\frac{1}{\sqrt{J_p^2 - 1}} - 0.50 \right) \quad (4-14)$$

is the asymptotic form.

Phenomenologically, this regime can be thought of as being determined by the need for a small, but continuing, decrease in ψ , which generates the δT^* necessary to allow the current flow. Since $V \propto \dot{q} \propto -J \dot{\psi} / \psi^3$ in this regime, this continuing decrease in ψ gives rise to a small non-zero voltage throughout the delay time. Although the example in Figure 4-2 has too low a J_p to observe this effect it can be seen when higher currents are used (see, for example, Figure 4-4).

As ψ decreases, the denominator of (4-12) also decreases, until it reaches zero when $\psi = \psi_{\min}$, where ψ_{\min} is given by $J_p^2 = (27/16) \psi_{\min}^5 (a + 2 \psi_{\min})$. An example of ψ_{\min} versus J_p is shown in Figure 4-3. One further point is that as ψ approaches ψ_{\min} , $\dot{\psi}$ goes to negative infinity and, hence, \dot{q} diverges to positive infinity.

This divergence in $\dot{\psi}$ and \dot{q} (or V) can be seen in Figure 4-2(a). It signals the end of the second regime. In the third regime ψ drops the rest of the way from ψ_{\min} to zero. This would be expected to occur on the time scale of τ_{GL} , which has been assumed infinitesimal in this model. Hence, the drop is indicated in Figure 4-2(a) as a dashed line. It will be shown in the next section that the inclusion of the normal current in the calculations removes this non-physical divergence.

As a summary, these three regimes are illustrated graphically in Figure 4-3 for $(1-t)=0.01$. Before the pulse starts, $\psi=1$, and $J=0$, which is the top left-hand point on the graph. During the first regime, when the current rises to J_p and the initial δT^* develops so that the current can be carried, the order parameter descends from $\psi=1$ to $\psi = \psi_{\max}(J_p)$. Note that if $J_p > J_{c1}$, ψ_{\max} does not exist, and the order

parameter falls rapidly all the way to zero. During the second regime, ψ falls from $\psi_{\max}(J_p)$ to $\psi_{\min}(J_p)$ at a rate governed by the quasiparticle relaxation time. Note that if $J_p < 1$, ψ falls only to ψ_{eq} , which is a stable solution, and remains there. For $J_p > 1$, the rate at which ψ is decreasing diverges at $\psi = \psi_{\min}(J_p)$, and during the third regime ψ falls very rapidly from $\psi_{\min}(J_p)$ to zero. This signals the final destruction of the superconducting state, the development of the normal state voltage and, hence, the end of the delay time.

This analysis of Figure 4-3 shows that the delay time within this model, in which effects on the scale of τ_J and τ_{GL} are neglected, is given by the following integral:

$$t_d(J_p) = \int_{\psi_{\max}(J_p)}^{\psi_{\min}(J_p)} \frac{d\psi}{\dot{\psi}(\psi, J_p)} \quad (4-15)$$

where the expression for $\dot{\psi}$ is given by (4-12). Although this model is not as accurate as the exact theory, it is much more readily evaluated numerically to provide qualitative estimates of the delay time. An approximate evaluation of this integral for J_p very close to 1. gives the asymptotic limit in (4-14). It can also be approximately evaluated in the limit where $2 \leq J_p \ll J_{c1}$, in which case the result is $t_d \approx 2.7 \tau_A / (J_p^2 - 1)$. Unfortunately, this condition on J_p cannot truly be satisfied except extremely close to T_c .

4.3 Simple Improvements

In this section we discuss some of the simple improvements that can be made to Tinkham's simple phenomenological approach. The most

physically obvious of these improvements is to include the normal current in the current equation (4-2b). We have done this by using the usual definition for the normal current

$$J_n = \frac{3\sqrt{3}}{2} \tau_J \dot{q} \quad (4-16)$$

where $J_n = I_n/I_c$. (This definition of the normal current uses the gauge choice $\vec{Q} = -2e\vec{A}$, where \vec{A} is the vector potential, which results in the voltage being proportional to \dot{Q} .) Thus, the current equation becomes

$$J = \frac{3\sqrt{3}}{2} (\psi^2 \dot{q} + \tau_J \dot{q}) \quad (4-17)$$

where Eq. (4-8a) still governs the time-dependence of the gap.

We have solved this coupled set of differential equations numerically and the resulting delay times as a function of J_p for two particular cases are included in Figures 4-1(a) and 4-1(b), where they are labeled as "TDT*GL($J_{sne}=0$).". Note that the results of the model with only this simple improvement are much closer to the exact results than the original version of the model.

Figure 4-4 shows a comparison of the time evolution of the gap and the voltage for all five models we consider. Note the similarities and differences between the present model and the original model. (The squarish voltage pulse is the one associated with the original model.) During the rising edge of the pulse the behavior is quite different, although the gap ends up at nearly the same value in both cases. After the rise-time, the two models predict nearly the same rates of gap decrease until near the end, where we find that the non-physical discontinuous drop of the gap in the initial model has been replaced by

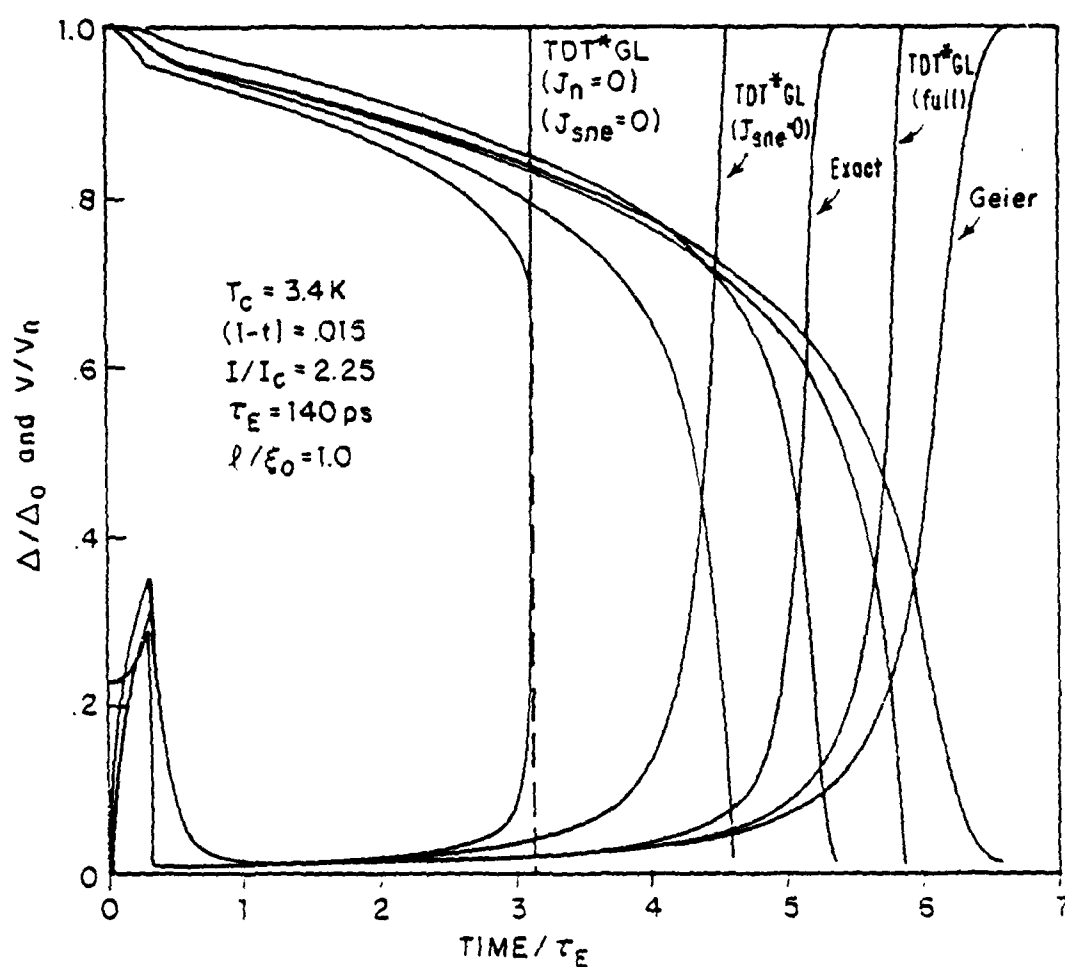


Figure 4-4 A comparison of the time evolution of the gap and the voltage for the five theoretical models considered. The squarish initial spike is the one associated with the TDT*GL ($J_n=J_{sne}=0$) model.

a longer, smooth transition to zero gap.

As mentioned before, the kinetic-inductance spike of the initial model is simply that of an inductor. The voltage response of the second model, which includes J_n , is essentially that of a linearly ramped current applied to a resistor and inductor in parallel. Thus, by adding J_n , we have in effect added the normal state resistance, R_n , in parallel with L_K . From simple circuit theory, we can calculate the expected height of this kinetic-inductance spike; it is

$$V_{\text{spike}} \approx \frac{\tau_J}{t_{\text{rise}}} (1 - e^{-t_{\text{rise}}/\tau_J}) V_n \quad (4-18)$$

where we have assumed a constant $L_K = L_K(t=0)$.

The other important difference between the original model and this first improved version is that the non-physical discontinuous drop of the gap from ψ_{min} to zero that occurs in the original model has been removed. From a physical point of view, this is because when the order parameter begins to decrease more rapidly, and V begins increasing, the voltage causes the current to be shunted more and more through R_n . This means that ψ does not need to decrease as rapidly as in the first model to enable the current to be carried. This process continues throughout the transition to the normal state, thus significantly lengthening the delay time to a value that is much closer to the exact calculation.

The second improvement that we have made in Tinkham's simple model is to include the J_{Sne} term in the current equation. The importance of this term in connection with this problem was first pointed out by Geier and Schön. It comes from the full SST equations, but for

phenomenological purposes it can also be derived from the τ^* approach (see Tinkham 1981, p. 258). In our usual reduced variables, it takes the form

$$J_{sne} = -\frac{3\sqrt{3}}{2} \psi q \int_{-\infty}^t \dot{\psi}' e^{(t'-t)/\tau_E} dt' \quad (4-19)$$

This is the same integral as occurred in the expression for $\delta\alpha^*$ [Eq. (4-7)]. Hence, the calculations do not become significantly more difficult.

Adding this term to (4-17), we obtain

$$1 - \psi^2 - q^2 = \frac{2\tau_\Delta}{\tau_E} \int_{-\infty}^t \dot{\psi}' e^{(t'-t)/\tau_E} dt' \quad (4-20a)$$

$$J = \frac{3\sqrt{3}}{2} (\psi^2 q + \tau_J \dot{q} - \psi q \int_{-\infty}^t \dot{\psi}' e^{(t'-t)/\tau_E} dt') \quad (4-20b)$$

for the gap and current equations of this full TDT^{*}GL model. [Eq. (4-8a) has been repeated for convenience.] The delay time as a function of J_p for this theory was shown in Figure 4-1, where it can be seen that it comes the closest to following the exact calculations.

Comparing the gap and voltage development for this model with the previous version ($J_{sne}=0$) in Figure 4-4, it appears that the effect of this J_{sne} term is to decrease the magnitude of the initial drop in the gap and to slow down the gap's rate of decrease throughout. This is consistent with the idea that J_{sne} carries part of the current, and, hence, the necessary drop and rate of decrease to carry the same total current is lower. Comparison with the exact calculations, however, makes it appear that the near agreement of this model in overall delay time may be partially fortuitous. The order parameter in the exact

calculations starts the slow regime much higher than in the approximate models and declines more slowly, until it begins a faster decrease to zero from a higher level. Some of the reasons for these discrepancies will be discussed in the next section on our exact calculations.

The last approximate theory we have evaluated is that of Geier and Schön (1981). As mentioned before, it was derived directly from the equations of Schmid and Schön (1975). Their final equations, however, are the same as Eqs. (4-20), except that the integral in (4-20a) has been changed so that the equation becomes

$$1 - \psi^2 - q^2 = \frac{2\tau_\Delta}{\tau_E} \frac{1}{\sqrt{\psi}} \int_{-\infty}^t \dot{\psi}' \sqrt{\psi'} e^{(t'-t)/\tau_E} dt' \quad (4-21)$$

This form of the integral should be a slightly more accurate evaluation of the energy integral in (4-6) when the pair breaking potential is much less than the gap. As can be seen from Figure 4-4, however, this integral leads to an even slower final decrease in the order parameter than the form used by Tinkham, and hence to longer delay times, as seen in Figure 4-1.

4.4 Numerical Solution of SST Equations

In a sense, all of the foregoing theories have been approximations to the SST equations, as applied to this problem. They serve to provide physical insight into the processes involved in this experiment, but to obtain truly accurate predictions from theory, it is necessary to use the full theory, not just approximations.

In using the SST equations to analyze this problem, the only approximation we have made is that mentioned in the first section, namely that we will be considering a one-dimensional, uniform filament, with no variations in the magnitude of the order parameter along its length. This approximation, combined with a gauge choice of $\vec{Q} = -2e\vec{A}$ and $\nabla\varphi=0$, where φ is the phase of the order parameter, allows us to drop all terms from the equations that involve spatial gradients. A further consequence is that we can entirely remove the two of the initial five equations that relate to branch imbalance.

The remaining three equations consist of a Boltzmann equation for the quasiparticle distribution function, $f(E)$, a G-L equation, and a current equation. Using our usual reduced variables, they are

$$N_1 \dot{\delta f} + \frac{N_1}{\tau_E} \delta f + R_2 \dot{\psi} \frac{\partial f}{\partial \varepsilon} - D' N_2 R_2 q \dot{q} \frac{\partial f}{\partial \varepsilon} = 0 \quad (4-22a)$$

$$(1 - \psi^2 - q^2) \dot{\psi} = \tau_{GL} \dot{\psi} + \frac{1}{1-t} \int_{-\infty}^{\infty} R_2 \delta f d\varepsilon \quad (4-22b)$$

$$\frac{2}{3\sqrt{3}} J = \psi^2 q - \tau_J \dot{q} \int_{-\infty}^{\infty} M \frac{\partial f}{\partial \varepsilon} d\varepsilon - 4 \frac{\Delta_0 \tau_J}{\hbar} q \int_{-\infty}^{\infty} N_2 R_2 \delta f d\varepsilon \quad (4-22c)$$

where N_1 , N_2 , R_2 and M are generalized densities of states, and $\delta f = f - f_0$ is the nonequilibrium distribution function. The reduced variable, ε , is equal to E/Δ_0 , and $D' = D\hbar/(\xi^2(T)\Delta_0)$ is a renormalized diffusion constant. Since the SST equations are derived for dirty superconductors near T_c , these equations can only be expected to be accurate for $\ell/\xi_0 \ll 5.5$ and $(1-t) \ll 1$.

The generalized densities of states are given by the following relations:

$$N_1 + iR_1 = \frac{\varepsilon/\psi + i\gamma/\psi}{\sqrt{(\varepsilon/\psi + i\gamma/\psi)^2 - 1}} \quad (4-23a)$$

$$N_2 + iR_2 = \frac{i}{\sqrt{(\varepsilon/\psi + i\gamma/\psi)^2 - 1}} \quad (4-23b)$$

$$M = N_1^2 + R_2^2 \quad (4-23c)$$

where $\gamma = \Gamma/\Delta_0$ is the reduced pair breaking potential. (We have used this M because it is slightly more accurate than the M^T that appears in the SST equations; see Schmid (1981), p.446.) Figure 4-5 shows an example of each of these densities of states for $\Gamma/\Delta=0.01$. In the limit where Γ/Δ goes to zero, N_1 becomes the usual BCS density of states.

Appendix B discusses and provides a listing of the computer program we have written to solve these equations. The validity of the numerical solution has been carefully checked by varying the number of energy bins used for $\delta f(E)$ and by varying the fineness of the time steps. These tests result in less than a 1% variation in the total delay time, thus indicating a well-converged solution.

Using this program, we can obtain an accurate picture of the evolution of the quasiparticle population during the delay time. Figure 4-6(a) shows an example of δf , the nonequilibrium quasiparticle distribution function, as a function of energy and time for an indium microbridge at $(1-t)=0.015$. The rising edge of I_p begins at $t=0$ and δf is initially equal to zero. As can be seen from the figure, the current pulse causes a negative going peak to develop in δf , thus, indicating that there are fewer quasiparticles at these energies than thermal equilibrium would dictate. Hence, Tinkham's δT^* is negative,

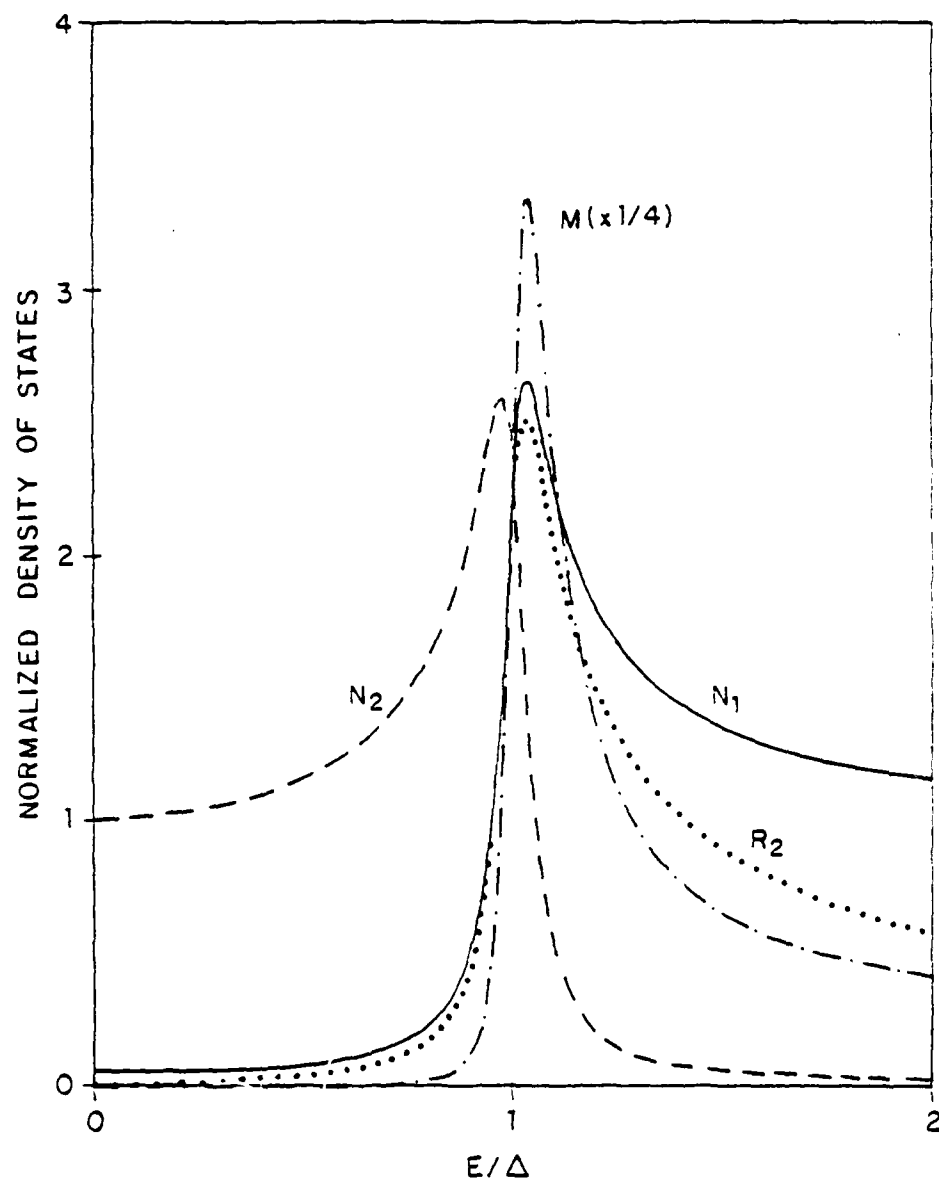


Figure 4-5 Examples of the four generalized densities of states used in the SST equations. Note that M has been reduced by a factor of 4 so that it will fit on this scale.



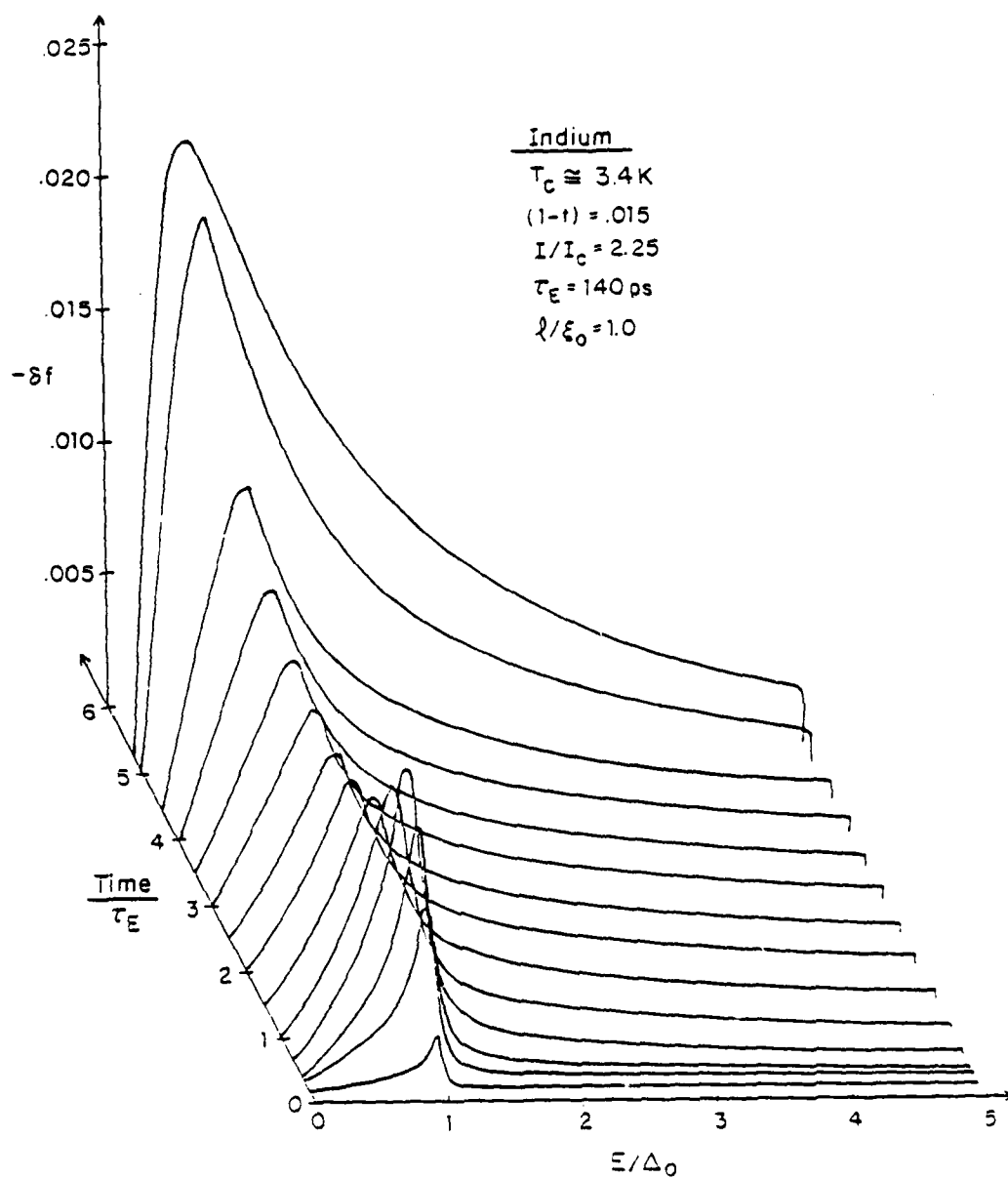


Figure 4-6(a) Plot of the nonequilibrium quasiparticle distribution function as a function of time and energy. Note that δf is negative.

AD-A130 913

TRANSIENT RESPONSE OF SUPERCONDUCTING MICROBRIDGES TO
SUPERCritical CURRENTS(U) HARVARD UNIV CAMBRIDGE MA DIV
OF APPLIED SCIENCES D J FRANK JUN 83 TR-20
N00014-77-C-0085

2/2

UNCLASSIFIED

F/G 20/3

NL

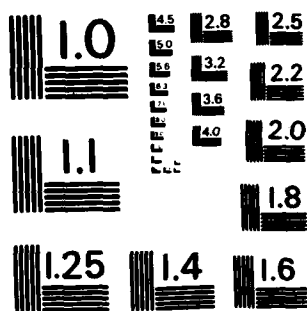
END

DATE

FILED

6 83

DTIC



MICROCOPY RESOLUTION TEST CHART
NATIONAL BUREAU OF STANDARDS-1963-A

as expected. Note that near the end of the delay time the nonequilibrium distribution function becomes significantly larger.

Figure 4-6(b) shows the total quasiparticle density, $n_{qp} = N_1(\delta f + f_0)$, as a function of energy and time for the same case. At $t=0$, Γ is much less than Δ , there is very little gap broadening and n_{qp} is almost exactly the BCS result. After the current step, however, the gap broadening becomes much more significant. In fact, near the end of the delay time, the gap broadening becomes so large that it causes n_{qp} to look very much like the normal state result.

This broadening is due to the pair breaking potential, $\Gamma = \Gamma_0 + (D/2)Q^2$, which becomes quite large near the end of the delay time because Q becomes large there. Figures 4-7(a) and (b) show an example of Γ/Δ , along with the gap, the voltage, and J_{sne} as they develop in time, for indium and dirty aluminum, respectively. The features of these curves are typical of all of the curves we have studied. Note that Γ/Δ is plotted against the log scale on the right and reaches final values around 100 for both figures. (This normalization of Γ is plotted because it is equal to γ/ω , which is the form that enters the generalized densities of states [Eqs. (4-23)].)

We believe that this high value of Γ/Δ is the primary cause of most of the differences between this exact theory and the previous theories, all of which assume $\Gamma/\Delta \ll 1$. Figure 4-8 shows plots of the important densities of states for varying values of Γ/Δ . Clearly, the form of these densities changes drastically between $\Gamma/\Delta = 0.1$ and $\Gamma/\Delta = 1.0$, necessitating entirely different approximations of the

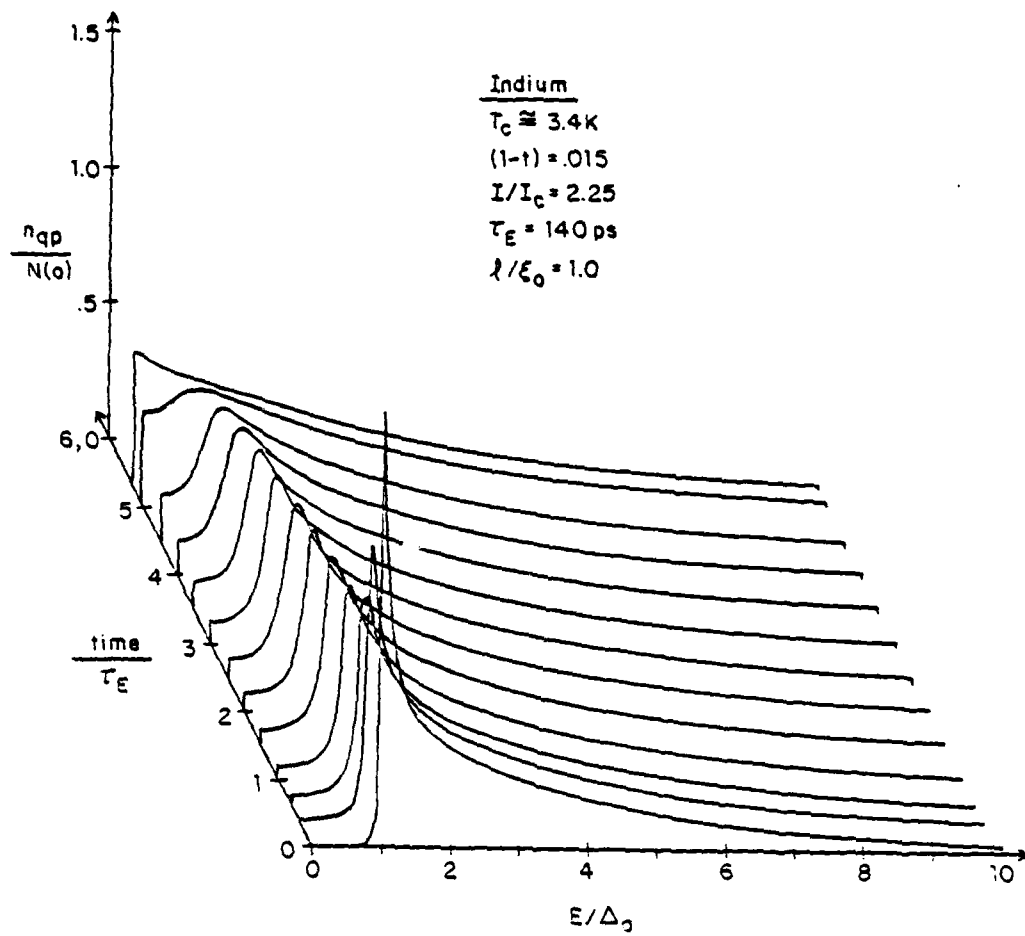


Figure 4-6(b) Plot of the total quasiparticle density as a function of time and energy.

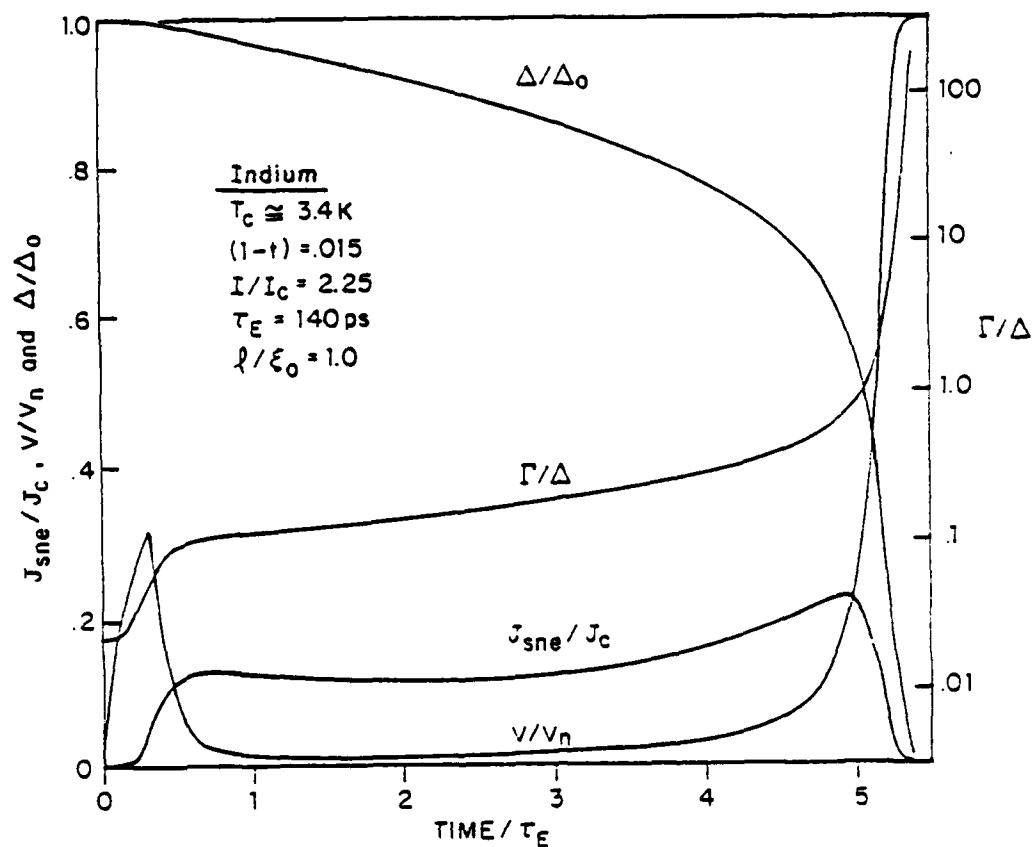


Figure 4-7(a) Plot showing the evolution of Δ , J_{sne} , V and the pair-breaking potential for indium as determined from our exact numerical solution of the SST equations.

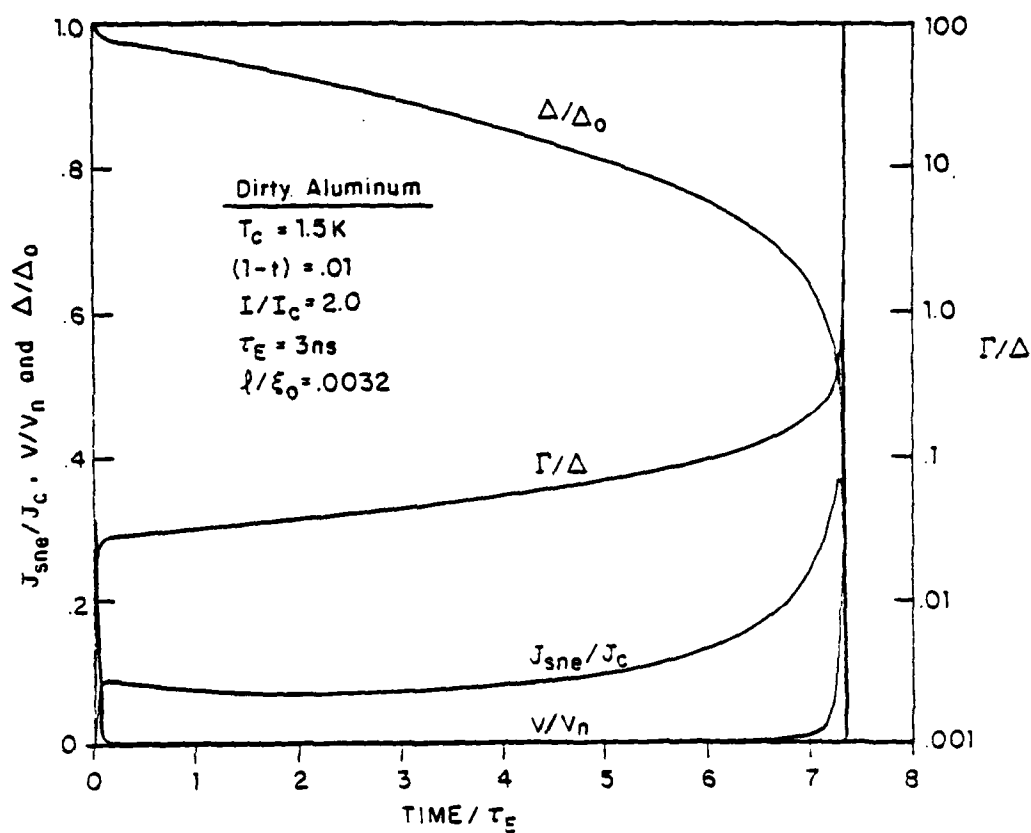


Figure 4-7(b) Plot showing the time dependence of Δ , J_{sne} , V and the pair-breaking potential for dirty aluminum as calculated by our exact numerical solution of the SST equations.

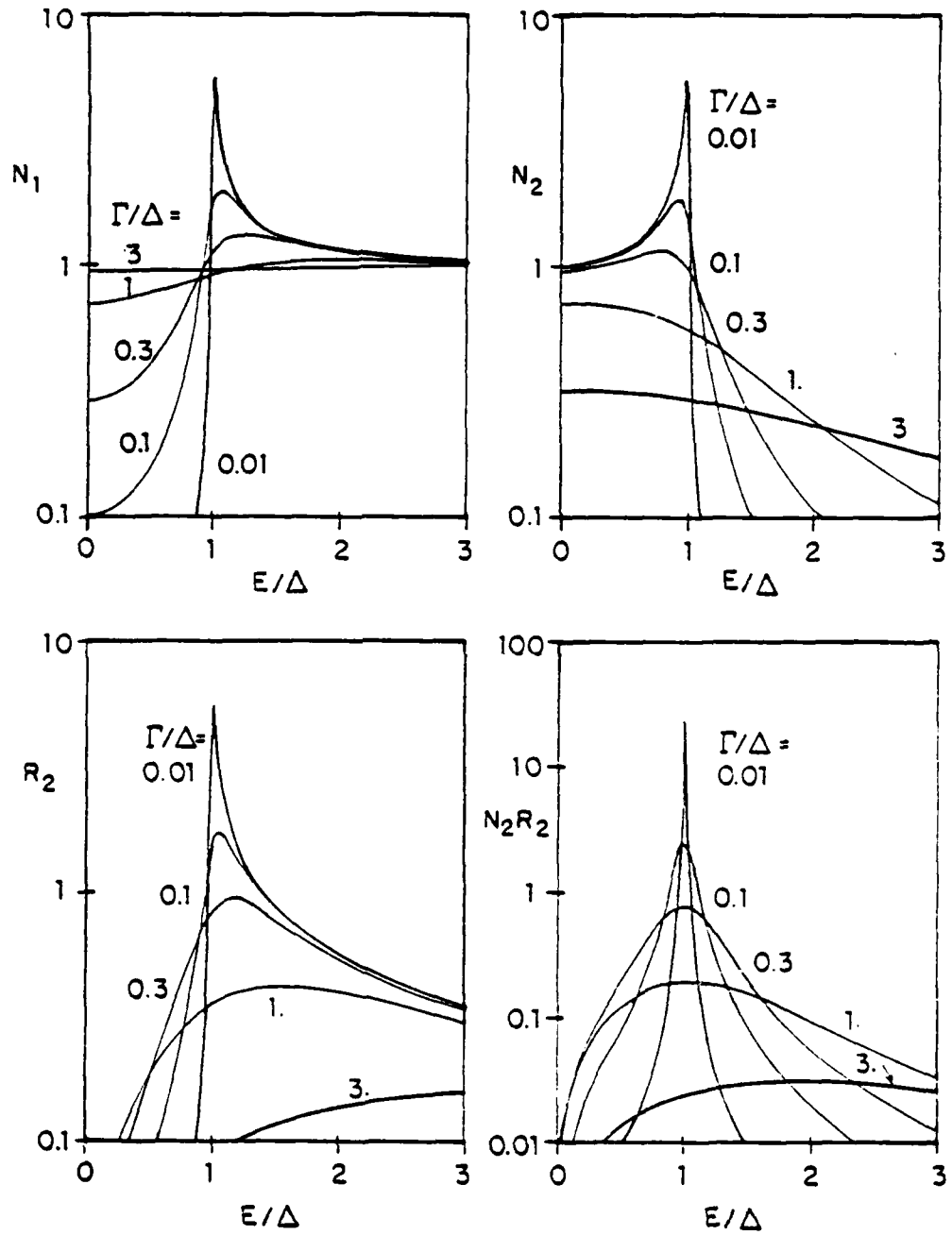


Figure 4-8 Semi-log plots of the important densities of states as functions of energy for various values of the pair-breaking potential.

integrals over these functions. In particular, this affects the approximations of the energy integral in Eq. (4-6), which appears in all of the approximate theories. If an accurate approximation to this integral could be found, it would probably significantly improve the agreement between the simpler theories and our exact calculations.

Referring back to Figure 4-4, the difference between the approximate and exact theories in the initial variation of the gap can also be explained. It is entirely due to the diffusion term in the Boltzmann equation (4-22a). In relatively clean materials such as indium, its effect is to decrease the initial drop of the order parameter. In dirty material such as the aluminum in Figure 4-7(b), the diffusion constant is smaller, and hence has a smaller effect. Thus, Figure 4-7(b) shows an initial drop in the gap much like that predicted by the simple theories, all of which completely ignore this diffusion term.

There is one last set of predictions, which will be useful for the next chapter. As mentioned in Chapter 3, the IBM experiments used a constant-height current pulse. A range of J_p 's was achieved by varying the temperature, and hence the critical current. In this situation, which is very different from that used for Figure 4-1, the delay time is very short when one measures just below T_c because the very small critical current results in a very large J_p . Furthermore, as T is decreased, the delay time increases until it diverges when I_c reaches I_p . A set of waveforms, modelled on one of our samples, is shown in Figure 4-9 to illustrate these effects. Several examples of the delay time versus $(1 - t)$ for these samples are included in the next chapter.

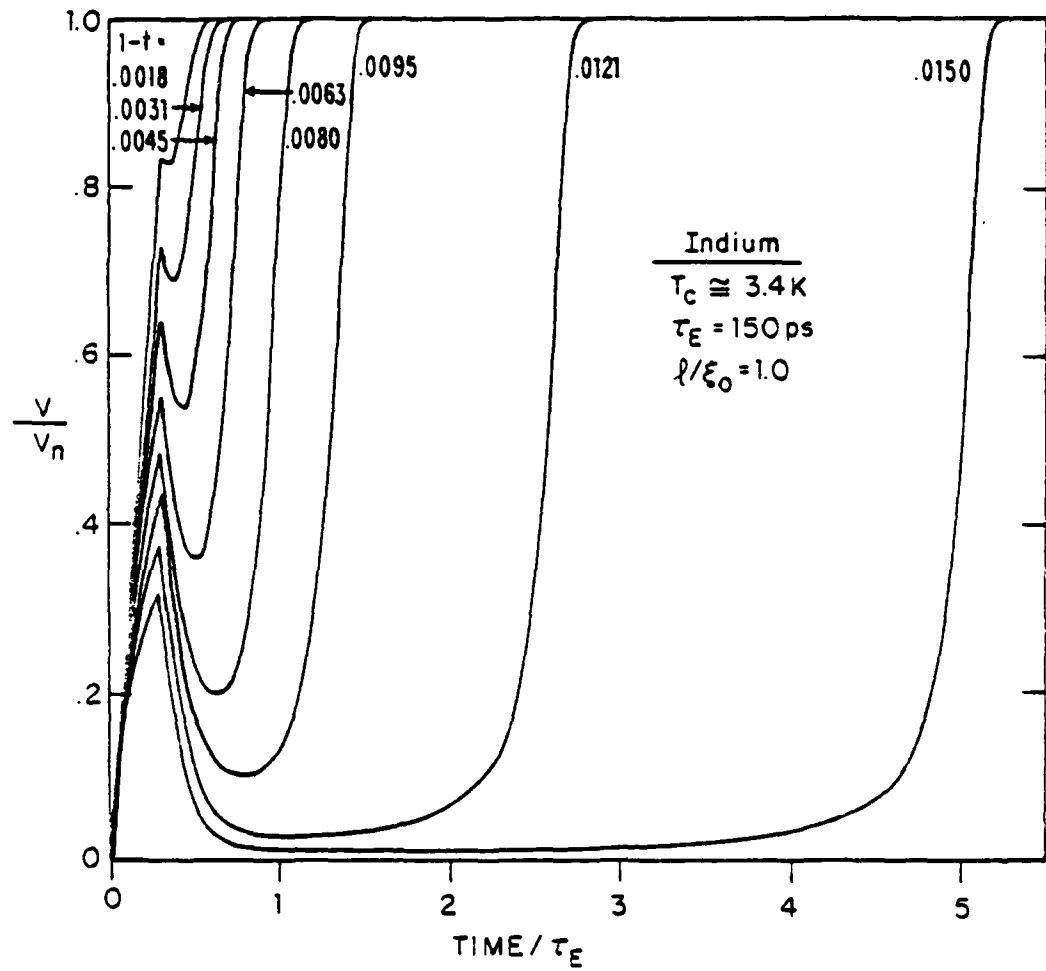


Figure 4-9 A set of waveforms simulating one of our IBM experiments, calculated using our exact numerical solution of the SST equations.

CHAPTER V

DATA ANALYSIS AND INTERPRETATION

5.1 Introduction

Using the tools and techniques described in the second and third chapters, we have made the first time-domain studies of the response of effectively one-dimensional indium microbridges to supercritical current pulses. The results of these experiments are presented in Section 2 of this chapter, along with theoretical comparisons and analyses based on the theories presented in Chapter 4.

We have also made a few of these same measurements on dirty aluminum microbridges. These results are presented and discussed in Section 3 of this chapter.

5.2 Indium Microbridges

We have made measurements on a variety of indium samples, some at Harvard and some in the collaboration with IBM. These were all fabricated using photolithography as described in Chapter 2. Most of them were fabricated on top of an SiO₂ layer, but a few were made directly on glass microscope slides. The measured properties of some of these samples are shown in the table below:

Table 5-1. Measured properties of selected indium samples.

sample ident.	dimensions (μm)	$\rho_{3.5}$ ($\mu\Omega\text{cm}$)	λ (\AA)	T_c (K)	$J_c(0)$ (MA/cm ²)
BJ35-4-1	111. x1.3x.20	0.39	2600	3.4245	67.4
BJ35-4-2	116. x1.7x.20	0.37	2700	3.4226	70.1
BK90-3-1	50.4x1.0x.22	0.20	5000	3.3991	112.
WMP1	127. x2.0x.15	0.32	3100	3.4144	82.2
1A	49.8x1.0x.21	0.24	4200	3.4031	117.
3A	176. x1.1x.21	-	-	3.399	-

The first three of these samples were measured in collaboration with IBM using their superconducting circuitry and the other three were measured at Harvard using conventional electronics. The dimensions were determined from photos taken with an optical microscope and from a digital thickness monitor used during evaporation. For the IBM strips, the residual resistivity at 3.5K, $\rho_{3.5}$, was inferred from the residual resistance and the dimensions; and for the Harvard strips, from the relation $\rho_{3.5} = \rho_{295} / (R_{295} / R_{3.5} - 1)$, where $\rho_{295} = 8.8 \mu\Omega\text{cm}$ for indium. We then used $\rho\lambda = 1. \times 10^{-11} \Omega\text{cm}^2$ for indium to determine the mean free path, λ . T_c and $J_c(0)$ were found by fitting J_c versus $t = T/T_c$ to the Ginzburg-Landau form $J_c(t) = J_c(0)(1-t)^{1.5}$, which the strips were found to follow quite well. We have not measured the diffusion length for these strips, but it is expected that it is in the 5-8 μm range.

The measured voltage waveforms for samples BJ35-4-1 and BK90-3-1 are shown in Figures 5-1 and 5-2, respectively. These were both taken with the IBM Josephson junction sampler chip. Another example of the data from the IBM collaboration was shown in Figure 3-6. Note that the curves are, at least qualitatively, in very good agreement with the theory (see, for example, Figure 4-3). Quantitative comparisons with theory are given in the following subsections. The initial kinetic

inductance spike and nonzero minimum voltage are discussed in 5.2.1 and the delay time until the rise to the normal state is dealt with in 5.2.2. Using the conventional electronics at Harvard, we have observed in the time domain the development of phase-slip centers. These data are discussed in 5.2.3.

5.2.1 Kinetic Inductance Spike and Nonzero Minimum Voltage

As we showed in the previous chapter, simple theoretical calculations indicate that there should be an inductive voltage spike associated with the rising edge of the current step. Furthermore, it was shown that there should be a nonzero minimum voltage between the inductive spike and the final rise to the normal state. Although this minimum voltage ought to become unobservably small as I_p approaches I_c , for $I_p/I_c \gtrsim 2$, it should be observable.

As can be seen from Figures 5-1 and 5-2, both of these effects are indeed present. This is the first experiment of this type in which these effects have been observed. These measurements were made possible by our use of the IBM superconducting circuitry. It had at least three characteristics that were very important in enabling us to observe these effects: the common ground plane for the entire circuit, which greatly reduced ringing due to the inductance of the signal lines, the very short rise-time of the superconducting pulse generator, and the high bandwidth and resolution of the Faris sampler.

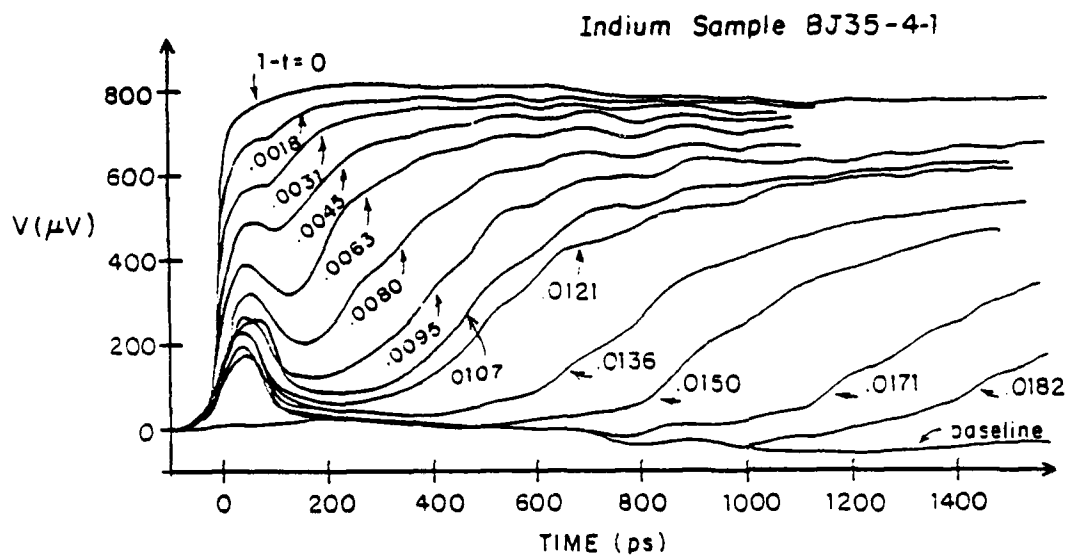


Figure 5-1 The voltage waveform data taken on sample BJ35-1-1 using the ISM circuitry.

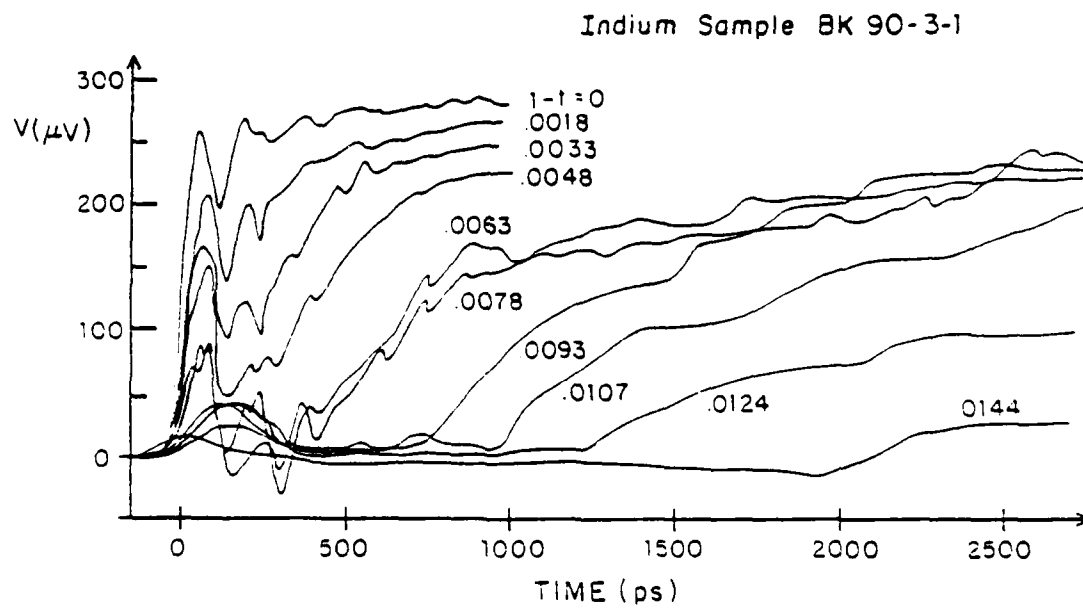


Figure 5-2 The voltage waveform data taken on sample BK90-3-1 using the IBM circuitry.

Figure 5-3 shows a comparison of the experimental waveforms and the theory for these two effects for three different temperatures. The theoretical curves were generated by our exact numerical solution of the SST equations (Schmid, Schön and Tinkham, 1980) using experimentally determined parameters and a value of τ_E obtained from our fits to the time delay data (see next section). Note that there is excellent agreement between theory and experiment considering that there are no adjustable parameters for this part of the curves.

We believe that the differences in these curves are, at least partially, due to waveform rounding caused by time jitter of perhaps as much as 25ps in the sampler and/or to the relatively crude model for the source voltage waveform that is used in the numerical solution. That model consists of a simple linear 45ps ramp from zero to the final level, after which it is completely flat. It seems clear that a model that incorporated some rounding in the rising portion of the pulse would come closer to matching the observed inductive spike.

Changing the rising edge of the current pulse, however, will only affect the rising portion of the inductive spike, its roundness and its amplitude. It will not affect the width of the spike or the location in time of the minimum. Yet the figure makes it clear that these are the aspects of the fit that most need to be improved. Within the model used, they are determined mostly by τ_J and τ_{GL} , which are determined by the T_C and by $1-t$. An improved fit might be obtained by significantly increasing τ_J and τ_{GL} , but there is no apparent theoretical justification for doing this. These difficulties in the fit might also be due to capacitance and inductance in the rest of the

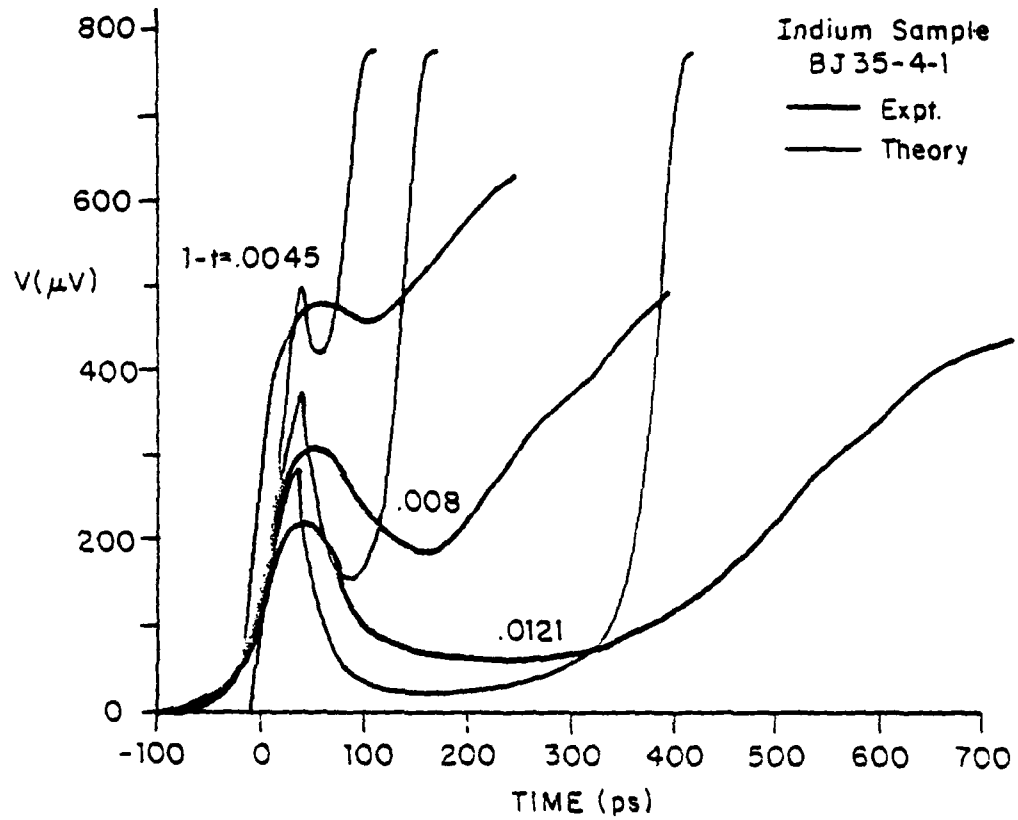


Figure 5-3 Comparison of experimental and theoretical waveforms for IBM sample BJ35-4-1 for three different temperatures. The parameters used in the theory are those that were measured for this sample.

circuit or to nonuniformity of the strip. At the present time we do not know which of these possibilities is the best explanation for these discrepancies in the fit at short times.

For the sake of a more detailed comparison with theory, Figure 5-4 compares the spike height versus $1-t$ for two of the strips with the theoretically predicted heights, where the parameters of the theory are set as before. Particularly, a risetime of 45ps has been used for both curves. Note that although the agreement is not excellent, there is general qualitative agreement. Furthermore, the magnitude difference for sample BJ35-4-2 could certainly be adjusted by lengthening the rise-time used. The difference in functional dependence, however, could probably be decreased only by taking into account the effects discussed above.

The minimum voltage versus $1-t$ for two of the strips is compared with theory in Figure 5-5. As can be seen, the agreement between theory and experiment is much better for this aspect of the waveforms. Note particularly that the functional form is accurately predicted by theory.

Thus, we have successfully observed the initial inductive spike and nonzero minimum voltage in indium microbridges. We find that the minimum voltage is adequately described by the theory, but that the fit between theory and experiment for the spike height and width leaves something to be desired.

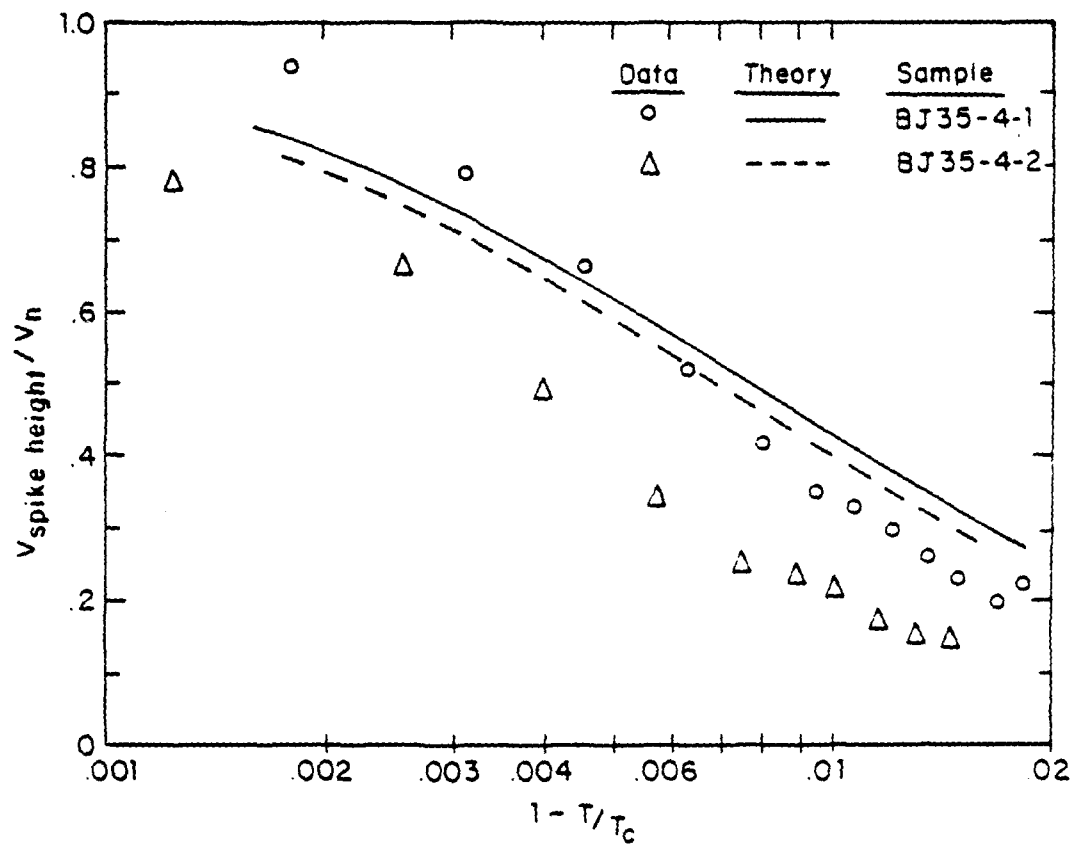


Figure 5-4 Measured inductive spike height as a function of temperature for two of the IBM samples. The solid and dashed lines are the theoretical predictions for the two samples.

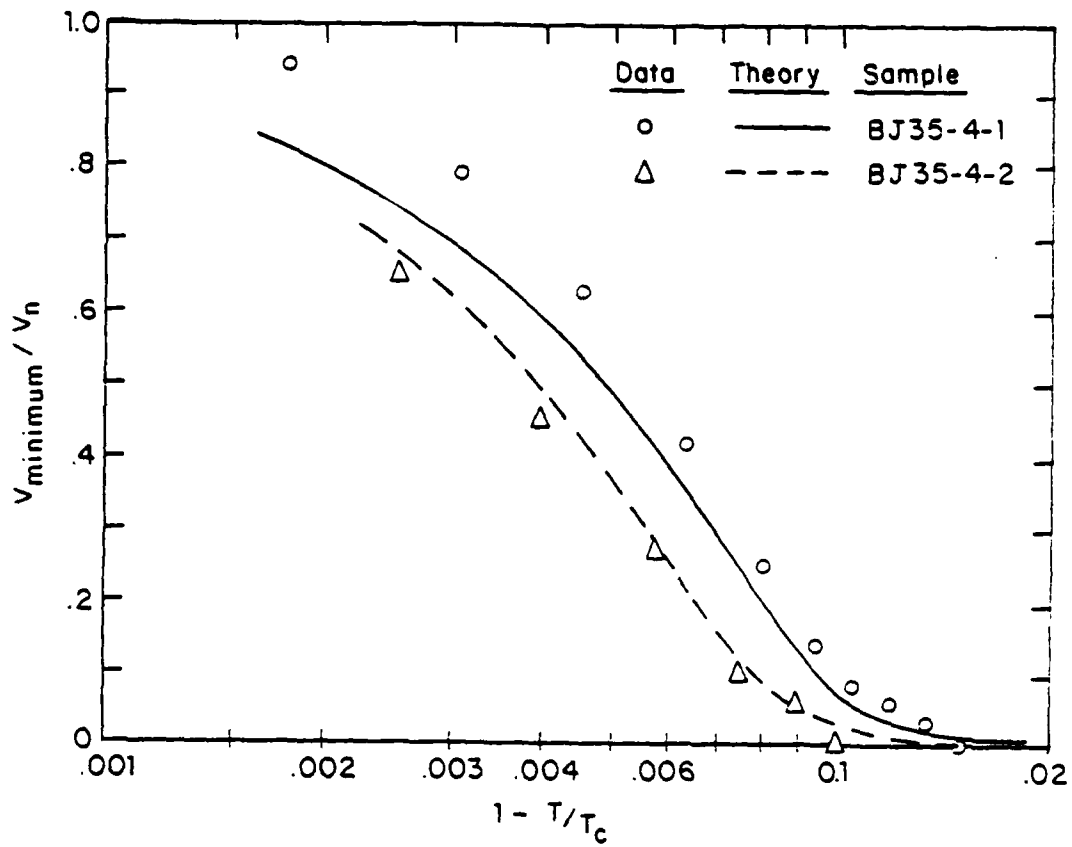


Figure 5-3 Measured minimum voltage as a function of temperature for two of the IBM samples. The solid and dashed lines are the theoretical predictions for the two samples.

5.2.2 Delay Time

We have been able to make delay time measurements on indium strips using both the IBM setup and the Harvard equipment. These are the first delay time measurements on effectively one-dimensional indium strips. Some typical waveforms were shown in Figures 2-13, 3-6, 5-1 and 5-2. We take a value for the delay time, t_d , from each of these curves according to the definition discussed below and fit these results with SST theory. From these fits we have obtained an estimate of τ_E for indium that agrees reasonably well with other estimates based on different experiments.

Figure 5-6 demonstrates our t_d definitions. The wider line represents an experimental waveform and the narrower one a theoretical calculation. We have defined the delay time as beginning at that point at which 60% of the rise-time has elapsed. This definition is used to reduce the discrepancies caused by rise-time differences between theory and experiment. As indicated in the figure, the end point of t_d for the experimental data is defined as that point at which the voltage has risen 10% of the way from its minimum point to its maximum value at long times. For the theoretical curve, the end point is defined at the point when the voltage has risen 50% of the way from its minimum to its maximum.

The 10% definition is used for the experimental data because only the very first portion of the rising edge can be thought to have any direct relationship to the simplified theory we have been using. The choice of exactly 10% is arbitrary. The rest of the rising edge is

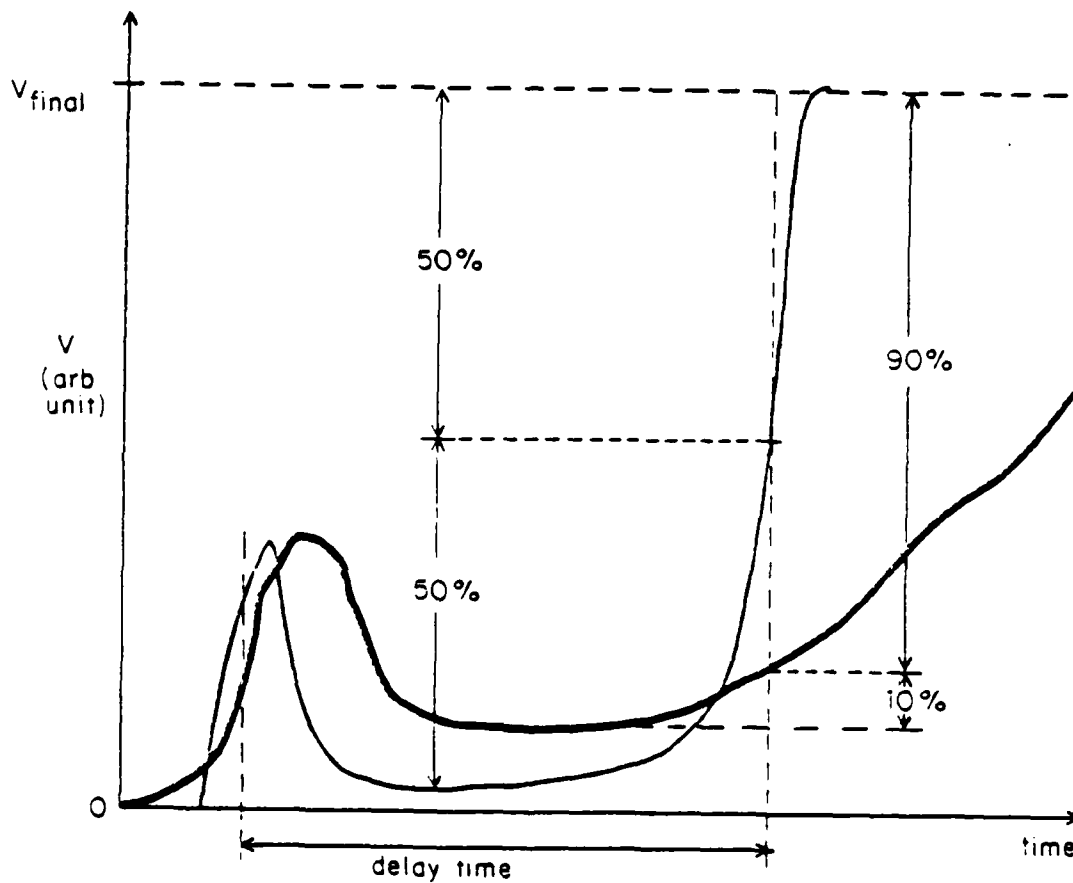


Figure 5-6 Illustration of our delay time definition for comparison of theory and experiment. The thinner line is the theoretical curve and the broader line represents a data curve.

always observed to rise much more slowly than the theoretical model predicts. There are many possible explanations for these long rise-times. They may be due to transverse nonequilibrium effects, to heating, to the development of phase-slip-centers or to some combination of these effects. None of these factors are taken into account in our theoretical calculations. The 50% point of the theory is chosen rather arbitrarily. It is approximately the steepest part of the curve and, furthermore, the choice of 50% minimizes the possible error in the event that a different point should have been chosen.

Using these definitions we have determined delay times for all of the waveforms taken on the three IBM scientific chip samples listed in Table 5-1. These data are presented in Figure 5-7 along with our best theoretical fit for each curve. τ_E is the only adjustable parameter in each of these fits, except for the fit to the 8K90-3-1 data. For that data we also fit the height of the current step, since it was not accurately determined during the experiment. The fits are based on only the delay time points for $(1-t) > .007$, where there is relatively good agreement. The large discrepancies for $(1-t) < .007$, where the delay times are quite short, are probably, at least in part, due to the sensitivity of these points to the exact form of the rising edge of the current pulse; as mentioned before, only a crude approximation to the rise-time has been put into the theoretical calculations. Other possible sources of these discrepancies are the same as those discussed in the previous subsection in connection with the inductive spike width and the location in time of the minimum voltage. Since we do not know which effects to take into account, we have not attempted to improve

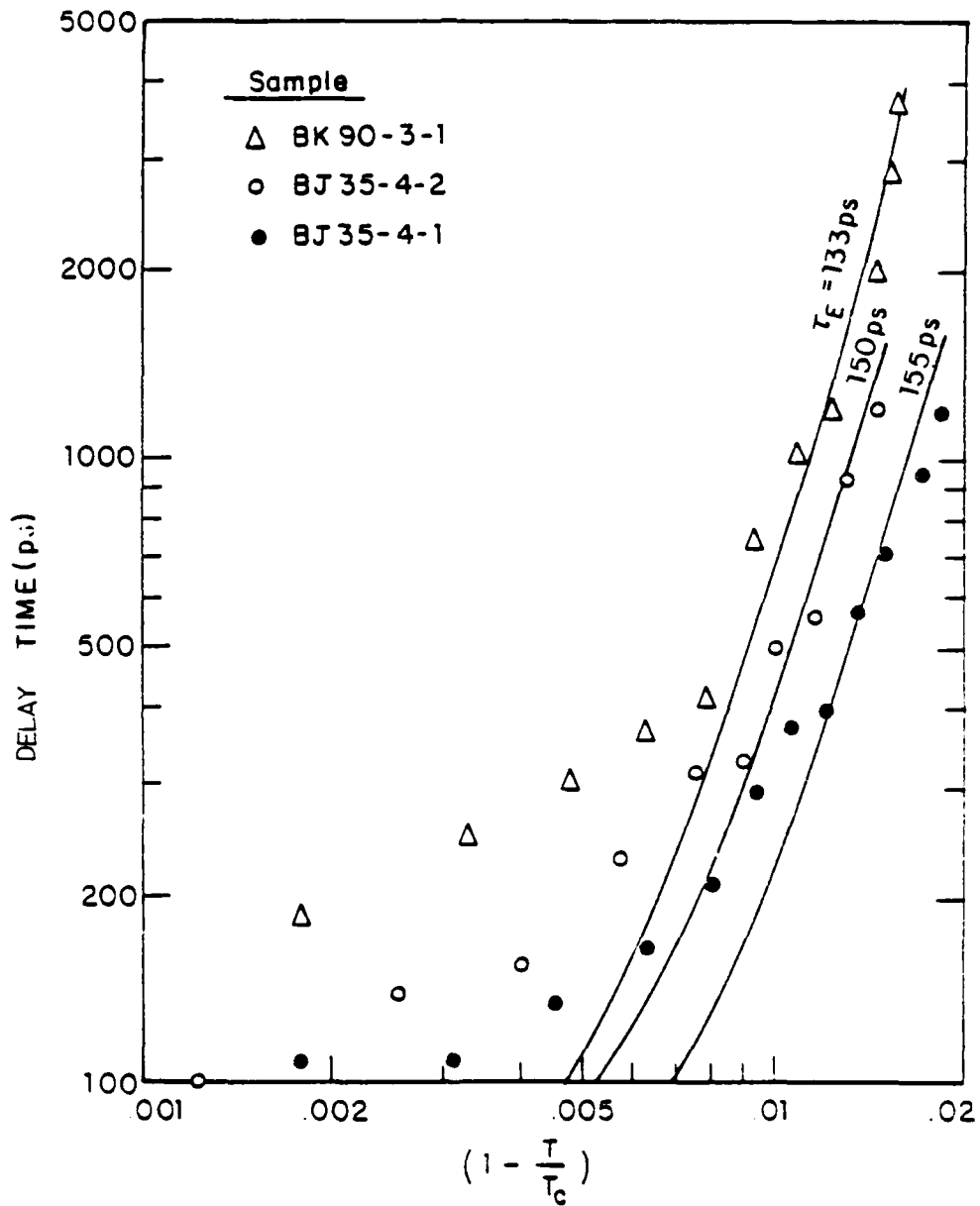


Figure 5-7 Measured delay time versus $(1 - T/T_c)$ for the IBM samples. The solid line for each sample is a fit to the theory for the points for which $T/T_c < 0.992$.

this part of the fit. As shown in the figure, the fits to the longer t_d points give 133, 150 and 155 picoseconds for the values of τ_E for these three samples.

We have also evaluated the delay time data taken here at Harvard on indium microbridges, using the same t_d definition as for the IBM data. (For an example of the waveforms, see Figure 2-13.) Figure 5-8 shows a plot of the t_d data taken on sample 1A at four different reduced temperatures. Lower reduced temperatures were not studied because of limitations on the magnitude of our current pulses. In all of these curves, we have used a DC bias current (i.e., a nonzero baseline voltage) to fine-tune the value of I_p/I_c , where $I_p = I_{\text{baseline}} + I_{\text{step}}$ is the total height of the current during a pulse. As discussed in Chapter 4, the delay time in this situation is expected to depend almost entirely on I_p/I_c , unless I_{baseline} becomes significant compared to I_c . Furthermore, in our theoretical calculations we have taken into account the DC biases that were used, so that the theoretical conditions are exactly the same as the experimental conditions. All four of the theoretical curves were generated using $\tau_E = 116\text{ps}$, which was found to give a good fit. Although the fit between data and theory is not perfect, it is acceptable at all four temperatures and clearly demonstrates that the expected temperature dependence of the delay time is indeed observed in these indium strips.

Putting together all of the estimates of τ_E from our various experiments, we obtain $\tau_E = 140 \pm 25\text{ps}$ for indium. This value is in reasonable agreement with the 110ps reported by Hsiang and Clarke(1980), and is very close to the 136ps inferred from Jillie's measurements of

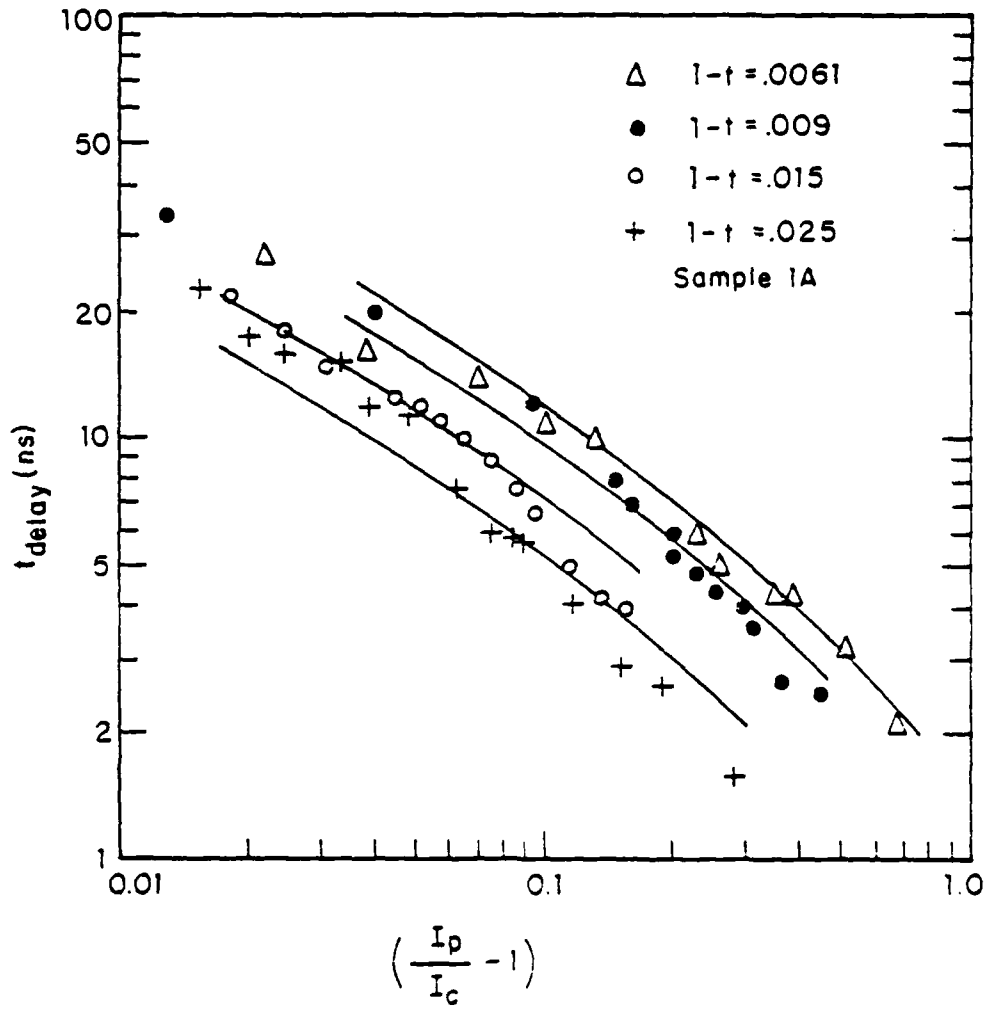


Figure 5-8 Plot of the delay time versus $(I_p/I_c - 1)$ for four different temperatures. This data was taken at Harvard using the more recent experimental setup.

the quasiparticle diffusion length (Jillie 1976). (In making this comparison we have used a value of the diffusion constant that is consistent with our own work rather than his value.) It is somewhat higher than the theoretical value of 95ps obtained by Kaplan, et al. (1976).

5.2.3 The Development of Phase-slip Centers

Using the conventional electronics at Harvard, we have been able to observe the time-domain development of phase-slip centers (PSC's). As would be expected, our long one-dimensional indium filaments show PSC's on their DC I-V curves, except when heating effects obliterate them. We have observed the development of these PSC's in time and have correlated the steps seen in the time domain with those seen in the corresponding I-V curves.

Figure 5-9 shows a typical example for sample 3A at $(1-t)=0.006$. Its I-V curve is shown in (a) and the corresponding voltage waveforms at various values of I_p/I_c are shown in (b). As can be seen in (b), the voltage at $t \sim 100$ ns proceeds through four relatively clear step levels as I_p/I_c increases. After the fourth step, the voltage level continues to increase as the current ratio is increased.

These features correspond to the first four steps in the I-V curve. Note that the first three steps in (a) are relatively short and that the fourth step rises substantially further, as the current is increased, before the jump to the fifth step occurs. These short steps give rise to the relatively narrow voltage levels in (b), while the longer fourth

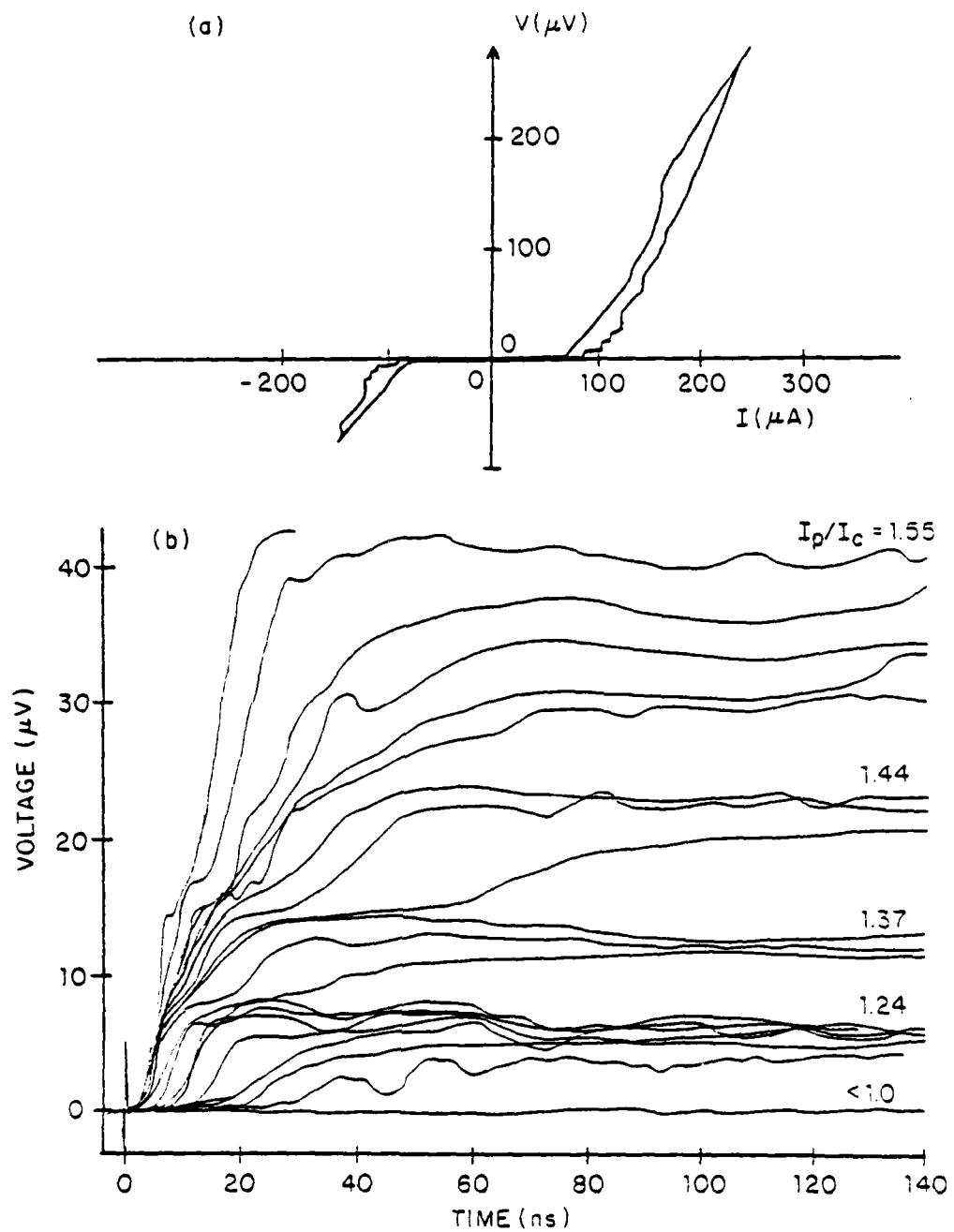


Figure 5-9 (a) An I-V curve showing phase slip centers, and (b) the time-domain development of these same phase slip centers. This data was taken at a fixed temperature of $(1-T/T_c)=0.006$.

step causes the wider range of voltages above the fourth step in (b). If the values of I_p/I_c in (b) are extended to slightly higher values than those shown in the figure, a fifth step transition is indeed seen.

The figure also shows how each of these steps develops in time. When the current level only slightly exceeds the critical current for a given PSC, there is a long delay time before that PSC develops a voltage drop. As the critical current of a given PSC is increasingly exceeded, the delay time before it develops decreases.

Figure 5-10 shows a plot of the delay time versus I_p/I_c for the four PSC's shown in Figure 5-9(b). For the purposes of this plot, the delay time for each PSC has been defined as the elapsed time until the voltage reaches a level about 10% of the way up from the previous phase-slip center's voltage level. For the short delay times this definition is probably fairly dubious, but it is useful for providing qualitative insight into the longer delay times.

As can be seen from the plot, each PSC's delay time diverges at its own I_c . Note that these critical currents agree quite well with those that one would determine from the I-V curve. Furthermore, the delay time curves for the second, third and fourth PSC's are fairly accurate translations, along the I_p/I_c axis, of the curve for the first PSC. Since the axis is a log scale, this means that each curve is just a simple t_d versus I_p/I_c curve normalized to the appropriate I_c for each PSC. This is demonstrated in Figure 5-11, which shows the delay time for each PSC plotted against I_p/I_c^* , where I_c^* is its effective critical current. The solid line is the theoretically generated $t_d(I_p/I_c)$ for

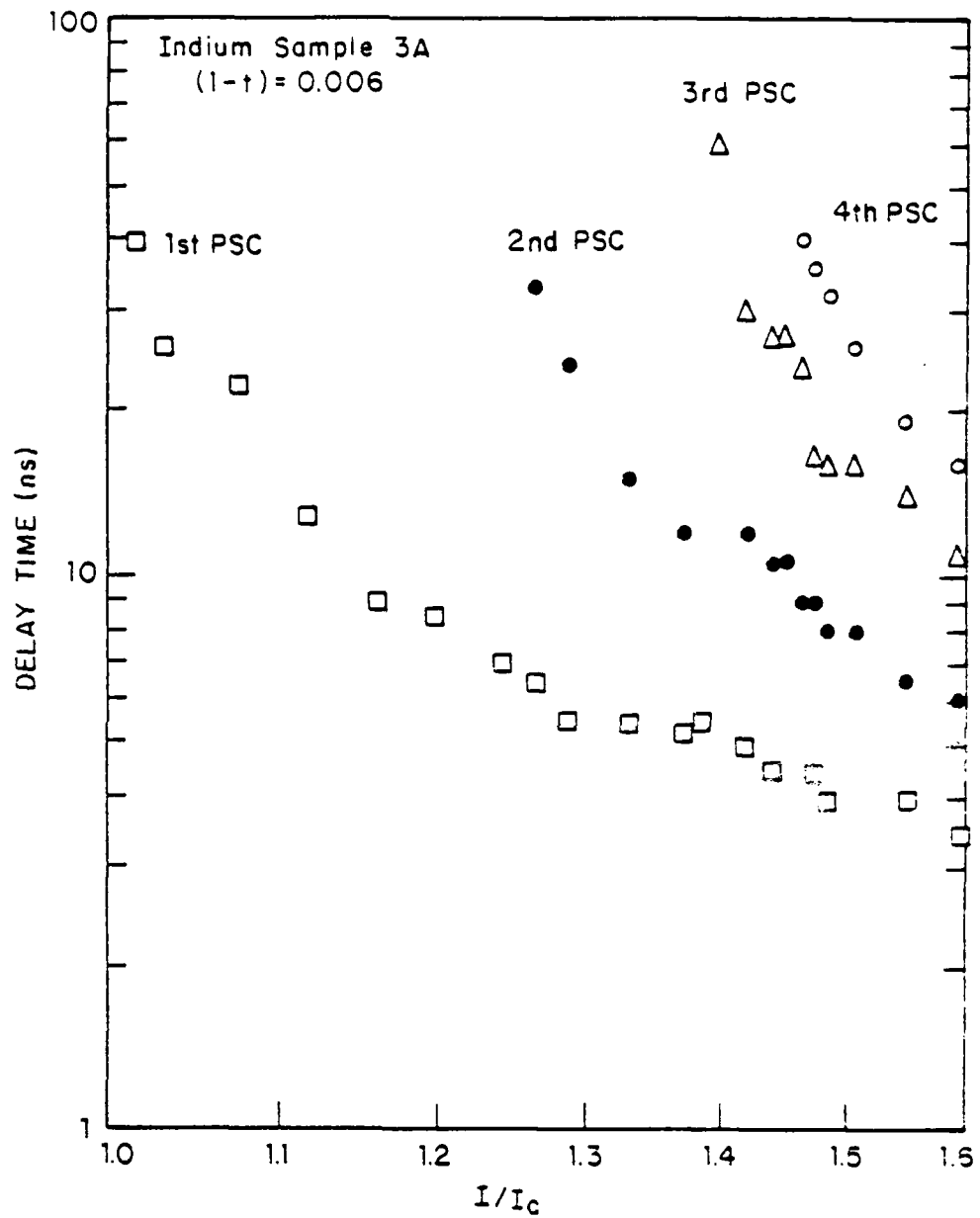


Figure 5-10 The measured delay time as a function of I/I_c for each of the four PSC's seen in the waveforms in Figure 5-9(b).

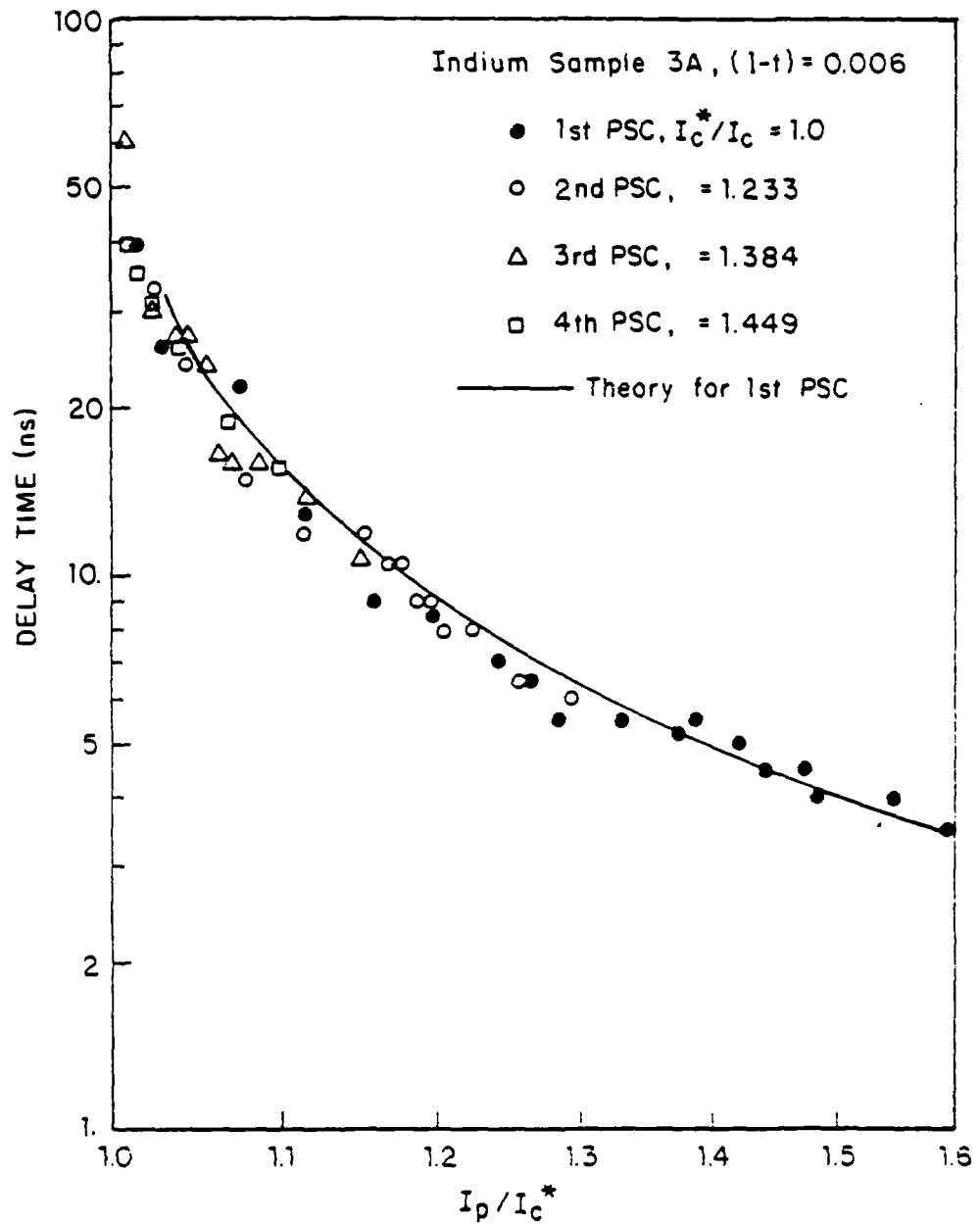


Figure 5-11 The measured delay time for each PSC in Figure 5-10 plotted against I_p/I_c^* , where I_c^* is the effective critical current of each PSC. The solid line is the theoretical prediction for the first PSC.

the first PSC ($\tau_E=148\text{ps}$). As can be clearly seen, the higher PSC's all fairly accurately follow the theory for a simple uniform strip, at least for these relatively long times.

It therefore appears that a very simple model can be used to explain these results. Namely, that each PSC can be thought of as an independent, uniform one-dimensional strip with its own I_c . When the current through the microbridge exceeds the I_c of a given PSC strip, that strip develops its normal state voltage after a delay time that is given by our theories in the previous chapter. Clearly, this model is not in any sense exact, since the effective critical currents of the PSC's depend on the quasiparticle currents from previous PSC's (Aponte, 1982) and, hence, are not constant in time. Nevertheless, the model clearly gives good results for these fairly long delay times.

We have also observed what appears to be thermal hotspot growth in some of our more hysteretic microbridges. This appears in the waveforms as a linear increase in voltage with time. We have inferred from these waveforms a growth rate of $\sim 25,000\text{cm/sec}$ which seems to be reasonable (Cherry and Gittleman, 1960). Any detailed comparison with theory is very difficult, however, because of the nonequilibrium processes involved.

To the best of our knowledge, this is the first reported observation of the time-domain development of PSC's and the growth of thermal hotspots in truly one-dimensional microbridges such as ours. We have observed these effects both in indium and in the dirty aluminum microbridges that are discussed in the next section.

5.3 Aluminum Microbridges

We made some measurements on a few dirty aluminum microbridges in the initial stages of our experimentation. These were fabricated using the techniques described in Section 2.2.3. The dirty aluminum used had a T_c of $\sim 1.54K$ and a mean free path of $\sim 40\text{\AA}$. As mentioned in Chapter 2, these strips were wider than $\xi_{GL}(T)$ in the useful temperature range, but were narrower than $\lambda(T)$, the magnetic field penetration depth. We found that the $I_c(T)$ of these strips did not follow the Ginzburg-Landau form at all. In fact, it varied approximately as $(1-T/T_c)^{0.9}$. This is probably because the granularity of the films causes their critical currents to be determined mostly by the inter-grain coupling strength. As a result, our simple theories cannot be expected to apply to these strips.

Nevertheless, we did carry out some experiments on the microbridges, partly to gain experience and understanding in making the measurements, and partly to determine what the transient response of these strips would be. Two examples of the waveforms obtained were shown in Figure 2-10.

As can be seen from that figure, there is a current-dependent delay before the development of voltage. Figure 5-12 shows a plot of this delay time (defined as in Section 5.2.2) as a function of $(I_p/I_c - 1)$ for the same strip at four different temperatures. Since this data does resemble our theory, we have included a theoretical fit (continuous line) for each reduced temperature. The value of τ_E needed for each of

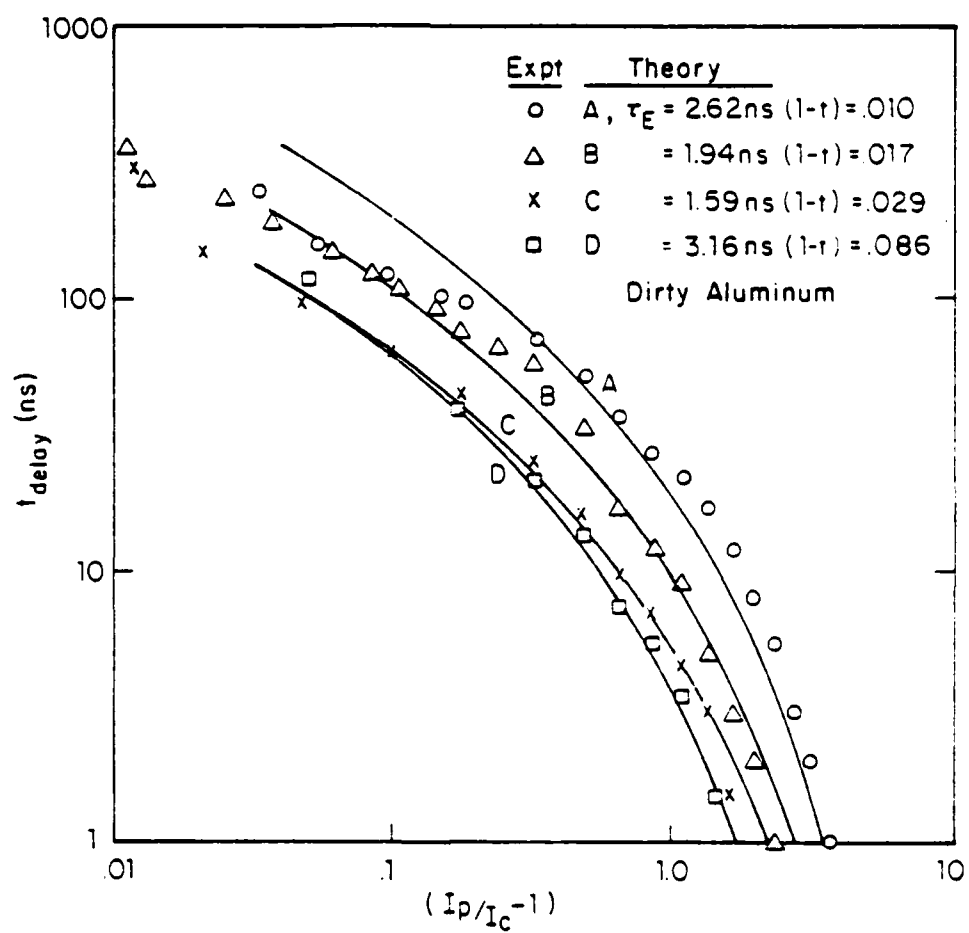


Figure 5-12 Plot of the delay time versus $(I_p/I_c - 1)$ for four different temperatures for one of our dirty aluminum bridges, with a theoretical fit given for each temperature.

these curves is indicated in the figure. The average of these values is $2.4 \pm 0.8 \text{ ns}$, which is consistent with the work of Chi and Clarke (1979). Note, however, that little significance should be placed on this number, since the spread in values for τ_E is an indication of the inapplicability of our theory.

We also tested a dirtier aluminum strip made by W. C. Danchi for other purposes. It had a T_c of $\sim 1.84 \text{ K}$, and had a more Ginzburg-Landau-like $I_c(T)$ that varied as $(1-T/T_c)^{1.3}$. It yielded a value of $1.15 \pm 0.25 \text{ ns}$ for τ_E , which is also consistent with the work of Chi and Clarke.

The time-domain development of PSC's was also observed in these aluminum micorbridges. Figure 5-13 shows an example of this. These waveforms were taken at a temperature slightly above the T_c of the weakest part of the strip. The rest of the strip was, however, superconducting. Hence, the curves are parameterized by I_p/I_0 , where I_0 is the critical current of the first PSC in the rest of the strip. The step at $I_p/I_0 = 1.0$ is due to the part of the strip that is still normal. The waveforms at this temperature are displayed because they clearly show the time-domain development of several PSC's. At lower temperatures, the strips become hysteretic and thermal hot-spot growth tends to make the development of the PSC's less distinct.

Although our measurements on these dirty aluminum strips show qualitatively all of the effects that would be expected, it would have been necessary to use less dirty aluminum to obtain the more Ginzburg-Landau-like behavior required for our theories. But, since we

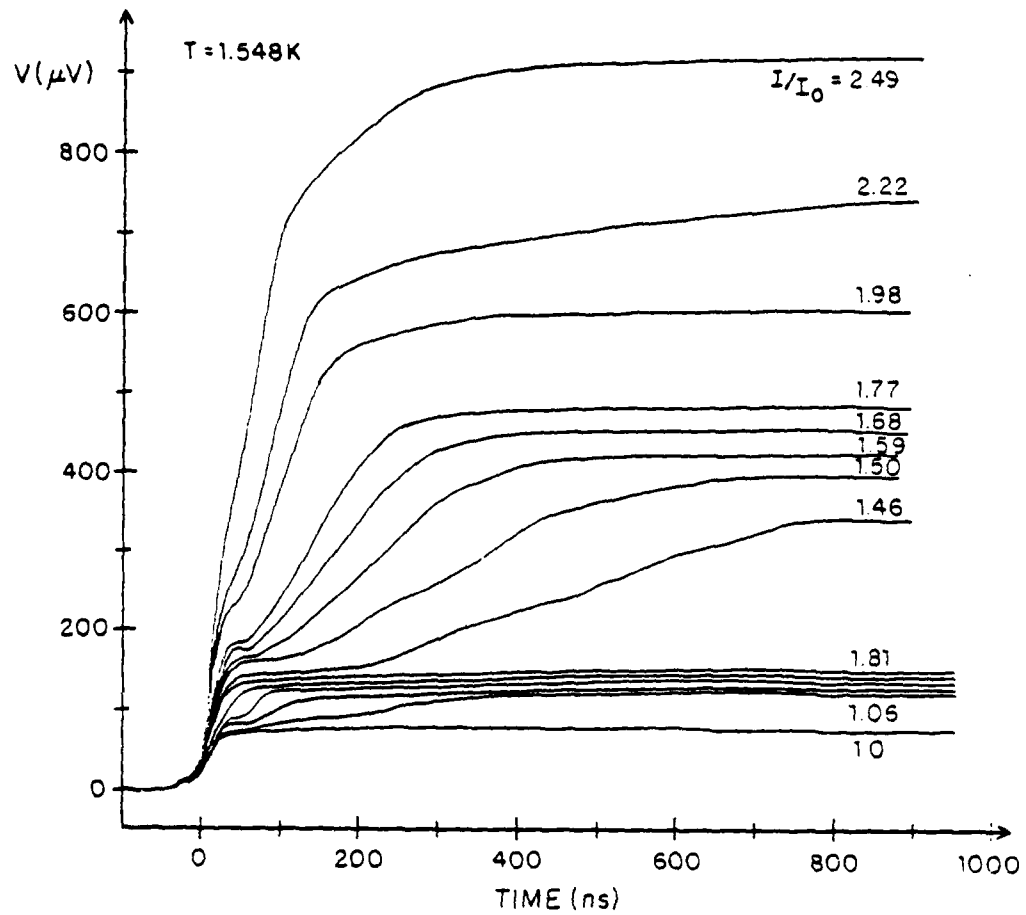


Figure 5-13 Set of voltage waveforms for a dirty aluminum bridge demonstrating the time-domain development of PSC's.

were limited to $T > 1.3\text{K}$, and since Wolter, et al. (1981) have already made many measurements on clean aluminum, we chose, instead, to concentrate most of our efforts on measuring the properties of the indium microbridges reported earlier in this chapter.

CHAPTER VI

POSSIBLE FUTURE EXPERIMENTS

6.1 Introduction

During the course of this work we identified two interesting variations on our original experiment. These are presented here as possible future extensions of the present work.

The next section describes the first variation, which involves observing the destruction of superconductivity due to a pulsed magnetic field. In the second experiment, which is discussed in Section 6.3, a burst of RF current, rather than a DC current pulse, is applied to a superconducting microbridge.

6.2 Destruction of Superconductivity by a Pulsed Magnetic Field

Just as superconductivity can be destroyed by excess current, it can also be destroyed by a magnetic field in excess of its critical magnetic field. An interesting experiment, which, to the best of our knowledge, has never been done, would be to observe the time required for the superconductivity of an effectively one-dimensional filament to be suppressed by the sudden application of a magnetic field. An experimental arrangement for such a measurement is shown in Figure 6-1.

The suggested arrangement uses the magnetic field in a superconducting stripline. This magnetic field can be quite well

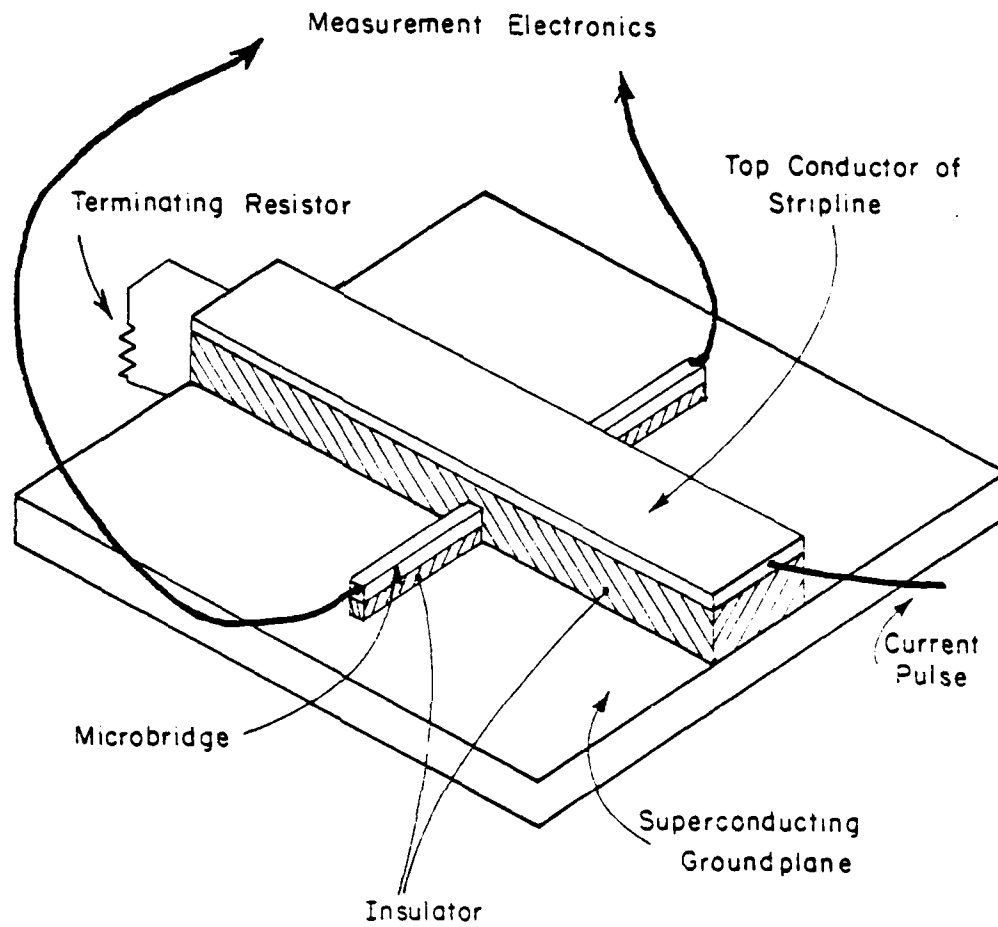


Figure 6-1 Possible experimental configuration for observing the time-domain destruction of superconductivity by a pulsed magnetic field.

characterized, is perpendicular to the direction of stripline current flow and is simply proportional to the magnitude of the current. Furthermore the rise-time of the field is the same as that of the current that produces it, which can be made very short. The one-dimensional filament would be fabricated through the stripline, perpendicular to it, so that, ideally, direct inductive coupling would be eliminated. The superconducting or normal nature of the microbridge could be observed by passing a small DC bias current through it and observing the voltage.

There seem to be two primary difficulties in this experiment. First, the parallel critical magnetic field of such filaments increases inversely with their thickness or width, whichever is smaller. This means that relatively large fields must be used, and, hence, relatively large currents in the stripline. Furthermore, the stripline materials must be chosen to withstand these currents and magnetic fields. Second, the large fields mean that substantial inductive pick-up could be expected, even on nearly ideally fabricated samples. Techniques would need to be developed to subtract this background from the desired signal.

We have done only a small amount of theoretical work on this problem. As a result we do not know whether the transient phenomena of this experiment would be expected to be significantly different from those of our current pulse experiments. It seems possible that there might be observable differences, however, since the theoretical analysis of this experiment within the SST framework would necessarily proceed rather differently than that of our experiment. Particularly, a

different gauge choice must be made, and various gradient terms must be taken into account. It would be interesting to complete a theoretical analysis of this problem to determine the ways in which it might be expected to differ from our present experiment.

6.3 Destruction of Superconductivity by a Burst of RF Current

A time-domain study of the response of a superconducting microbridge to an RF current pulse would be interesting for several reasons. Since sufficient RF current can destroy superconductivity, one could measure the time required to do so and compare it with theory. This should be an effective test for the effect of the diffusion terms that depend on \dot{Q} in the SST equations. Furthermore, by varying the frequency of the RF, one could probably gain insight into the time constants of the various regimes. It might also provide additional insight into the causes of gap and critical current enhancement due to microwaves (Mooij 1981). Additional information might be provided for this last purpose by studying the results of combining DC with the RF burst.

This experiment could be done in a manner very similar to our present experiment; the difference being that the DC pulse generator would be replaced by an RF burst generator. If the RF were synchronous, one could observe the effect of each cycle using a sampling oscilloscope; while if the RF were asynchronous, one could measure the behavior averaged over all phases. Either of these measurements would probably be interesting.

Since this experiment involves only current through a strip, we were able to use our exact computer program (see Appendix B) with only a few minor modifications to determine some theoretically expected results. Figure 6-2 shows the result when a 7GHz current burst with a peak amplitude of 4.5 times the critical current is imposed on a relatively clean indium strip. The applied current waveform is shown in 6-2(a), the voltage waveform in 6-2(b) and the corresponding value of the energy gap in 6-2(c). Note that the voltage waveform develops a very complicated structure and that the gap undergoes its undulations every half cycle, i.e., at twice the applied frequency. These features are typical of all of the cases we have investigated. We have also found that in at least one case the delay time until the strip goes normal increases significantly as the material is made dirtier and in all cases it is much longer than it would have been for an equivalent DC pulse. Based on our preliminary studies, this experiment seems to yield very interesting results and probably deserves further study.

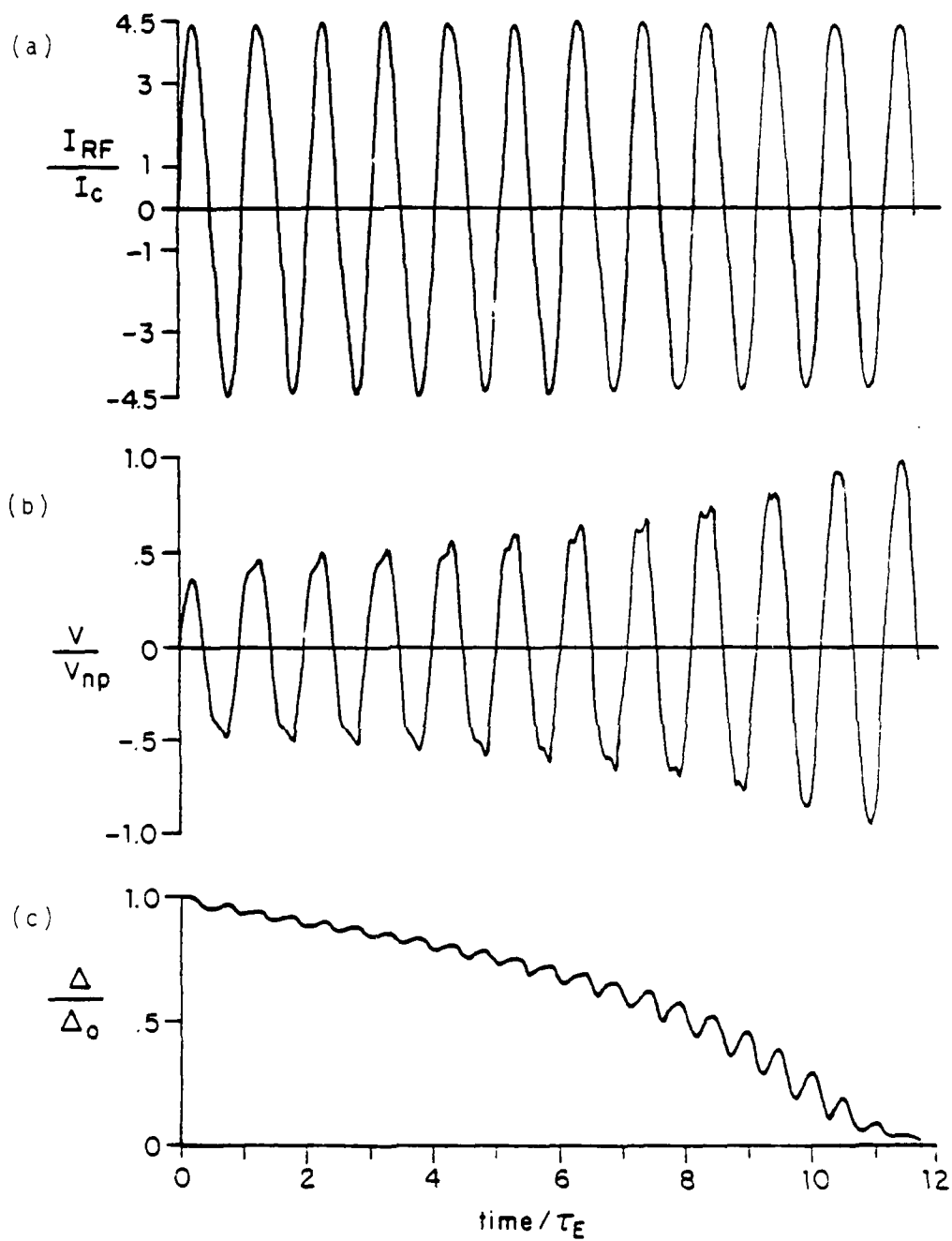


Figure 6-2 (a) An applied 7GHz current burst and (b) the resulting voltage and (c) gap variation with time.

CHAPTER VII

SUMMARY AND CONCLUSION

In the previous chapters we have discussed the various aspects of our time-resolved measurements of the voltage waveforms on one-dimensional superconducting strips caused by current pulses in excess of their critical currents. In this chapter we summarize our work and our conclusions.

The experiments were carried out in two ways: using conventional electronics in the laboratory at Harvard and using a superconducting sampler circuit and pulse generator in a collaboration with IBM. The Harvard experiments involved the construction of several pulse generators and the use of high frequency sampling electronics, all of which has been described in detail. The experiments at IBM used the Josephson computer technology to place the pulse generator, microbridge and sampler all on the same ground plane. This was found to result in a great reduction in extraneous signals and should be a useful technique for many other experiments. This is the first known use of this superconducting circuitry for a nonequilibrium superconductivity experiment. In both types of experiments, the microbridges were fabricated by projection photolithography using a small photolithographic facility that we helped to develop at Harvard.

The data we have taken using these methods include the first known observations of the kinetic inductance spike, the non-zero minimum

voltage, and the time-domain development of phase slip centers. These measurements were made on indium microbridges and represent an important extension of the work of Pals and Wolter (1979) to a higher critical temperature material. In addition, we have measured the delay time between the application of the current pulse and the development of the first phase slip center in these bridges and have fit this data with the predictions of the SST theory (Schmid, Schön and Tinkham 1980) to obtain an estimate of 140 picoseconds for τ_E in indium. This estimate is in good agreement with the values obtained by other workers. We have also measured the delay times until the appearance of the higher phase slip centers and have shown that they are consistent with a simple model in which each phase slip center is treated as an independent ideal strip with its own effective critical current. In addition, we have made a few measurements on dirty aluminum strips which also show the time-domain development of phase slip centers.

We have compared the data with the nonequilibrium superconductivity theory of SST wherever possible. To do this, we have developed a computer program that numerically solves the SST equations exactly in the one-dimensional, uniform strip approximation. From these numerical solutions we have found that, for the most part, the theory is in good agreement with the data. This agreement is best for the longer delay times and for the magnitude of the minimum voltage, but is only qualitative for the time scales below ~ 200 ps that were observable with the IBM setup. We have suggested several explanations for these discrepancies, but do not know which, if any, is correct. We have also used this exact solution to test the validity of several simpler

approximations, including Tinkham's phenomenological approach, which we have used to provide an intuitive understanding of the physics involved in this experiment.

Although this^{is} not an "easy" experiment, it does seem to be a fairly accurate way of obtaining an estimate of τ_E which is nearly independent of the other parameters of the material. As a result, it would probably be both useful and interesting to apply this technique to a variety of other superconductors.

APPENDIX A
TUNNEL DIODE-BASED PULSE GENERATOR

As discussed in Chapter 2, the later experiments at Harvard required a shorter rise-time pulse generator. We designed and built a tunnel diode-based pulse generator to meet this requirement. Its notable features include an adjustable baseline for the pulses, self adjustment of the current bias on the tunnel diode and a circuit that can measure the critical current of the strip during the time between the pulses. This last measurement provides an output voltage proportional to the current at which the sample voltage exceeds a small preset value. It is combined with the source pulse height in an analog divider that provides a direct output of the ratio $-I_p/I_c$. The pulse generator can also be switched out of the pulse mode into a DC I-V mode with load line compensation.

A block diagram of the pulse generator is shown in Figure A-1(a). The circuitry is all solid state, consisting of 41 integrated circuits, one module and various discrete components. It is constructed on two 6"x6" double-sided printed circuit boards which we designed for this purpose. One of the circuit boards contains the digital timing logic (18) and the other one contains all of the linear circuitry. These boards are mounted in a sturdy aluminum box which provides shielding between the boards and from ambient noise. They consume about 7 watts from an external ± 5 , +12 and ± 15 volt power supply. Switches S1, S2, S4 and S5 are CMOS bilateral switches controlled by the timing logic (18).

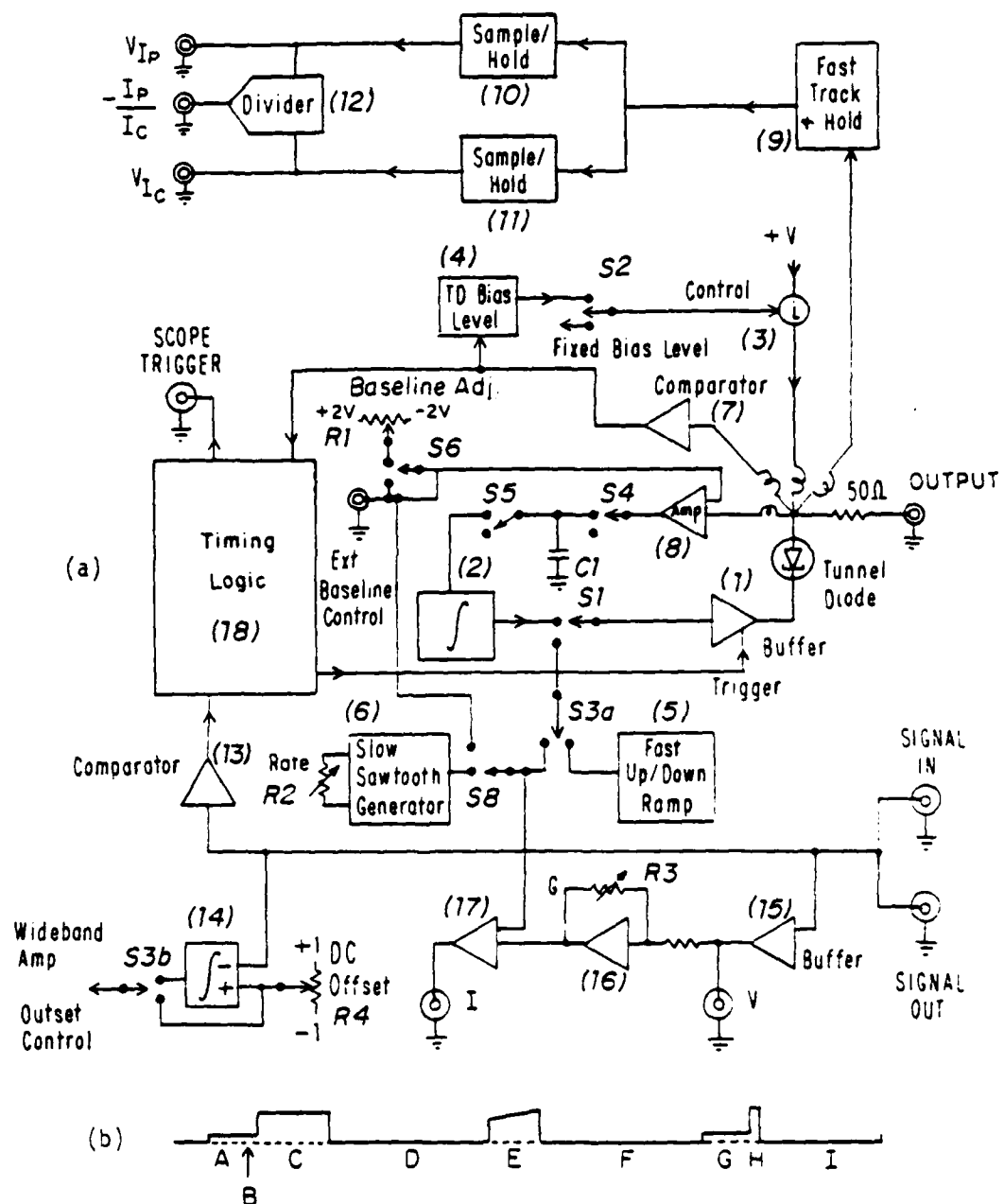


Figure A-1 (a) Block schematic diagram of the tunnel diode pulse generator. (b) Timing diagram showing one full cycle.

All others are manual switches on the front of the box.

A timing diagram of the pulse generator is shown in Figure A-1(b). It can be briefly described as follows: during A the baseline of the pulse is present, at B a pretrigger is sent out to the oscilloscope and C is the pulse during which the waveform observations are made (i.e., C is the pulse with which the experiment is concerned). The source voltage necessary to produce critical current is determined during E, while G and H are the baseline and pulse by which the tunnel diode bias current is recalibrated. The baseline shown during A and G is usually adjusted to zero, but is shown as non-zero in the Figure for clarity. During D, F and I the output is off, and the sample equilibrates to the bath temperature. Both parts of Figure A-1 are referred to extensively in the following explanation of the circuit.

The central element of the pulse generator is the tunnel diode. We have used a GE TD266A which has a peak current of 100mA, a valley current of 14mA and undergoes a total forward voltage transition of $\sim 440\text{mV}$. Its I-V curve is shown in Figure A-2. Since its internal capacitance is only 6pf, it can in principle make its transition in $t \approx C\Delta V/I \approx 22\text{ps}$. In our circuit the output pulse has a rise-time of $\sim 300\text{ps}$. We believe this slowness is due to inductance and stray capacitance. Referring to the timing diagram, the tunnel diode is in its high voltage state during C and H.

The voltage relative to which the tunnel diode operates is set by a very high frequency, low impedance buffer (1). Thus, the effective source voltage, V^S , equals $V_{\text{buffer}} + V_{\text{TD}}(\text{time})$. Hence, $V^S_{\text{baseline}} =$

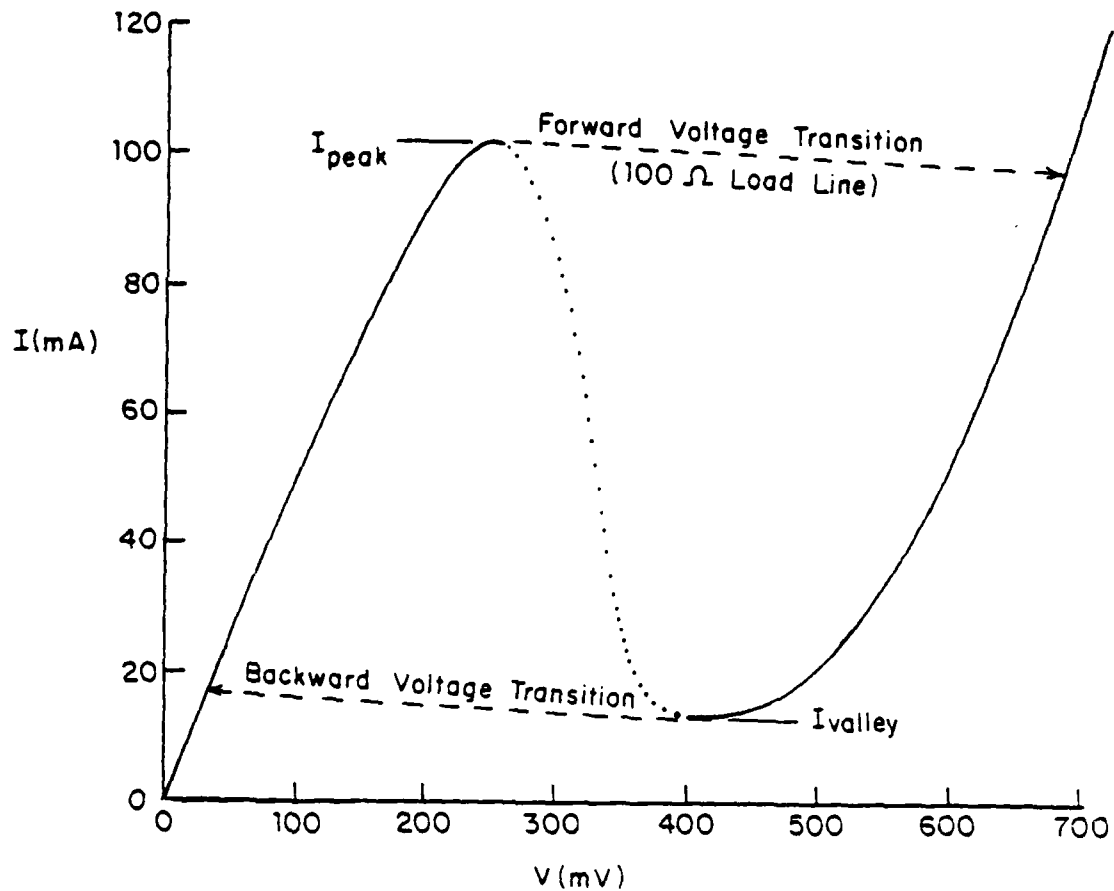


Figure A-2 I-V curve for the TD266A tunnel diode used in our pulse generator. The dashed lines show the transitions made by the diode when biased on a 100 Ω load line.

$V_{\text{buffer}} + V_{\text{TD, peak}} = V_{\text{buffer}} + .25\text{V}$ and $V_{\text{pulse}}^{\text{S}} = V_{\text{buffer}} + .69\text{V}$. This source voltage is applied to the output through a 50Ω resistor so that the pulse generator will properly terminate any signals that are reflected back up the transmission line. As a result, the output voltage equals $.5 \times V_{\text{source}}$ and the step voltage output into 50Ω is $\sim 220\text{mV}$. Since V_{buffer} is variable, the baseline can be adjusted to any desired voltage. R1, which is on the front panel, allows it to be adjusted between $\pm 1\text{V}$.

The source of the buffer voltage is determined by switches S1 and S3. During the pulse times AC and GH, the voltage is taken from the integrator (2) that holds the baseline voltage. During the critical current measurement time, E, it comes from the ramp (5). It is set to zero voltage during the off times, D, F and I. When the front panel switch S3 is set for I-V mode, S1 remains connected to S3 all the time and the voltage that drives the buffer comes from the "slow" sawtooth generator (6) or from the baseline control.

The bias current for the tunnel diode is supplied by a voltage controlled current source (3). This current source is connected through a small inductance, as are all of the other contacts to the tunnel diode, except the output, so that it will present a high impedance to the transient of the tunnel diode. During the times when the tunnel diode is used (AC and GH), S2 is set so that the voltage controlling the current source comes from the tunnel diode bias level (4). While the circuit is idling, during D, F and I, switch S2 is turned off, so that no current flows. It is set to a fixed bias level that results in $\sim 10\text{mA}$ during E, when the critical current is being determined, so that the

buffer (1) does not need to source current (since it is an emitter follower intended to sink the current from (3)). This 10mA level is also applied when the I-V mode is being used.

To work properly, the tunnel diode must be biased with a current that is just slightly below its switching level. Since this level depends on temperature, load and baseline, it is very desirable to make the circuit self-adjusting. To accomplish this, the control voltage that determines the tunnel diode bias current during AC, which is stored on a capacitor in (4), is readjusted each cycle by the following process. During D this voltage is decreased slightly so that the tunnel diode will be biased below its peak when this voltage is applied to the current source (3) during G. (G is about 1 μ s long so that all of the transients associated with initiating the baseline have time to die away.) At the end of G, (4) begins to ramp up the control voltage (and hence the bias current) and continues to do so until the comparator (7) detects that the tunnel diode has switched. It immediately stops ramping and holds a control voltage very slightly below that at which the tunnel diode switched. This new bias current control voltage is then used for the next experimental pulse, AC.

Since the tunnel diode is biased just below threshold, it needs a small push to cause it to switch at the desired time. This is accomplished by weakly coupling the output of an ECL gate (4ns rise-time) into the buffer amplifier (1). Since the sampling plug-in used to observe the signal requires a trigger before the signal arrives, the timing logic (18) provides one at time B, about 200ns (adjustable by a trimpot) before the tunnel diode is triggered.

The desired baseline voltage is set by the front panel potentiometer R1 or by an external control voltage, depending on the setting of switch S6. The feedback circuit [(8),S4,C1,S5,(2)] causes the output baseline to follow the control voltage. The amplifier (8) detects the difference between the actual V_{baseline} and the desired V_{baseline} . During A it places a voltage on C1 (through S4) proportional to this difference. During D the charge on C1 is transferred through S5 into the integrator (2), thus creating a new voltage for the buffer (1) to use during GH, when the bias current is adjusted, and during the next AC. The integrator (2) integrates up or down, a little each cycle, until $V_{\text{baseline,out}} = V_{\text{baseline,in}}$ at which point no more charge is transferred through C1. It then maintains the baseline voltage at that level.

The source voltage necessary to exceed critical current is determined during E. As mentioned above, the current source (3) is set to a small fixed bias current and the input to the buffer (1) comes from (5). Inside of (5) there is a capacitor that holds the voltage that is sent to the buffer. During E this voltage is ramped up until the comparator (13) (which monitors the voltage coming back from the sample) detects that the microbridge has begun to go normal. This signal from the comparator initiates time period F, during which (1) and (3) are in the idle state and the capacitor in (5) is ramped back down for a fixed period of time at the same rate at which it was ramped up, so that it will be ready for the next cycle. Both the ramp rate and duration are adjustable by means of trimpots.

The high speed track and hold (9), an Analog Devices module, is used to acquire the source voltage at which critical current is reached. During E it is set in the "track" mode, and its output follows the source voltage. The instant the threshold is detected, the track and hold is switched to "hold" and its output is held at that value of the source voltage at which critical current was reached. Since the high speed track and hold has a large "droop" rate (i.e., the stored charge that defines the output voltage leaks away fairly quickly) its output is immediately sampled and held by (11), a lower speed, low droop rate sample and hold circuit, the output of which can be monitored externally.

The magnitude of the source voltage pulse is obtained similarly. A few hundred nanoseconds after C begins, the source voltage is again held in (9). This time the output of (9) is sampled and held by (10), a circuit that is identical to (11). Its output can also be externally monitored. The outputs of (10) and (11) are fed into an analog divider (12), which is set up so that its output is exactly $-V_{\text{pulse}}/V_{\text{IC}}$ in volts, which is equal to $-I_{\text{p}}/I_{\text{c}}$ in volts. A six position calibration switch is provided on the front panel to facilitate the adjustment of the various trimpots that ensure the accuracy of the divider. Most of the inaccuracies in the ratio come from errors in determining V_{IC} because of the difficulty of setting the comparator (13) threshold, especially for very low resistance samples.

One other aspect of the circuitry when the pulse mode is in use is that integrator (14) adjusts the DC offset of the wideband amplifier (a B&H Electronics type DC3002-AL). This is done during time period D

(i.e., when no voltage is being generated) and causes the DC output voltage of the amplifier to equal the voltage set on R4, a front panel control. In this way any thermal drift in the output of the amplifier is eliminated. When the I-V mode is used, the integrator (14) cannot be used, and is bypassed by switch S3b.

When S3 is set to the I-V mode, the tunnel diode voltage is nearly zero and the output voltage is determined by the buffer (1). The input voltage of the buffer comes from either the "slow" sawtooth generator (6) or the baseline voltage, depending on the setting of S8, which is on the front panel. When S8 is set to the baseline, the voltage can either be externally controlled or be manually set by R1. When the sawtooth generator (6) is used, its repetition rate can be varied from $\sim 7\text{kHz}$ to $\sim 0.001\text{Hz}$ using R2 and a fast/slow range switch.

Since the sample is located between two terminated 50Ω transmission lines, it sees an effective 25Ω load line. Circuits (15), (16) and (17) are used to correct for this load line: they put out signals proportional to the true I and V of the sample. The output of the wideband amplifier is buffered by (15), which has a very high input impedance. Its output is equal to the sample voltage multiplied by A_{wb} , the gain of the wideband amplifier, and it is put out as "V" on the front panel. The actual current through the sample is given by

$$\begin{aligned} I_{\text{sample}} &= V_{\text{source}} \times D / 50\Omega - V_{\text{sample}} / 25\Omega \\ &= D \times (V_{\text{source}} - (A_{wb} V_{\text{sample}}) \times 2 / (A_{wb} D)) / 50\Omega, \end{aligned}$$

where D is the numeric attenuation (not in decibels). Therefore, to obtain an output signal proportional to the current, the variable gain amplifier (16) amplifies $A_{wb}V_{\text{sample}}$ ("V") by $2/(A_{wb}D)$ and the result is subtracted from V_{source} in (17). Thus, the voltage that is put out of (17) is equal to $I_{\text{sample}} \times 50\Omega/D$. The amplification of (16), A_{16} , is set by $R3$, which is labelled "G" and varies from 0 to 10. This "G" equals $10/A_{16}$ and should therefore be set to $G=5 \times A_{wb}D$ for proper accounting of the load line. Figure A-3 shows a plot of the proper G vs Attenuation for the wide band amplifier used. Note that this Figure is valid only when the output of the amplifier is properly terminated in 50Ω since its unterminated gain is about a factor of two higher than its terminated gain.

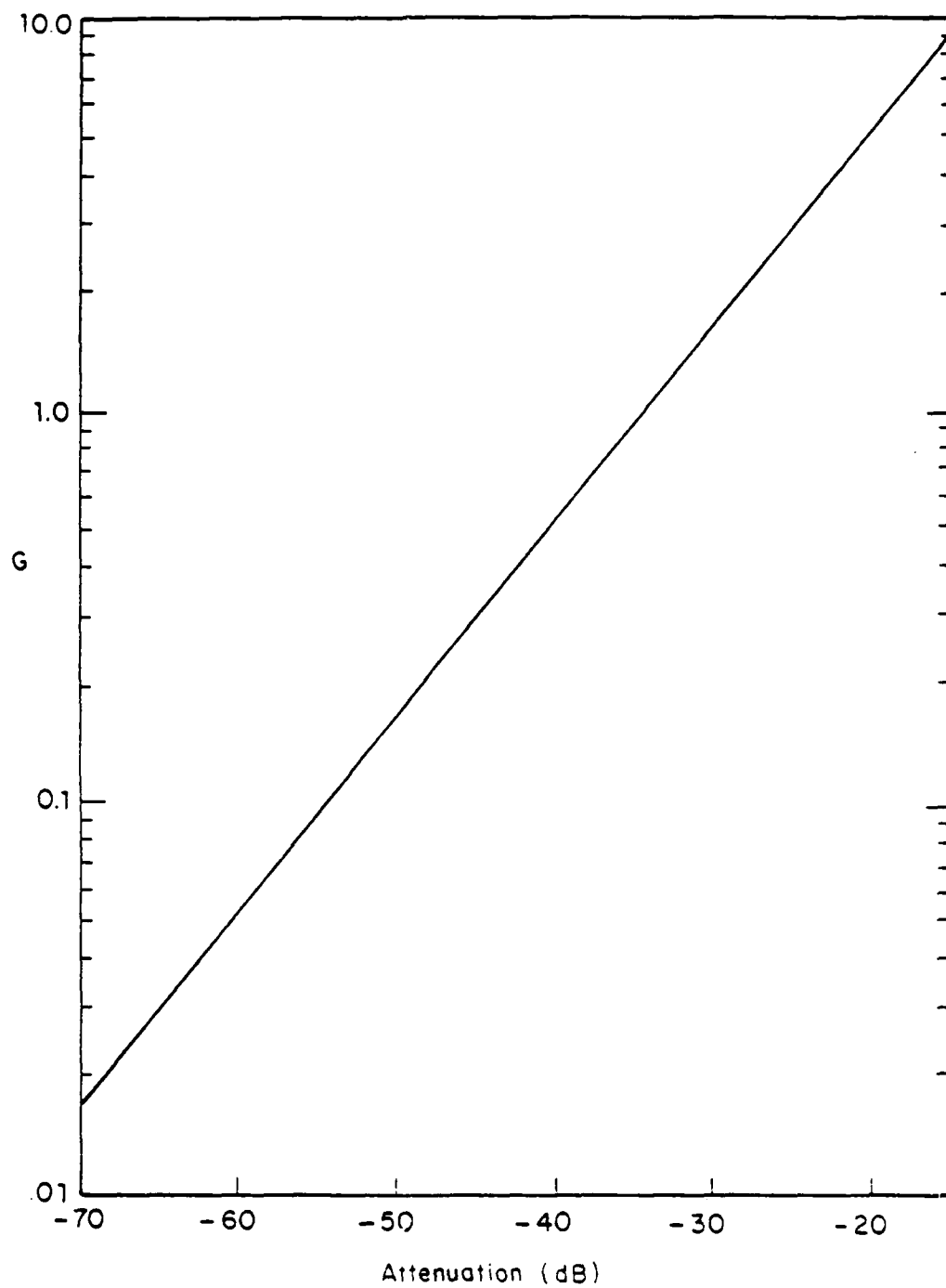


Figure A-3 Calibration diagram for G , the I-V curve correction control, as a function of the attenuation of the current output to the sample.

APPENDIX B

NUMERICAL SOLUTION OF SST EQUATIONS

B.1 The Equations

As discussed in Chapter 4, we have written a computer program that numerically solves the partial differential equations of Schmid, Schön and Tinkham (1980), as applied to our particular experiment. In this Appendix we specify in more detail the equations and approach we have used in the numerical solution, and provide a listing of the actual program.

In our usual approximation of an infinitely long one-dimensional strip that is completely uniform along its length, the SST equations are as given in Eq. (4-22). These equations are only valid for dirty superconductors close to T_c , i.e., $\xi/\xi_0 \ll 5.5$ and $(1-t) \ll 1$. They are repeated here for convenience:

$$N_1 \dot{\delta f} + \frac{N_1}{E} \delta f + R_2 \dot{\psi} \frac{\partial f}{\partial \epsilon} - D' N_2 R_2 q \dot{q} \frac{\partial f}{\partial \epsilon} = 0 \quad (B-1a)$$

$$(1-\psi^2-q^2) \dot{\psi} = \tau_{GL} \dot{q} + \frac{1}{1-t} \int_{-\infty}^{\infty} R_2 \delta f d\epsilon \quad (B-1b)$$

$$\frac{2}{3\sqrt{3}} J = \psi^2 q - \tau_J \dot{q} \int_{-\infty}^{\infty} M \frac{\partial f}{\partial \epsilon} d\epsilon - 4 \frac{\tau_J}{\hbar} q \int_{-\infty}^{\infty} N_2 R_2 \delta f d\epsilon \quad (B-1c)$$

where $\epsilon = E/\Delta_0$ is the reduced energy, $\psi = \Delta/\Delta_0$ is the reduced gap, $q = \xi(T)Q/\hbar$ is a renormalized superfluid momentum, $f = f_{th} + \delta f$ is the quasi-particle distribution function, and $J = I/I_c$ is the reduced critical current. The generalized densities of states, N_1 , N_2 , R_2 and M , and the other quantities will be defined below.

Since the densities of states are very sharply peaked at $\epsilon = 0$, it is necessary to choose a new energy variable which will in effect spread out the peaks and make it easier to discretize the energy. The variable change we have used is

$$\epsilon = \psi (\epsilon^n + 1 + 4\gamma_0 \epsilon) \quad (B-2)$$

where ϵ is the new energy variable and $\gamma_0 = \Gamma_0/\Delta_0$ is the rescaled initial pair breaking potential. The exponent, n , is chosen to be the closest odd integer to $-\ln(\gamma_0)$, as this was found to give well-spread-out peaks. Thus, ϵ varies from 0 to ∞ as ϵ varies from -1 to ∞ , and the slowest variation of ϵ with ϵ occurs at $\epsilon = 0$, when $\epsilon = 0$. In practice, n is usually 3 or 5 and the energy is only taken out to $\epsilon = 100$, in which case $-1 \leq \epsilon \leq 4 \pm 1$.

In making this change of variables, the changes in the differential and in the derivatives are given by

$$d\epsilon = \psi (n\epsilon^{n-1} + 4\gamma_0) d\epsilon \quad (B-3a)$$

$$\left. \frac{\partial f}{\partial \epsilon} \right|_{\tau} = \left. \frac{\partial f}{\partial \epsilon} \right|_{\tau} \left. \frac{\partial \epsilon}{\partial \epsilon} \right|_{\tau} = \left. \frac{\partial f}{\partial \epsilon} \right|_{\tau} \psi (n\epsilon^{n-1} + 4\gamma_0) \quad (B-3b)$$

$$\left. \frac{\partial f}{\partial \tau} \right|_{\epsilon} = \left. \frac{\partial f}{\partial \tau} \right|_{\epsilon} + \left. \frac{\partial f}{\partial \epsilon} \right|_{\tau} \left. \frac{\partial \epsilon}{\partial \tau} \right|_{\epsilon} \dot{\psi} = \left. \frac{\partial f}{\partial \tau} \right|_{\epsilon} + \left. \frac{\partial f}{\partial \epsilon} \right|_{\tau} \dot{\psi} (\epsilon^n + 1 + 4\gamma_0 \epsilon) \quad (B-3c)$$

Plugging these into (B-1), changing the time scale to τ_E , taking into account the load line and solving for the derivatives gives

$$\begin{aligned} \dot{f} = - \dot{f} - \frac{\partial f}{\partial \epsilon} & \left[\frac{\dot{\psi} (R_2 - N_1 (\epsilon^n + 1 + 4\gamma_0 \epsilon)) - D' N_2 R_2 q \dot{q}}{N_1 \psi (n\epsilon^{n-1} + 4\gamma_0)} \right] \\ & - \frac{\partial f_{th}}{\partial \epsilon} \left[\frac{R_2 \dot{\psi} - D' N_2 R_2 q \dot{q}}{N_1 \psi (n\epsilon^{n-1} + 4\gamma_0)} \right] \end{aligned} \quad (B-4a)$$

$$\dot{\psi} = \frac{\tau_E}{\tau_{GL}} \left[\psi(1-\psi^2-q^2) - \frac{2\psi}{1-\epsilon} \int_{-1}^{\infty} d\epsilon (n\epsilon^{n-1} + 4\gamma_0) R_2 \delta f \right] \quad (B-4b)$$

$$\dot{q} = \frac{\tau_E}{\tau_J} \cdot \frac{\frac{2}{3\sqrt{3}} J - \psi^2 q + \frac{8\Delta_0 \tau_J}{h} q \psi \int_{-1}^{\infty} d\epsilon (n\epsilon^{n-1} + 4\gamma_0) N_2 R_2 \delta f}{1-2 \int_{-1}^{\infty} d\epsilon (M-1) \left(\frac{\partial \delta f}{\partial \epsilon} + \frac{\partial f}{\partial \epsilon} \tanh \right) + \frac{R_N}{R_{\text{source}}}} \quad (B-4c)$$

These are the equations as actually used in the program. The material parameters that are entered into the program are T_c , ξ_0 , λ , τ_E and $1-\epsilon$, which are the critical temperature, the BCS coherence length, the mean free path, the electron-phonon collision time and 1 minus the reduced temperature, respectively. The rest of the quantities in the equations are defined as follows:

the generalized densities of states

$$N_1 = \text{Re} \left(\frac{\epsilon/\psi + i\gamma/\psi}{\sqrt{(\epsilon/\psi + i\gamma/\psi)^2 - 1}} \right) \quad (B-5a)$$

$$N_2 = \text{Re} \left(\frac{i}{\sqrt{(\epsilon/\psi + i\gamma/\psi)^2 - 1}} \right) \quad (B-5b)$$

$$R_2 = \text{Im} \left(\frac{i}{\sqrt{(\epsilon/\psi + i\gamma/\psi)^2 - 1}} \right) \quad (B-5c)$$

$$M = N_1^2 + R_2^2 \quad (B-5d)$$

the reduced pair breaking potential

$$\gamma = \gamma_0 + \frac{1}{2} D' q^2 \quad (B-5e)$$

the equilibrium reduced pair breaking potential

$$\gamma_0 = \frac{\hbar}{2\tau_E \Delta_0} \quad (\text{B-5f})$$

the renormalized diffusion constant

$$D' = \frac{D\hbar}{\xi^2(T)\Delta_0} \quad (\text{B-5g})$$

the diffusion constant

$$D = \frac{1.764 \pi}{3\hbar} kT_c \xi_0 \quad (\text{B-5h})$$

the Ginzburg-Landau coherence length (the radical on the right is an approximation to the Gor'kov χ function; it makes this expression accurate to within 0.5% for all values of z/ξ_0)

$$\xi(T) = \frac{.739 \xi_0}{\sqrt{1+.882\xi_0/z} \sqrt{1-t}} \cdot \sqrt{\frac{6+.882\xi_0/z}{6+.752\xi_0/z}} \quad (\text{B-5i})$$

the equilibrium energy gap

$$\Delta_0 = kT \sqrt{\frac{1-t}{.106}} = 3.07 kT \sqrt{1-t} \quad (\text{B-5j})$$

the Ginzburg-Landau relaxation time

$$\tau_{GL} = \frac{\pi\hbar}{8kT(1-t)} \quad (\text{B-5k})$$

the current relaxation time

$$\tau_J = \frac{2\pi\hbar kT}{\pi\Delta_0^2} \quad (\text{B-5l})$$

In solving equations (B-4), $\dot{\gamma}$ and \dot{q} are evaluated first, and then all of the $\dot{f}(z)$ are calculated in terms of these new values of $\dot{\gamma}$ and \dot{q} . After the derivatives are all calculated, a plot is determined based

on stability considerations and on the maximum permitted fractional increment of all of the quantities. Then new values for ψ , q and all the $\delta f(\epsilon)$ are calculated (e.g., $\psi(t+\delta t) = \psi(t) + \delta t \dot{\psi}(t)$). The energy variable, ϵ , is discretized into a number of evenly spaced energy values, where the number can be varied up to 500. We usually used 50 values, as that was found to yield good results without taking an unreasonable amount of computer time. It was found that in order to ensure stability, the energy derivative $\frac{\partial \delta f}{\partial \epsilon}$ must be discretized using both the forward and backward differences, which are $\frac{\delta f(\epsilon + \delta \epsilon) - \delta f(\epsilon)}{\delta \epsilon}$ and $\frac{\delta f(\epsilon) - \delta f(\epsilon - \delta \epsilon)}{\delta \epsilon}$, respectively. The forward difference is used for those terms in the coefficient of $\frac{\partial \delta f}{\partial \epsilon}$ that are positive, and the negative difference is used for those that are negative.

Section 2 is a listing of the computer program, which is written in FORTRAN.

B.2 Program Listing

```

C  DELAY TIME PROGRAM--BASED ON S-S EQUATIONS.  IBM TEMP SCAN VER 11.0
C  G IS THE REDUCED GAP AS A FUNCTION OF TIME
C  Q IS THE RENORMALIZED SUPERFLUID MOMENTUM
C  DF IS THE NONEQ CHANGE IN THE QP DISTRIBUTION FUNCTION
C  DFDT IS THE TIME DERIVATIVE OF DF
C  A(I) AND B(I) ARE THE COEFFICIENTS OF DGDT AND DQDT IN Eq B-4(a)
C  REAL K,IC,ICO,IS,IP,IPO,KT,N1,N2,N2R2,MT,MFP
C  LOGICAL RISING
C  IMPLICIT COMPLEX(C)
C  DIMENSION DF(500),DFDT(500),A(500),B(500),TRA(10)
C  DIMENSION DERDE(500),EP(500)
C  DATA BETA,K,HBAR,PI/.106,.086170837,.0006582183,3.14159365/
C  FUNCTION DEFINITIONS
C  CNR1(X,Y)=CMPLX(X,Y)/CSQRT(CMPLX(X,Y)**2-1.)
C  CNR2(X,Y)=CMPLX(0,1.)/CSQRT(CMPLX(X,Y)**2-1.)
C  E(I)=EL+I*DE
C  INPUT
C  TYPE *, ' TIME DELAY PROGRAM, FIXED PULSE, TEMP SCAN, '
C  1, ' VERSION 10.0 '
C  TYPE *, ' ENTER STEP CURRENT, ICO, RISE TIME(NS) AND LOAD LINE '

```

```

ACCEPT *,IS,ICO,RT,RLN
TYPE *,' ENTER NO. ENERGY BINS, MAX FRAC INCR,'
1 , ' MAX FRAC OF STAB TIME'
ACCEPT *,NE,FI,FST
TYPE *,' FOR OUTPUT, ENTER MAX COUNT, MAX FRAC CHANGE,',
1 ' MAX INCR, AND FIRST UNIT NUMBER'
ACCEPT *,MC,FC,FINC,LU
TYPE *,' ENTER Tc(DEG), XSIO(um), MN FREE PATH(um), TAU E(ns)'
ACCEPT *,TC,XSIO,MFP,TE
TYPE *,'ENTER TEN (1-t)''s'
ACCEPT *,TRA
C  SETUP VARIABLES
  PAUSE 'INSERT DATA DISK'
  LU=LU-1
  RT=RT/TE                      ! NORMALIZE THE RISE-TIME
  DTTI=10./RT
  ICNT=1
  GOTO 2
1  ICNT=ICNT+1
  IF(ICNT.GT.10) STOP
2  TR=TRA(ICNT)                  ! TR IS 1-T/Tc
  IF(TR.EQ.0.) STOP
  LU=LU+1                        ! LU IS THE FILE # DATA WILL BE WRITTEN ON
  OPEN(UNIT=LU,FORM='UNFORMATTED',ACCESS='SEQUENTIAL',TYPE='NEW',
1  DISP='SAVE')
  DO 10 I=1,NE
  DF(I)=0.
  DFDT(I)=0.
  A(I)=0.
10  B(I)=0.
  T=0.
  M=MC
  DQDIO=1.
  NEM1=NE-1
  KT=K*TC*(1.-TR)                ! KT IS kt IN meV
  DOR=SQRT(TR/BETA)               ! DOR IS GAP/KT
  DO=DOR*KT                       ! EQUILIB GAP IN meV
  TJ=2.*HBAR/(PI*DO*DOR)         ! CURRENT RELAXATION TIME
  TGL=PI*HBAR/(8.*KT*TR)         ! G-L RELAXATION TIME
  GMO=HBAR/(2.*TE*DO)            ! EQUILIB REDUCED PAIR BREAKING POT
  GM=GMO*4.
  XL=.882*XSIO/MFP                ! XIT IS G-L COHERENCE LENGTH
  XIT=.739*XSIO*SQRT((6.+XL)/((6.+XL/1.173)*(1.+XL)*TR))
  DHBAR=.1592*TC*MFP*XSIO        ! DIFFUSION CONST TIMES HBAR
  DP=DHBAR/(XIT*XIT*DO)          ! RENORM DIFFUSION CONST
  TYPE 12
12  FORMAT(4X,'1-T',7X,KT GAP/KT GAP GAMMA',
1  7X,TJ TGL D'' XSI(T)')
  TYPE 14, TR,KT,DOR,DO,GMO,TJ,TGL,DP,XIT
14  FORMAT(1X,8F9.5,F10.5/)
  IC=ICO*(TR**1.5)                ! CRITICAL CURRENT AT TR
  RI=IS/IC                        ! RATIO OF Istep/Ic
  IPO=RI*2./SQRT(27.)
  RU=1.+FC

```



```

RL=1./RU
RNL=1./RLN                                ! RNL=RN/RSOURCE, RLN=RSOURCE/RN
U1=TE/TGL
U2=8.*DO*TJ/HBAR
U3=(TE/TJ)
DQEND=U3*IPO/(1.+RNL)                    ! DQDT WHEN STRIP IS NORMAL
DQI=FINC*DQEND
C  SETUP ENERGY FUNC      ENERGY=GAP*(E**N+1+GM*E),  E IS EPSILON
N=1+2*INT(-.5*ALOG(2.*GM0)) ! EXPONENT n
EL=-1.
D=1.
DO 18 I=1,25
D=D/2.
IF(EL**N+1+GM*EL) 16,19,17
16 EL=EL+D
GOTO 18
17 EL=EL-D
18 CONTINUE
19 Z=100.**(.1./N)
EH=Z -Z*Z*GM/(N*100+GM*Z) ! MAX VALUE OF E
DE=(EH-EL)/NEM1           ! DELTA E
DE2=2.*DE
DEH=.5*DE
EL=EL-DE
DO 20 I=1,NE
EP(I)=1.+E(I)**N +GM*E(I) ! EP IS ENERGY/GAP
20 DERDE(I)=N*E(I)**(N-1) + GM ! DERIV OF EP WRT E
DQDT=0.
DGDTL=0.
DGGDT=0.
C  FIND INITIAL VALUE FOR G AND Q
Q=0.
G=1.
TYPE *,N,EL,EH,DE,'IC=',IC,' J/JC=',RI,'dQdtf=',DQEND
TYPE *
TYPE *,      T      V      G      DGGDT      Q',
1'      S1      J2      DT      GAMMA/G'
WRITE(LU) TR,TC,IS,ICO,RI,XSIO,DHBAR,TE,DQEND
C  BEGIN EQUATION SOLUTION.  TIME LOOP
100 S1=0. ! INTEGRAL IN B-4(b)
S2=0. ! INTEGRAL IN NUMERATOR OF B-4(c)
S3=0. ! INTEGRAL IN DENOM OF B-4(c)
AMX=DEH
GMPP=(GM0+.5*DP*Q*Q)/G ! PAIR BREAKING POT / G
DO 200 I=1,NE ! ENERGY LOOP FOR INTEGRALS
EA=EP(I)
N1=ABS(REAL(CNR1(EA,GMPP)))
CD=CNR2(EA,GMPP)
N2=ABS(REAL(CD))
R2=AIMAG(CD)
DEDE=DERDE(I)
DFTH=DFTHDE(G,DEDE,EA,DOR)
N2R2=N2*R2
MT=N1*N1+R2*R2

```

```

      IF(I.EQ.1)GOTO 110          ! SET UP DERIVATIVES WRT E
      IF(I.EQ.NE)GOTO 120
      DDFDEF=(DF(I+1)-DF(I))/DE
      DDFDEB=(DF(I)-DF(I-1))/DE
      GOTO 130
110   DDFDEF=(DF(2)-DF(1))/DE
      DDFDEB=DDFDEF
      GOTO 130
120   DDFDEF=(DF(NE)-DF(NE-1))/DE
      DDFDEB=DDFDEF
130   S1=S1+DE*DEDE*R2*DF(I)      ! SUM UP INTEGRALS
      S2=S2+DE*DEDE*N2R2*DF(I)
      S3=S3+DE*(MT-1.)*(DDFDEF+DFTH)
      DENOM=N1*G*DEDE
      B1=DP*N2R2*Q
      AMX=AMAX1(AMX,(ABS(DGDT)*(R2+N1*EA)+ABS(DQDT*B1))/DENOM)
      IF(DQDT*Q.GE.0.) GOTO 140    ! EVAL A(I) AND B(I)
      B(I)=B1*(DDFDEB+DFTH)/DENOM
      GOTO 150
140   B(I)=B1*(DDFDEF+DFTH)/DENOM
150   IF(DGDT.LE.0.) GOTO 160
      A(I)=(R2*DDFDEB-N1*EA*DDFDEF+R2*DFTH)/DENOM
      GOTO 200
160   A(I)=(R2*DDFDEF-N1*EA*DDFDEB+R2*DFTH)/DENOM
200   CONTINUE                    ! END OF ENERGY LOOP
C   DETERMINE NEW DERIVATIVES
      DQDT=U3*(G*G*Q-IPO*AMIN1(1.,T/RT)-Q*G*U2*S2)/(2.*S3-1.-RNL)
      DGDT=U1*(G*(1.-G*G-Q*Q)-G*2.*S1/TR)
      DFF=0.
      DO 220 I=1,NE              ! FIND DERIVATIVES OF THE DISTR. FNC
      DFDOT=-DF(I) - A(I)*DGDT + B(I)*DQDT
      DFDT(I)=DFDOT
      DFM=AMAX1(.00001,ABS(DF(I)))
220   DFF=AMAX1(DFF,ABS(DFDOT/DFM))
      DTT=.01
      IF(T.LT.RT) DTT=DTTI
      DQQ=DQDT/AMAX1(Q,.001)
      DGG=ABS(DGDT/G)            ! DT IS THE NEW DELTA TIME
260   DT=AMIN1(FST*DE/AMX,FI/AMAX1(DQQ,DGG,DFF,DTT))
C   INCREMENT TIME
      T=T+DT
      G=G+DT*DGDT
      Q=Q+DT*DQDT
      DO 300 I=2,NE
300   DF(I)=DF(I) +DT*DFDT(I)
C   OUTPUT
      IF(DQDT.GE.DQU.OR.DQDT.LE.DQL) GOTO 302
      IF(RISING.AND.DQDT.LT.DQDTL) GOTO 302
      IF(.NOT.RISING.AND.DQDT.GT.DQDTL) GOTO 302
      IF(M.LT.MC) GOTO 303
302   DQDTN=DQDT/DQEND
      S2=-SQRT(27.)*4.*TJ*D0*Q*G*S2/HBAR
      TYPE 301,T,DQDTN,G,DGDT,Q,S1,S2,DT,GMFP
301   FORMAT(X,5F10.5,2G11.3,E10.2,F10.5)

```

```

WRITE(LU) T,DQDTN,G,DGDT,Q,S2,GMPP
M=0
DQU=AMIN1(DQDT+DQI,AMAX1(1.E-5,DQDT)*RU)
DQL=AMAX1(DQDT-DQI,AMAX1(1.E-5,DQDT)*RL)
303 M=M+1
    RISING=.TRUE.
    IF(DQDT.LT.DQDTL) RISING=.FALSE.
    DQDTL=DQDT
C   CHECK FOR END OF TIME
    IF(DQDT.LT.-.01) GOTO 305
    IF(G.GT.2.) GOTO 305
    IF(G.GT..01) GOTO 100      ! IF NOT END, GO TO 100
C   END OF TIME LOOP
305 DQDTN=DQDT/DQEND
    S2=-SQRT(27.)*4.*TJ*DO*Q*G*S2/HBAR
    TYPE 301,T,DQDTN,G,DGDT,Q,S1,S2,DT,GMPP
    WRITE(LU) T,DQDTN,G,DGDT,Q,S2,GMPP
    CLOSE(UNIT=LU)
    GOTO 1                    ! GO DO NEXT TEMPERATURE
END
C
C   THIS FUNCTION CALCULATES THE DERIVATIVE OF FERMI FUNC WRT E
C
    FUNCTION DFTHDE(G,DEDE,EA,DOR)
    E=G*DOR*EA
    IF(E.GT.50.) GOTO 10
    Y=EXP(E)
    DFTHDE=-(G*DOR*DEDE/(Y+1.))*(Y/(Y+1.))
    RETURN
10  DFTHDE=0.
    RETURN
    END

```

REFERENCES

- Aponte, J. and M. Tinkham, 1982, J. Low Temp. Phys., in press.
- Canavello, B. J., M. Hatzakis and J. M. Shaw, 1977, IBM Tech. Disc. Bull. 19, 4048.
- Cherry, W. H. and J. I. Gittleman, 1960, Sol. St. Elec. 1, 287.
- Chi, C. C. and John Clarke, 1979, Phys. Rev. B19, 4495.
- Chi, C. C., M. M. T. Loy and D. C. Cronmeyer, 1981, Phys. Rev. B23, 123.
- Clarke, John, 1972, Phys. Rev. Lett. 28, 1363.
- Dolan, G. J. and L. D. Jackel, 1977, Phys. Rev. Lett. 39, 1628.
- Donnelly, R. J., 1981, in Physics Vade Mecum, H. L. Anderson, ed., (American Institute of Physics), New York.
- Dunkleberger, L. N., 1978, J. Vac. Sci. Technol. 15, 88.
- Faris, S. M. and A. Davidson, 1979, IEEE Trans. Mag. MAG-15, 416.
- Faris, Sadeg M., 1980, Appl. Phys. Lett. 36, 1005.
- Faris, S. M. and N. F. Pedersen, 1981, Physica 108B+C, 1087.
- Geier, Alfons and Gerd Schön, 1982, J. Low Temp. Phys. 46, 151.
- Gittleman, J. I. and S. Bozowski, 1964, Phys. Rev. 135, A297.
- Glang, R. and L. V. Gregor, 1970, in Handbook of Thin Film Technology, Ch. 7, L. I. Maissel and R. Glang, eds., (McGraw-Hill), New York.
- Greiner, J. H., C. J. Kircher, S. P. Klepner, S. K. Lahiri, A. J. Warnecke, S. Basavaiah, E. T. Yen, John M. Baker, P. R. Brosious, H.-C. W. Huang, M. Murakami and I. Ames, 1980, IBM J. Res. Develop. 24, 195.
- Guyon, E., F. Meunier and R. S. Thompson, 1967, Phys. Rev. 156, 452.
- Hagedorn, F. B., 1964, Phys. Rev. Lett. 12, 322.
- Hsiang, Thomas Y. and John Clarke, 1980, Phys. Rev. B21, 945.
- Jillie, D. W., 1976, Ph.D. thesis, SUNY at Stony Brook.
- Jillie, Don, 1980, unpublished.

- Josephson, B. D., 1962, Phys. Lett. 1, 251.
- Kaplan, S. B., C. C. Chi, D. N. Langenberg, J. J. Chang, S. Jafarey and D. J. Scalapino, 1976, Phys. Rev. B14, 4854.
- Lindelof, P. E. and J. Bindslev Hansen, 1977, J. Low Temp. Phys. 29, 369.
- Matisoo, J., 1978, J. de Physique C6, 1590.
- Mooij, J. E., 1981, in Nonequilibrium Superconductivity, Phonons, and Kapitza Boundaries, K. E. Gray, ed., NATO ASI B65, (Plenum Publishing Corp.), New York, 191.
- Octavio, M., S. Frota-Pessoa, I. F. Oppenheim and J. A. Blackburn, 1981, Phys. Lett. 82A, 365.
- Oppenheim, I. F., S. Frota-Pessoa and M. Octavio, 1982, preprint.
- Palmer, D. W. and S. K. Decker, 1973, Rev. Sci. Instrum. 44, 1621.
- Pals, J. A. and J. Wolter, 1979, Phys. Lett. 70A, 150.
- Peters, Robert and Hans Meissner, 1973, Phys. Rev. Lett. 30, 965.
- Schmid, Albert and Gerd Schön, 1975, J. Low Temp. Phys. 20, 207.
- Schmid, Albert, Gerd Schön and Michael Tinkham, 1980, Phys. Rev. B21, 5076.
- Schmid, Albert, 1981, in Nonequilibrium Superconductivity, Phonons, and Kapitza Boundaries, K. E. Gray, ed., NATO ASI B65, (Plenum Publishing Corp.), New York, 423.
- Schmidlin, F. W., Arthur J. Learn, E. C. Crittenden, Jr. and J. N. Cooper, 1960, Sol. St. Elec. 1, 323.
- Skocpol, W. J., M. R. Beasley and M. Tinkham, 1974, J. Low Temp. Phys. 16, 145.
- Skocpol, W. J., 1976, Phys. Rev. B14, 1045.
- Smith, A. D., W. J. Skocpol and M. Tinkham, 1980, Phys. Rev. B21, 3879.
- Tinkham, M., 1979, Festkörperprobleme (Advances in Solid State Physics), Vol. XIX, J. Truesch, ed., Vieweg, Braunschweig, 363.
- Tinkham, M., 1981, in Nonequilibrium Superconductivity, Phonons, and Kapitza Boundaries, K. E. Gray, ed., NATO ASI B65, (Plenum Publishing Corp.), New York, 231.
- Wolter, J., P. M. Th. M. van Attekum, R. E. Horstman and M. C. H. M. Wouters, 1981, Sol. St. Comm. 40, 433.

ACKNOWLEDGEMENTS

I am deeply grateful to the many people who have contributed to this research and who have made my stay in Cambridge enjoyable. I am especially indebted to my advisor Professor Tinkham for suggesting this research project and for providing encouragement and suggestions along the way. I have also greatly appreciated the opportunity to collaborate with Art Davidson and Sadeg Faris at IBM's Watson Research Center. In this connection, I am particularly grateful to Bill Skocpol for arranging the collaboration. (It is too bad he joined the opposition before it came to fruition.)

Turning the lab's evaporator room into a "clean" room was quite an undertaking. It would have been impossible without the assistance of everyone in the lab. In particular, Bill Skocpol and Alice White made very significant contributions. The efforts of Andy Smith and Greg Blonder in assembling the lab's LSI 11/2 computer were invaluable, since most of my innumerable theoretical calculations were run on it. More importantly at the moment, though, I have been able to use its text editor to write my thesis. I am also very indebted to the group's machinist, Louis DeFeo, for building my rigs and for making the very detailed projection attachment for the microscope. But what about that drawer for the microscope.....?

I have very much enjoyed working with all of the people in the lab and count them all as friends. Greg was a great office-mate for several

years. I wish thesis-writing were as easy as he made it look. Chris Lobb has always been very encouraging. It was a pleasure to work with him on percolation and I look forward to continuing the collaboration. I would like to thank Andy Smith for leaving the lab well stocked in electronics parts, David Abraham for wading through Appendix A and making many useful comments, Bill Danchi for letting me test one of his dirty aluminum microbridges, Juan Aponte for knowing everything there is to know about the material parameters of indium, and Alvin Drehman for providing diversions and distractions once every other week.

I want to especially thank my wonderful wife, Joy, for bearing with my thesis writing and for providing an immense amount of help in finishing it up. Finally, I must thank God for giving me the ability to do this work and enabling me to complete it.

DISTRIBUTION LIST FOR ONR ELECTRONIC AND SOLID STATE SCIENCES

Director Advanced Research Projects Agency Attn: Technical Library 1400 Wilson Boulevard Arlington, Virginia 22209	Commandant, Marine Corps Scientific Advisor (Code AX) Washington, D.C. 20380	Air Force Cambridge Research Laboratory L.S. Hanscom Field Technical Library Cambridge, Massachusetts 02138
Office of Naval Research Electronics Program Office (Code 427) 800 North Quincy Street Arlington, Virginia 22217	Naval Ordnance Station Technical Library Indian Head, Maryland 20640	Harry Diamond Laboratories Technical Library Connecticut Avenue at Van Ness, N.W. Washington, D.C. 20438
Office of Naval Research Code 105 800 North Quincy Street Arlington, Virginia 22217	Naval Postgraduate School Monterey, California 93940 Attn: Technical Library (1 copy) Elect. Engin. Depart. (1 copy)	U.S. Army Research Office Box CM, Duke Station Durham, North Carolina 27706
Director Naval Research Laboratory 4555 Overlook Avenue, S.W. Washington, D.C. 20375 Attn: Technical Library (6 cps) Code 5200 (1 copy) 5210 (1 copy) 5270 (1 copy) 6400 (1 copy)	Naval Missile Center Technical Library (Code 5632.2) Point Mugu, California 93010	Director U.S. Army Engineering Research and Development Laboratories Fort Belvoir, Virginia 22060 Attn: Technical Documents Center
Office of the Director of Defense Research and Engineering Office of the Assistant Director Electronics & Physical Sciences The Pentagon, Room 3D1079 Washington, DC 20301	Naval Electronics Laboratory Center San Diego, California Attn: Technical Library (1 copy) Code 2300 (1 copy) 2600 (1 copy) 4800 (1 copy)	Director National Bureau of Standards Attn: Technical Library Washington, D.C. 20214
Defense Documentation Center (12 cps) Cameron Station Alexandria, Virginia 22314	Naval Undersea Center Technical Library San Diego, California 92132	Naval Research Laboratory 4555 Overlook Avenue, S.W. Washington, D.C. 20375 Attn: Code 5300 (1 copy) 7100 (1 copy) 7900 (1 copy)
Commanding Officer Office of Naval Research Branch Office 536 South Clark Street Chicago, Illinois 60605	Naval Weapons Laboratory Technical Library Dahlgren, Virginia 22448	Naval Electronics Laboratory Center San Diego, California 92152 Attn: Code 2100 (1 copy) 2200 (1 copy)
San Francisco Area Office Office of Naval Research 50 Fell Street San Francisco, California 94102	Naval Ship Research and Development Center Central Library (Codes L42 And L43) Washington, D.C. 20007	C.C. Klick Superintendent Materials Sciences Division Naval Research Laboratory 4555 Overlook Avenue, S.W. Washington, D.C. 20375
Commanding Officer Office of Naval Research Branch Office 1030 East Green Street Pasadena, California 91101	Naval Surface Weapons Center White Oak Laboratory Silver Spring, Maryland 20910 Attn: Technical Library (1 copy) Code 200 (1 copy) 212 (1 copy)	Naval Research Laboratory 4555 Overlook Avenue, S.W. Washington, D.C. 20375 Attn: Code 5220 (1 copy) 5230 (1 copy) 5250 (1 copy) 5260 (1 copy) 5270 (1 copy) 5500 (1 copy)
Commanding Officer Office of Naval Research Branch Office 495 Summer Street Boston, Massachusetts 02210	Deputy Chief of Naval Operations (Development) Technical Analysis and Advisory Group (Code NOF-0770) Washington, D.C. 20350	Naval Electronics Laboratory Center San Diego, California 92152 Attn: Code 2500 (1 copy) 4000 (1 copy)
New York Area Office Office of Naval Research 115 Broadway 5th Floor New York, New York 10003	Commander Naval Air Systems Command Washington, D.C. ATTN: Code 310 (1 copy) 360 (1 copy)	Office of Naval Research (2 cps) 800 N. Quincy Street Arlington, Virginia 22217 Attn: Code 430 (2 copies)
ODOR&E Advisory Group on Electron Devices 201 Varick Street New York, New York 10014	Commander Naval Electronics Systems Command Washington, D.C. 20360 Attn: Code 304 (1 copy) 310 (1 copy)	Naval Research Laboratory 4555 Overlook Avenue, S.W. Washington, D.C. 20375 Attn: Code 5400
Naval Air Development Center Attn: Technical Library Johnsville Marinaster, Pennsylvania 18974	Naval Surface Weapons Center Attn: Library Dahlgren, Virginia 22448	Naval Electronics Laboratory Center San Diego, California 92152 Attn: Code 3000 (1 copy) 5000 (1 copy) 5600 (1 copy)
Naval Weapons Center China Lake, California 93555 Attn: Technical Library (1 copy) Code 6010 (1 copy)	Air Force Office of Scientific Research Attn: Electronic and Solid State Sciences Division Department of the Air Force Washington, D.C. 20333	Air Force Office of Scientific Research Mathematical and Information Sciences Directorate 1400 Wilson Blvd. Washington, D.C. 20333
Naval Research Laboratory Underwater Sound Reference Division Technical Library P.O. Box 8337 Orlando, Florida 32806	Air Force Weapon Laboratory Technical Library Kirtland Air Force Base Albuquerque, New Mexico 87117	
Navy Underwater Sound Laboratory Technical Library Fort Trumbull New London, Connecticut 06320	Air Force Avionics Laboratory Air Force Systems Command Technical Library Wright-Patterson Air Force Base Dayton, Ohio 45433	

DATE
FILMED
— 8